UNIVERSITY OF PADOVA

DEPARTMENT OF INFORMATION ENGINEERING

DOCTORAL THESIS

Automated analysis of corneal images for early diagnoses and large-scale screening in ophthalmology

---

Ph.D. School in: **INFORMATION ENGINEERING**
Curriculum: **BIOENGINEERING**
Series: **XXXV**

Supervisor:
Prof. Fabio SCARPA

Ph.D. Candidate:
Alessia COLONNA

School Director:
Prof. Andrea NEVIANI

A thesis submitted in fulfillment of the requirements
for the degree of Philosophiæ Doctor (Ph.D.)

2022

Abstract

This thesis deals with the automate analysis of confocal microscopy images of the corneal sub-basal nerve plexus. New methodologies are proposed for the identification and tracing of the structures present in this corneal layer, with particular attention to nerve fibers. Starting from their tracing, the parameters of clinical interest are estimated. The latter will be useful for making diagnoses, for mass screening, and for obtaining an early diagnosis of some pathological and/or inflammatory states.

Infections and diseases, whether ocular or systemic, affect the structure of the cornea. This means that the corneal structures, in particular the nerve fibers and dendritic cells, change their morphology and their density in relation to the presence of pathological and inflammatory states. The changes in morphological aspect of corneal structure can affect vision in numerous ways: in some cases, it can lead to blindness; in others, patients are subjected to feelings of discomfort and painful sensations. It is important to underline that these parameters may also vary in the presence of other factors: advancing age, prolonged use of contact lenses, surgery (LASIK, PRK, or corneal transplant).

Initially, corneal structures were studied *ex vivo*, with the problem that they degenerate within the first 14 hours after death. Thanks to the introduction of confocal microscopy, these analyzes can be performed *in vivo* (in-vivo confocal microscopy, IVCM), in a rapid and non-invasive way.

Over the years, particular interest has been directed to the analysis of IVCM images of a specific corneal layer: the above mentioned sub-basal nerve plexus. It contains several nerve fibers (the cornea is the most innervated tissue in the human body) and, thanks to the IVCM technique, it is the only nervous part in the human body that is directly accessible *in vivo* and non-invasive.

At present, analyzes of this type of images are performed manually or semi-automatically, taking a long time for the execution and being sometimes subjective and prone to error.

Therefore, the need to develop an automatic tool for the evaluation and analysis of IVCM images of the sub-basal plexus is evident. Automatic methods, suitable for carrying out this type of analysis, usually follow well-defined phases. First, it will be necessary to identify and trace the structures present in the available images. Starting from this, it will be necessary to quantitatively measure the characteristics and morphology of the structures themselves, estimating the parameters of clinical interest. Finally, the parameters must be studied to obtain the relationship between them and the presence of pathological (in the initial or already overt stages), inflammatory and postoperative states.

In this thesis, a new methodology for the identification and tracing of corneal nerve fibers will be described. The method, based on modern deep learning techniques, has allowed the limitations of automatic methods previously presented in the literature but never universally accepted. The proposed method has been shown to minimize the required computing time and provide more accurate results.

In order to obtain the best framework, various aspects related to the use of deep learning techniques for semantic segmentation were investigated. The first aspect aims to improve results by manipulating the ground truth: nerve tracing was based on the segmentation of the whole nerve fiber region (providing the networks with as much information as possible, not just the centerline, as it was done before). The second aspect aims to investigate which is the best Convolutional Neural Network structure for tracing nerve fibers: from a UNet used as baseline, results have been improved adding some specific modules and connections. Instead, the third aspect is linked to the analysis of the adequate loss function: numerous loss functions present in the literature have been analyzed, and two have been proposed. The latter have been developed *ad hoc* for the required task.

From the comparison with the manual analysis, the best combination of the investigated aspect (best Ground Truth, best architecture, and best loss function) achieved a high Global Score (94.79%). This index is derived from two indices often used in the literature to evaluate the goodness of the proposed segmentation: the True Positive Rate (TPR, which is the proportion of nerves correctly identified) and the False Discovery Rate (FDR, which is the proportion of nerves wrongly identified as such), both calculated with a tolerance margin. In the best case, the values are 92.75% for the TPR and 3.07% for the FDR, respectively. These indices underline that the proposed method exceeds the results proposed by other methods based on classical image processing techniques.

Following the proposed algorithm for the identification and tracing of nerve fibers, a method for the automatic estimation of the tortuosity of corneal nerve fibers was investigated. Tortuosity is a highly controversial clinical index: the correlation between tortuosity and a large group of ocular and systemic diseases has already been demonstrated; however, there is no universally accepted definition of tortuosity.

The conducted analysis allows identifying three classes of tortuosity: low, medium, and high. All the fundamental aspects for the analysis of tortuosity are considered. First, a new method is proposed to address the problem of bifurcations (keeping the main nerve fiber together and separating the secondary). Subsequently, three different tortuosity measures are estimated for each nerve fiber under analysis (taking into account three different aspects of tortuosity). Finally, a single tortuosity value is identified for the entire image, considering the optimal length and tortuosity value of each individual fiber. The proposed framework reached an accuracy of 96.6% in terms of correspondence with the manual analysis in the classification of the three classes.

The results obtained are encouraging and may represent a new starting point for

improving the analysis of tortuosity and other clinical parameters related to the analysis of the corneal nerves.

Finally, this thesis has focused on the clinical aspect, taking into consideration two limitations of the methods analyzed so far: the limitation of the visual field of a single image and the presence of structures other than nerve fibers in the images of the sub-basal plexus. In this regard, some methods have been proposed for the analysis of images of patients affected by diabetic neuropathy or Parkinson's disease, or subjects who had undergone LASIK-type surgery. In the case of the presence of pathology, the analysis was performed on multiple images simultaneously, or on mosaics, obtained by reconstructing the corneal surface from numerous IVCM images. Instead, in the postoperative case, attention was paid to the identification of dendritic cells present in the sub-basal plexus and which indicate the presence of an inflammatory state, giving an idea of the progress of the healing process. These analyzes made it possible to highlight the need for the previous steps (precise tracing of corneal nerve fibers and accurate estimation of clinical parameters), as well as the need to simultaneously analyze multiple images and multiple structures.

Sommario

 Questa tesi si occupa dell'analisi automatizzata di immagini del plesso nervoso sub-basale corneale, acquisite tramite microscopia confocale. Vengono proposte nuove metodologie per l'identificazione e il tracciamento delle strutture presenti in questo strato corneale, con particolare attenzione alle fibre nervose. A partire dal loro tracciamento vengono stimati i parametri di interesse clinico. Quest'ultimo passaggio è necessario per il raggiungimento dello scopo finale: effettuare diagnosi, svolgere screening di massa e ottenere una diagnosi precoce di alcuni stati patologici e/o infiammatori.

La cornea può essere colpita da infezioni e malattie, sia oculari che sistemiche. Questo fa si che le strutture corneali, in particolare le fibre nervose e le cellule dendritiche, cambino la loro morfologia e la loro densità in relazione alla presenza di stati patologici e infiammatori. I cambiamenti nell'aspetto morfologico della struttura corneale, possono influenzare la vista in numerosi modi: in alcuni casi, i pazienti possono essere portati alla cecità; in altri, possono manifestare sensazioni di disagio e di dolore. È importante sottolineare che i parametri morfologici possono variare anche in presenza di fattori diversi da quelli infiammatori e/o patologici: è stato dimostrato, infatti, che anche l'età avanzata, l'uso prolungato delle lenti a contatto e la chirurgia (LASIK, PRK o trapianto di cornea) influiscono sulla morfologia delle strutture corneali.

Inizialmente la cornea e le sue strutture sono state studiate *ex vivo*; tali analisi avevano un grosso limite: le cellule, i nervi e le varie strutture degeneravanono entro le prime 14 ore dalla morte. Grazie all'introduzione della microscopia confocale, queste analisi possono essere eseguite *in vivo* (*in-vivo confocal microscopy*, IVCM), in modo rapido e non invasivo.

Nel corso degli anni, particolare interesse è stato rivolto all'analisi delle immagini di uno specifico strato corneale: il plesso nervoso sub-basale. In esso sono presenti numerose fibre nervose (d'altronde, la cornea è il tessuto più innervato del corpo umano) e, grazie alla tecnica IVCM, è l'unica parte del sistema nervoso umano direttamente accessibile *in vivo* e in maniera non invasiva.

Attualmente, le analisi di questa tipologia di immagini vengono eseguite manualmente o in modo semiautomatico, con lo svantaggio di risultare molto onerose in termini di tempo, oltre a risultare talvolta soggettive e incline a errori.

Pertanto, è evidente la necessità di sviluppare uno strumento automatico per la valutazione e l'analisi delle immagini di IVCM del plesso sub-basale. I metodi automatici idonei a svolgere questo tipo di analisi seguono solitamente fasi ben definite. In primo luogo, c'è la necessità di identificare e tracciare le strutture presenti nelle

immagini disponibili. A partire da questo primo passaggio, è necessario misurare quantitativamente le caratteristiche e la morfologia delle strutture stesse, stimando i parametri di interesse clinico. Infine, l'ultimo passaggio prevede che vengano studiati i parametri ottenuti, con lo scopo di individuare le possibili relazioni tra gli stessi e la presenza di stati patologici (nelle fasi iniziali o già conclamate), infiammatorie e postoperatorie.

In questa tesi verrà descritta una nuova metodologia per l'identificazione e il tracciamento delle fibre nervose corneali. Il metodo proposto, basato sulle moderne tecniche di *deep learning*, ha consentito di superare i limiti dei metodi automatici precedentemente presentati in letteratura, ma mai universalmente accettati nella pratica clinica. È stato dimostrato che il metodo proposto riduce al minimo il tempo di calcolo richiesto e fornisce risultati maggiormente accurati.

Al fine di ottenere il miglior *framework*, sono stati studiati numerosi aspetti legati all'uso di tecniche di *deep learning*, specialmente nel campo della segmentazione semantica. Il primo aspetto mira a migliorare i risultati manipolando il *ground truth*: il metodo proposto per il tracciamento dei nervi si basa sulla segmentazione dell'intera regione delle fibre nervose (fornendo alle reti quante più informazioni possibili), non solo sull'analisi della sola linea centrale, come è stato fatto sino ad ora in letteratura. Il secondo aspetto mira a indagare quale sia la migliore struttura di rete neurale convoluzionale (CNN) per il tracciamento delle fibre nervose: dall'architettura UNet, utilizzata come architettura di base, i risultati sono stati migliorati aggiungendo moduli e connessioni specifici. Il terzo aspetto, invece, mira a individuare quale sia la funzione costo adeguata nella fase di addestramento della rete: sono state analizzate numerose funzioni costo presenti in letteratura e ne sono state proposte due. Queste ultime sono state sviluppate *ad hoc* per il compito richiesto.

Dal confronto con l'analisi manuale, la migliore combinazione di tutti gli aspetti indagati (migliore *ground truth*, migliore architettura e migliore funzione costo) ha ottenuto un *Global Score* elevato (94,79%). Questo indice è derivato da due indici spesso utilizzati in letteratura per valutare la bontà della segmentazione proposta: il *True Positive Rate* (TPR, che è la proporzione di nervi correttamente identificati) e il *False Discovery Rate* (FDR, che è la proporzione di nervi erroneamente identificati come tali), entrambi calcolati con un margine di tolleranza. Nel migliore dei casi, i valori sono rispettivamente 92,75% per il TPR e 3,07% per FDR. Questi indici sottolineano che il metodo proposto supera i risultati proposti da altri metodi, basati su tecniche di elaborazione delle immagini classiche.

Sulle basi dell'algoritmo proposto per l'identificazione e il tracciamento delle fibre nervose, è stato studiato un metodo per la stima automatica della tortuosità delle fibre nervose corneali. La tortuosità è un indice clinico molto controverso: è già stata dimostrata la correlazione tra la tortuosità e un ampio gruppo di malattie oculari e sistemiche; tuttavia, non esiste una definizione universalmente accettata di tale indice.

L'analisi condotta consente di identificare tre classi di tortuosità: bassa, media e

alta. Per raggiungere tale classificazione, vengono affrontati tutti gli aspetti fondamentali che caratterizzano l'analisi della tortuosità, in particolare, e degli altri indici, in generale. In primo luogo, viene proposto un nuovo metodo per affrontare il problema delle biforcazioni: mantenere unita la fibra nervosa principale e separare la secondaria, invece di separare tutti i rami che giungono ad una stessa biforcazionie. Successivamente, vengono stimate tre diverse misure di tortuosità per ciascuna fibra nervosa in analisi. Le tre misure analizzate tengono in considerazione tre diverse caratteristiche della tortuosità. Infine, una volta identificati la lunghezza ottimale e il valore corretto di tortuosità di ogni singola fibra, viene identificato un unico valore di tortuosità per l'intera immagine. Il framework proposto ha raggiunto una precisione del 96,6% per quanto riguarda la corrispondenza con l'analisi manuale nella classificazione delle tre classi.

I risultati ottenuti sono incoraggianti e possono rappresentare un nuovo punto di partenza per migliorare l'analisi della tortuosità e di altri parametri clinici relativi all'analisi dei nervi corneali.

Infine, questa tesi ha rivolto lo sguardo all'applicazione clinica, prendendo in considerazione due limiti delle metodiche finora analizzate: il ridotto campo visivo che caratterizza le singole immagini e la presenza di altre strutture (diverse dalle fibre nervose) nelle immagini del plesso sub-basale in analisi. A tal proposito, sono state proposte alcune metodiche per l'analisi di immagini di pazienti affetti da neuropatia diabetica o da morbo di Parkinson. Inoltre, sono state analizzate immagini acquisite in soggetti che hanno subito un intervento chirurgico di tipo LASIK. Nel caso di presenza di patologia, l'analisi è stata eseguita su più immagini contemporaneamente o su mosaici (ottenuti ricostruendo la superficie corneale da numerose immagini IVCM). Sono questi i casi in cui si è voluto superare il limite del ridotto campo visivo. Nel caso post-operatorio, invece, si è posta attenzione all'identificazione delle cellule dendritiche presenti nel plesso sub-basale (affrontando così il secondo problema legato alla presenza di strutture diverse dalle fibre nervose). Le cellule dendritiche sono interessanti da analizzare in quanto evidenziano la presenza di uno stato infiammatorio e forniscono un'idea dell'andamento del processo di guarigione.

Queste analisi hanno permesso di evidenziare la necessità e l'importanza dei passaggi precedenti (tracciamento preciso delle fibre nervose corneali e stima accurata dei parametri clinici), nonché la necessità di analizzare contemporaneamente più immagini e più strutture.

Contents

List of Figures

List of Tables

Chapter 1

Introduction

1.1   Aim and objectives

For humans, the eye is a window to the outside world. It allows us to see what surrounds us: it receives the light coming from the environment, filters it, focuses it, converts it into an electrical signal, and sends it to the brain. Taking the reverse path, and then observing the structures present in them, allows us to open a window on our health. Through modern and accurate imaging techniques, it is possible to observe the ocular layers and the structures present in them. Therefore, ophthalmic imaging allows diagnosis and monitor post-operative and pathological states (at both the ocular and systemic levels).

Most studies in the literature have focused on the analysis of the retina, a layer responsible for transforming the light beam into an electrical signal. Nevertheless, there are numerous structures in the eye that arouse great interest, as they appear to have a relationship with the begin, advancement, or persistence of some pathological or inflammatory states. However, studies of these structures are very limited compared to those related to the retina.

In this work, we wanted to analyze one of these structures: the cornea. The cornea is the most innervated tissue in the human body; it contains several nerve endings that make this tissue even 300-600 times more sensitive than the skin [1]. Thanks to the confocal microscopy technique, it is possible to visualize *in vivo* the intricate network of nerve fibers of the sub-basal plexus. In-vivo confocal microscopy (IVCM) technique is fast, non-invasive, and allows acquiring images of the corneal layers with good resolution and 800-fold magnification [2].

Therefore, the acquisition of images through IVCM allows for direct visualization of the changes at the cellular level in the different corneal layers, in particular, it is possible to monitor the changes in the morphological parameters of the corneal nerves. Therefore, starting from the observation of nerve fibers and the study of its morphological characteristics, it is possible to investigate the correlations between, on the one hand, patient feedback and clinical outcomes and, on the other hand, the innervation of the sub-basal corneal layer.

Initially, people used to think that these correlations concerned only infections and/or pathologies at the corneal level [3–5]. Subsequently, thanks to more in-depth and extensive studies, it was shown that they are also related to infections and/or

pathologies at the systemic level [6–8]. Some interesting results reported in the literature underline how some morphological changes are already present in the early stages of the disease and can therefore become a useful tool for early diagnosis, thus influencing, in some cases, the subsequent therapy.

Furthermore, other studies have shown that a technique of this type (rapid and non-invasive) is the ideal tool for performing continuous inspections, which are a useful means of quantifying and monitoring the progressive changes in immune responses related to surgery or therapy to which the patient is exposed [2, 9–11].

Despite the non-invasiveness and rapidity of acquisition of the technique, as well as the clinical relevance of the results obtained, the analysis of images of the sub-basal corneal plexus is not common in clinical practice. The big limitation lies in the required analysis, currently performed manually or, in some cases, semi-automatically. To extract the features useful for diagnosis and prognosis (such as nerve fiber length, density, branch points, tortuosity, etc.), it is necessary first to identify and trace the nerve fibers present in the available images. Manual tracing is a very laborious and time-consuming activity. Furthermore, manual analysis is subjective and therefore not reproducible: it varies according to the clinician who performs it and depends on his experience.

Moreover, it should also be noted that a single confocal microscopy image covers only 0.15% of the corneal extension [2, 12]. In this regard, it is evident that, in order to make a diagnosis or extract indicators of the patient's health status, it is necessary to analyze more than a single image. Therefore, the complexity, the time requirement, the subjectivity and the requirement to analyze multiple images for each patient greatly limit the use of IVCM in daily clinical practice.

An automatic instrument, capable of reliably extracting the intricate network of nerve fibers and quantitatively measuring its characteristics and morphology (for example, by estimating its density or tortuosity), would provide a much simpler, more objective, and clinically usable procedure for the image analysis of the corneal sub-basal plexus. Therefore, the purpose of this thesis is to develop a framework for the automatic analysis of confocal images of the sub-basal corneal plexus, investigating three fundamental aspects: the identification and tracing of nerve fibers, the extraction of the features useful for diagnosis (with particular attention to the study of tortuosity), and the clinical application of the previous steps.

As mentioned before, automatic tracing is an important step for quantitative analysis in daily clinical practice. Various methods have been proposed in the literature: all of them attempt to automate the analysis and in particular the tracing of corneal nerve fibers, each presenting strengths and weaknesses, but none universally accepted in clinical practice. The logic of the proposed method is to overcome the limitations of the previous methods, minimizing required computing time, and providing more accurate results. For this purpose, the proposed method is based on the most modern deep learning techniques.

Tracing is the step that precedes the extraction of useful for diagnosis. Among all, tortuosity is the most discussed feature in the literature. The correlation between

corneal nerve tortuosity and pathologies has been demonstrated multiple times. However, since there is no de facto definition of tortuosity, the reproducibility of the proposed results is very poor. Indeed, many studies still rely on manual observation and a qualitative judgment of tortuosity. Some studies have proposed automating the calculation of this feature, but the results obtained are not universally valid. Each proposed metric, in fact, examines different characteristics of the tortuosity and is based on different aspects (geometric distances, angles, curvatures, twist estimation,...). The proposed method aims to simultaneously consider multiple aspects, addressing the classical problems in the estimation of tortuosity, facing the bifurcation problem and the need to switch from an index relative to the single nerve fiber to one related to the whole image.

Finally, different frameworks have been proposed in this work, based on tracing and estimation of the parameters just seen, useful for performing an automated analysis of corneal images for early diagnoses and large-scale screening in different pathologies.

1.2 Outline of the thesis

Chapter 2 "The human eye" is an introductory chapter aimed at presenting the anatomy of the human eye, with particular attention to the cornea, its histology and the structures present in the sub-basal plexus. In the same chapter, the instrument (confocal microscope) is presented which has allowed a great breakthrough in corneal analysis, guaranteeing the acquisition of images in a rapid and non-invasive manner. This technique allows the passage from an *ex vivo* to one *in vivo* analysis, allowing more in-depth and continuous studies. The main recognizable diseases are presented, through the analysis of the sub-basal plexus, diseases are presented, and finally, a quick presentation of the main steps of automated analysis of this type of images is introduced.

In chapter 3 "Nerve Tracing", the analysis for the identification and tracing of the nerve fibers of the sub-basal plexus is proposed. The methods developed and the analyses carried out are discussed, as well as a comparison of the results obtained.

In Chapter 4 "Tortuosity estimation", based on the nerve tracing discussed in chapter 3, the methods proposed for the analysis and estimation of tortuosity are reported. The main problems known in the literature related to this task are analyzed. A completely automatic framework to deal with those problems is proposed. This framework promotes an automatic tool for the classification of images in three levels of tortuosity: low, mid, and high.

Finally, chapter 5 "Single, mosaic, and Multiple-image analysis in clinical application" analyzes the ability of the fully automatic software proposed to extract parameters that are useful for a diagnosis. To do this, the importance of considering an extended region of the cornea will be highlighted. Different approaches will be discussed, such as analyzing multiple images simultaneously or using the mosaic

technique. Furthermore, the need to identify other structures present in the images of the corneal sub-basal plexus will be introduced in the same chapter. Particular attention is paid to dendritic cells: these are especially important cells in the inflammatory process. The introduction of these patterns in the tracing and identification phase of nerve fibers plays a fundamental role: it reduces the errors in the tracing of nerves and allows obtaining more clinical information from the images.

A brief discussion, to summarize the results obtained in each step of the automatic analysis of confocal microscopy images of the corneal sub-basal plexus, is reported in Chapter 6.

Chapter 2

The human eye

The human eye is the main sense organ of the visual apparatus. It has the task of obtaining information on the surrounding environment through light. It refracts light present in the environment, adjusts its intensity through a diaphragm called the iris, and focuses it through an adjustable lens system. This process permits the formation of an image (electromagnetic energy of the visible spectrum). Subsequently, the image is transformed by the retinal receptors into a series of electrical impulses (visual action potentials) that, through the optic nerve, are sent to the cerebral cortex. Lastly, the impulses are processed and interpreted by the cortex, thus producing the sensation of vision [13–15].

In humans, the eye has a hard and elastic consistency and is kept in the correct position, by specialized muscles, bands, nerves and vessels that penetrate it [13, 14].
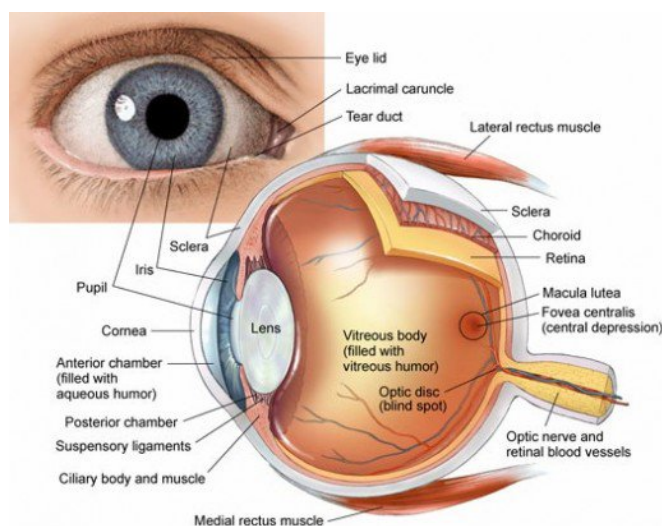
FIGURE 2.1: Basic anatomical diagram of the main anatomical structures of the visual apparatus and the corresponding representation of the right eye seen from the front (top left).

The main structures of the eye present in Figure 2.1 will be briefly described below, following the path of light through them.

Light penetrates the eye through the tear film that covers the outermost structure of the eye: the cornea, showed in 2.2A. This structure provides ideal transmission of light, thanks to the transparency that characterizes it. (The cornea will be investigated

further in this chapter). Together with the sclera, the cornea forms the outermost membrane of the eyeball [16–18].
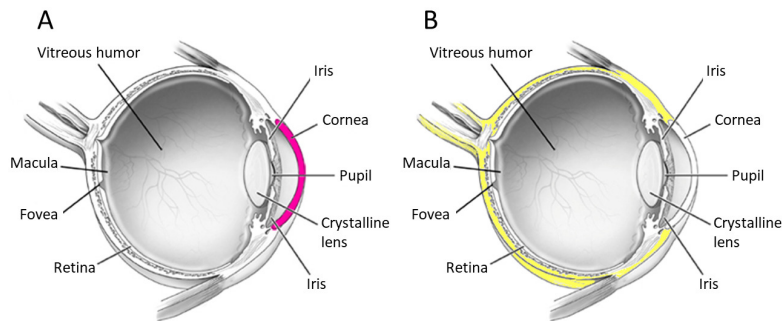
FIGURE 2.2: Schematic representation of the cornea (A - left in magenta) and the sclera (B - right in yellow).

The sclera is a hard, opaque, and white fibrous structure. Its location is shown in Figure 2.2B. It surrounds the entire ocular globe and has a structural and protective function. It resists internal and external forces, maintains the shape of the eyeball, which is fundamental to protect the structures contained in it. Furthermore, this structure is important for the attachment of extrinsic muscles that control the movement of the eyes [13, 14, 16, 19].

After passing through the cornea, light meets a fluid, the aqueous humor. It is a transparent liquid that supplies the cornea and lens with nutrients and keeps the internal pressure of the eye constant. The aqueous humor is produced by the ciliary body [20].
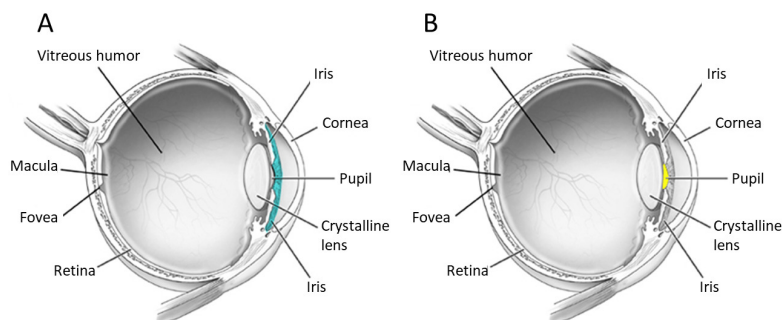
FIGURE 2.3: Schematic representation of the iris (A, left in cyan) and pupil (B - right in yellow).

Behind the aqueous humor, the incoming light meets the iris, represented in Figure 2.3A. It is a colored disc, visible through the cornea, formed by opaque material that has a black hole in the center, the pupil (Figure 2.3B). The iris behaves like the shutter of a camera in which the pupil acts as an aperture. When the amount of light entering the eye decreases, the muscle in the iris promotes pupil dilation, allowing a

greater amount of light to enter and reach the retina. On the contrary, when too much light enters the eye, another muscle of the iris causes the pupil to narrow, allowing less light to reach the retina [13, 14, 19].

The iris, together with the choroid and the ciliary body, forms the uveal tract (or simply the uvea).

The choroid is a membrane that extends below the sclera; it is very rich in blood vessels that serve to nourish the innermost ocular membrane, the retina.

The ciliary body is made up of two parts: the ciliary muscle, strong and smooth muscles connected to the lens, allowing adjustment of the refractive power; and the ciliary epithelium, responsible for the production of aqueous humor[13, 14, 19, 20].

Once the pupil modulates the intensity of the incoming light, the light beam meets the surface of the crystalline lens (Figure 2.4A). The crystalline lens has the shape of a biconvex lens, with a greater curvature in the posterior face. The curvature of the lens faces changes according to the distance of the observed object: this phenomenon is called 'the accommodation process" and allows changes in the optical power of the eye, to allow proper focus on objects at different distances[13, 14, 19].
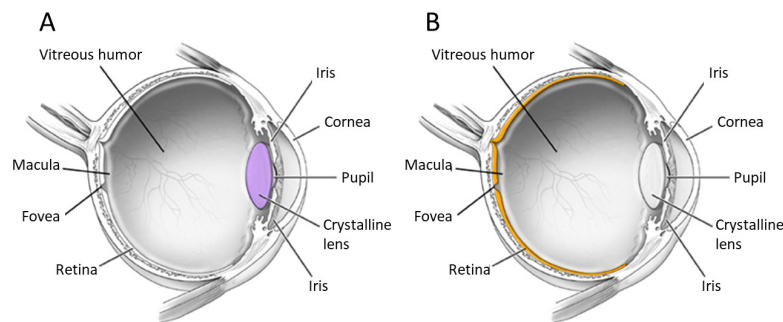
FIGURE 2.4: Schematic representation of the crystalline lens (A - left in purple) and the retina (B - right in orange).

After being focused through the lens, light flows into the eye through vitreous humor: a liquid containing a lipoprotein matrix that gives it gelatinous properties. The liquid fills the space between the lens and the retina, thus helping the sclera maintain the right shape of the eye [16]. The presence of phagocytes allows the elimination of debris and the ability to maintain transparency, which is fundamental for light transmission [13, 14].

Finally, the light beam reaches the retina, the third and innermost coat of the eye, shown in Figure 2.4B. The retina is a multilayered structure composed of different types of neurons, interconnected with each other through synapses.

In the outermost layer of the retina, there are photoreceptors, which are cells sensitive to light radiation that convert photons into neural signals through the phototransduction process. Among the cells that make up it, there are cones and rods: cones operate in conditions of rather intense light and are responsible for color vision; while rods, which are more numerous, are sensitive to low light intensities but do not perceive

colors, thus giving a 'light-dark' type of vision. The central area of the retina is called the macula, and within it there is the fovea, that is the area where the cones are most concentrated (both structures, macula and fovea, are labelled in the figures) [13, 21].

2.1   The Cornea

The cornea, together with the sclera, forms the outer layer of the eyeball whose main purpose is to protect the internal structures of the eye, acting as a structural barrier against infections [13, 14].

Furthermore, the cornea is the first structure that interacts with the beam of light that enters the eye. It has two main functions: to refract and transmit the light beam. The cornea, together with the air-tear interface, contributes approximately two-thirds of the refractive power of the human eye [22, 23], the remaining third is given by the lens.

The transmission of the light beam occurs because of the minimum dispersion and the characteristic transparency of the corneal structure. The cornea, in fact, is made up of cellular and acellular components, but is devoid of vascularization. The lens and cornea are the only tissues in the human body that are not vascularized [24].

Cell and acellular composition, the percentage of water it is made up of (it must remain 78%), and the lack of blood vessels bring the characteristic transparency of corneal tissue [18], ensuring maximum light transmission.

The avascular cornea is nourished by diffusion. It is nourished externally by tears and internally by aqueous humor; the external environment provides adequate oxygenation.

The size of the cornea varies between individuals: the horizontal diameter is slightly larger than the vertical diameter (11.71 ± 0.42 mm and 10.63 ± 0.63 mm, respectively) [25]. The thickness can also vary between individuals, moreover, in the same individual there is a variation between the central, thinner area, to the peripheral, thicker one [26, 27].

2.1.1   Corneal histology

The cornea is made up of three anatomical layers, separated from each other by two membranes. From the outside to the inside there are: the epithelium, Bowman's membrane, the stroma, Descemet's membrane and the epithelium [18, 22, 26]. All layers are schematized in Figure 2.5 and are described below.

- The *epithelium* is the outermost layer of the cornea and creates the first barrier from the external environment. It is composed of 5 to 6 cell layers, whose micro surface irregularities are smoothing from the tear film. This provides a smooth surface and allows cleaning the surface.

    Superficial cells appear polygonal in shape, with a well-defined nucleus, well-defined edges, and have homogeneous density; while the innermost ones have

a smaller polygonal shape, a nucleus not always visible, and a much higher density.

The tight junctions between epithelial cells prevent tears (thus, microbes and fluid) from entering the intercellular spaces.

Epithelial cells are continuously regenerated: corneal epithelial cells have an average lifespan of 7 to 10 days [22, 28]. The outermost cells are subject to apoptosis (cellular and programmed death), and the innermost cells, migrating outward, taking their place.

There are numerous nerve endings in the epithelium, which are responsible for corneal sensitivity and provide fundamental factors for corneal regeneration and healing.

- The *Bowman's membrane* is an acellular layer, composed of collagen fibrils, without any architectural pattern. The border with the epithelial layer is well defined, while the border with the stroma is unclear because the transition is gradual. This membrane protects the underlying stroma layer and, if injured, does not regenerate. In any case, it would not appear to be a membrane that plays a critical role in the structure or function of the cornea [29].

- The *stroma* is the thickest layer of the cornea: it accounts for about 90% of the entire corneal volume.

  It consists of a cellular, an acellular, and a sensorineural part. The cellular part is mainly composed of keratocytes (occupying approximately 3% of the stromal volume). Their density varies according to the region analyzed: they decrease from the anterior to the posterior area.

  The main activity of these cells is the synthesis of the extracellular matrix and stromal remodeling. The acellular part, produced by keratocytes, is composed of collagen fibers, which are grouped to form lamellae. The latter are arranged parallel to the ocular surface, guaranteeing the transparency and strength of the cornea, and reducing the scattering of the light beam [22, 26].

- The *Descemet's membrane* is the other cell-free layer of the cornea. It is made up of collagen secreted by endothelium cells: secretion begins in the uterus, starting at the 8-week stage, and continues throughout life. The membrane acts as a basement membrane for the endothelium [22, 26].

- The *endothelium* is the innermost layer of the cornea and is made up of a single cell layer. At birth, endothelial cells are homogeneous in size and have a uniform hexagonal shape. Since they have limited mitotic activity, cell density decreases at an average rate of 0.6% per year in normal corneas every year. The space previously occupied by cells that die or lose functionality is then occupied by cells that are still alive, which expand and change their shape (polymegathism and polymorphism, respectively) [22, 26, 30].

Structure of the Cornea
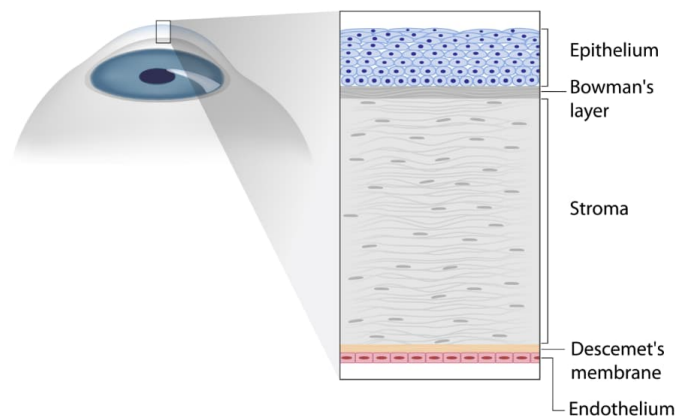
FIGURE 2.5: Schematic representation of the corneal layer.

2.1.2 Corneal nerves

The cornea is the most densely innervated surface tissue in the human body. Indeed, the corneal nerve density is 300 to 400 times greater than the nerve density of human skin. High innervation is essential to ensure protection of the eye from mechanical, thermal, or chemical injury, playing a fundamental role in the blink reflex. In addition to sensory functions, corneal innervation helps maintain the functional integrity of the ocular surface by releasing substances that promote epithelial homeostasis and stimulate tears production [2, 31, 32].

Nerves reach the cornea radially and penetrate it at the mid-stromal level (Figure 2.6). In the stroma, the nerves form a first network: they run parallel to the corneal surface and subdivide several times, creating a network of numerous branches. To maintain corneal transparency, nerve fibers lose their myelin sheaths within about 1 mm of the limbus, continuing into the stroma protected only by the Schwann cell sheaths [31–33].

At some point, the nerve fibers of the stroma abruptly change direction, proceeding in the direction of the corneal surface. These nerves penetrate the Bowman's membrane and continue their course parallel to the corneal surface. In this area, just below the basal cells of the epithelium, a new network is formed. This corneal region is called the **sub-basal nerve plexus**.

In this second network, Schwann cell sheaths are also lost: the lack of a sheath guarantees greater transparency. Furthermore, this absence involves a higher metabolic cost for nerve transmission and makes nerve fibers highly vulnerable to degeneration even due to minimal disturbances, which could be metabolic, toxic, immune, or inflammatory. Due to this ease of degeneration, the body has compensated for the evolution of mechanisms and processes for the regeneration of the corneal nerves [34, 35].
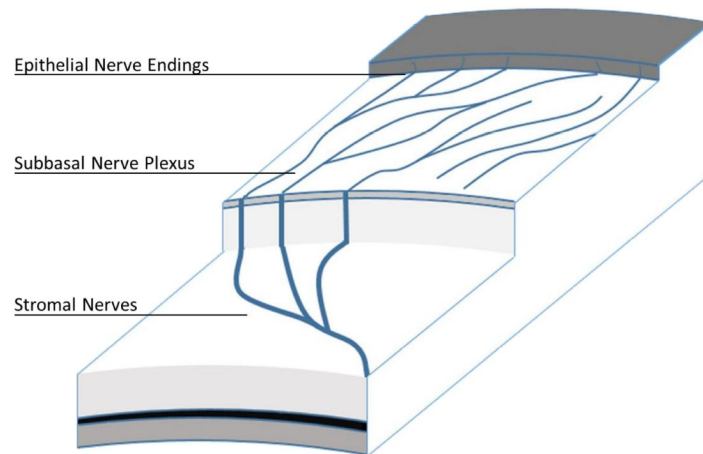
FIGURE 2.6: Schematic representation of corneal nerves propagation through the corneal layers.

If viewed in its entirety, the sub-basal plexus would appear as a spiral-shaped assembly of long nerve fibers. Nerves have been shown to be dynamic: they migrate centripetally, converging on the spiral in the lower nasal quadrant of the paracentral cornea. The imaginary center, or vortex, is located in the lower area, slightly displaced towards the nasal area. In the region of the corneal apex, the fibers are arranged in an almost vertical direction [31, 36, 37].

2.1.3 Dendritics cells

Until about 20 years ago, the cornea was considered a tissue with immune privilege, due to the absence of antigen-presenting cells (APCs) [38].

However, recent studies have shown the presence of APCs in the cornea: in particular, a significant number of macrophages in the posterior stoma and inactive dendritic cells (DCs) in the anterior stroma and in the corneal epithelium (especially between the basal layer and sub-basal) have been detected [39, 40].

Hence, the immune privilege of the cornea has no longer been associated with the lack of resident cells, but with the universally immature phenotype of the cells that reside there [41]. Furthermore, dendritic cells of the corneal epithelium, that reside in the basal layer, have been found to be more numerous in the periphery than in the central region [42].

Due to the functional plasticity of DC in the immature stage, cells play a fundamental role in maintaining corneal homeostasis, immune tolerance, regulating the immune responses of T-cells, and in innate immunity against microbes [38, 40, 41, 43, 44].

Typical dendritic cell morphology is characterized by long extended dendritic processes between adjacent epithelial cells. Due to these extensions, DCs are able to capture harmless and pathogenic antigens and preserve tissues from microbial invasion or the emergence of pro-inflammatory stimuli. When the cornea becomes

inflamed, the corneal DCs mature, migrate to the draining lymph nodes, and present the antigens directly to the T-lymphocytes [45].

Therefore, both nerve fibers and dendritic cells operate as sentinels on the corneal surface. While the former use nociceptors to detect chemical and temperature changes, the latter use protein receptors, called Toll-like receptors.

Nerve fibers and dendritic cells are often found in close proximity, and, for this reason, numerous studies have questioned the interaction between the two [46, 47]. Examples of this are the interaction in the case of inflammatory processes of the airways and in the case of the presence of diabetes. DCs have been observed to mediate innervation and regeneration of sensory nerves through ciliary neurotrophic factor and, as diabetes reduces the population of DCs in corneas, reduced innervation and regeneration of sensory nerve fibers occurs [48].

2.2   Confocal Microscopy

Over the years, for physicians and researchers in the field of ophthalmology, microscopic evaluation of structures, ocular in general, and the cornea in particular, has always represented a great challenge. The characteristic transparency of the cornea allowed its analysis by instruments such as the slit lamp biomicroscope and the ophthalmoscope. However, these instruments presented a few obstacles: first, the inability to produce images with a high magnification. Therefore, the only way to perform detailed analyzes at the microscopic level was by conducting in vitro studies. However, this is a limiting technique: In vitro studies, in fact, tend to introduce artifacts and do not allow the evolution of some processes to be kept under control [34].

To overcome this and other limitations, confocal microscopy was developed. It is a tool that allows the *in vivo* visualization of the cellular architecture and nerve fibers of the cornea. Its main advantage is that it allows the acquisition of numerous images in a very short time and with magnification levels that reach 800 times.

The optical principle behind this technique consists of aligning the light rays emitted, with those reflected by the tissues through a system of lenses. Therefore, the focal point of the lighting system and the observation correspond to each other. This is the reason why the technique is called 'confocal'.

Conventional light microscopy produces low quality images because of the reflected and scattered light from structures that do not belong to the focal plane, whereas confocal microscopy has the ability to not be influenced by the light reflected from structures that do not belong to the focal plane. Therefore, well-defined images are obtained, with a spatial resolution of about 5 microns axially and 1-2 microns laterally. However, the field of vision of acquisition is limited [49].

Figure 2.7 shows a diagram of the operation of the confocal microscope. Briefly, the generated light beam passes through the first pinhole and is focused through a lens system. Subsequently, the light beam reflected from the tissues (in the focal plane and out of the focal plane) is deflected by the objective lens towards a second

pinhole. In this way, light from the out-of-focus planes is prevented from reaching the acquisition system (green arrows in the scheme).
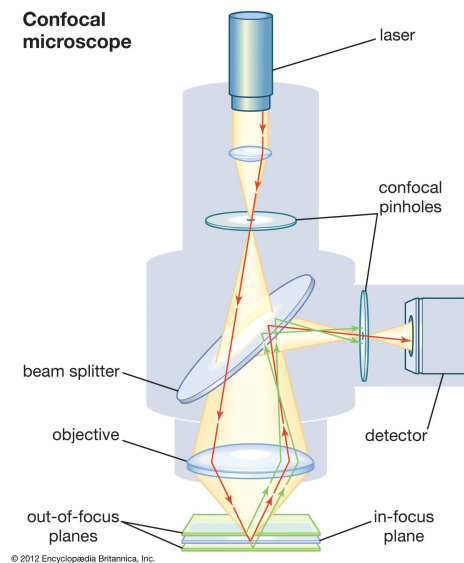
FIGURE 2.7: Representation of the operating scheme of a confocal microscope.

When considering the mechanism by which scanning occurs, it is possible to distinguish three different types of confocal microscope [2]:

- *Tandem-Scanning Confocal Microscope (TSCM)* [50–52]

  It is a microscope that uses a rotating disk on which a set of microscopic pinholes, arranged in an Archimedean spiral, are shown. The large number of openings ensures that there is strong light dispersion, which requires a very powerful light source.

- *Slit-Scanning Confocal Microscope (SSCM)* [51, 52]

  In this microscope, multiple vertical openings (similar to slits) are used for illumination and observation. Such a structure allows scanning a larger area simultaneously and in parallel. Furthermore, the light source needed in this case is less than in the previous one. Instead, the axial and transverse resolutions are reduced as well as the depth steps are increased.

- *Laser-Scanning Confocal Microscope (LSCM)* [51–53]

  As the name suggests, this instrument uses a laser beam, which is moved by a system of mirrors, acquiring the sample in a complete manner. This technique allows obtaining images with better contrast, resolution, quality, and focus than previous techniques.

  This group includes the Heidelberg Retinal Tomograph with the Rostock Cornea Module produced by Heidelberg Engineering, Germany (HRTII-III / RCM), shown in Figure 2.8.
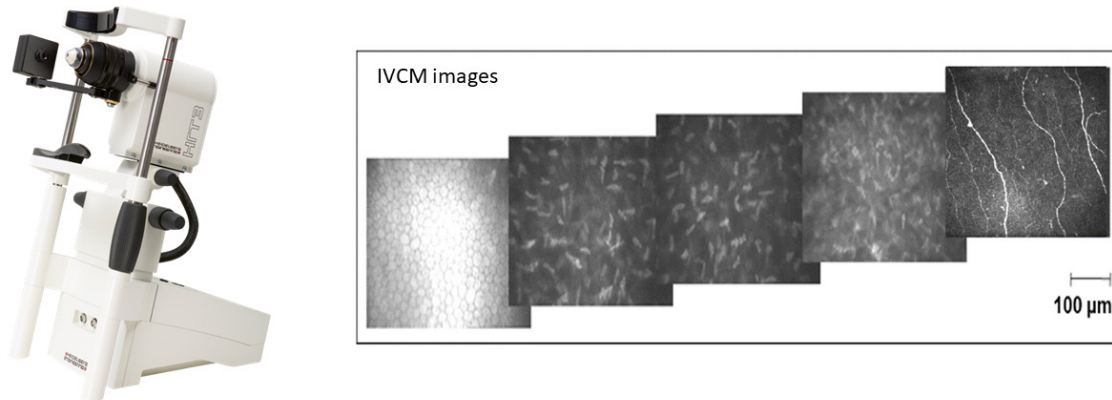
FIGURE 2.8: Heidelberg Retinal Tomograph (left), and images acquired with this tool of various corneal layers (right). From left to right the images represent the endothelium, stroma (3 images), and sub-basal nerve plexus.

To ensure the best possible acquisition, all possible adaptations in the microscope setup must be considered. Therefore, the goal is to improve compliance, position, and comfort and to reduce movement. In the case of the Laser-Scanning Confocal Microscope, a drop of hydroxypropyl methylcellulose is often used; it improves the optical coupling by decreasing the artifacts typical of corneal compression that occur from contact with the instrument (the application of the corneal surface is reduced). For a good final quality, a total of 6 to 8 volume and/or sequence scans from the center of each cornea are recommended.

2.3   Diagnostic window

Thanks to the properties of its layers, the cornea has great resistance to infection. In a healthy cornea, or in a cornea whose layers are intact, the passage of pathogens is prevented. However, as a result of trauma, scratches, inflammation (both exogenous and endogenous), or other events, the integrity of the tissue can be lost, thus affecting the properties of the cornea itself.

In general, pathologies that lead to loss of corneal properties can be divided into the following groups:

- *Inflammatory pathologies*

  They are the most common; generally, the inflammation is caused by bacteria, fungi, or viruses. Sometimes, they can be linked to the misuse of devices, such as contact lenses. The most common and studied pathology is keratitis: it causes corneal opacity and, if not treated, can lead to blindness.

- *Pathologies of the ectatic type*

  It is a group of inherited congenital diseases that are distinguished by an alteration in the normal corneal curvature. The most common is keratoconus: it

causes a reduction in the strength and thickness of the corneal tissue, leading to a variation in the curvature of the structure similar to that of a cone.

- *Degenerative diseases*

  As the name suggests, these are pathologies that lead to the degeneration of the corneal structures. Diseases that are divided into other categories, such as keratitis and keratoconus, are often also part of this group. In particular, there is often talk of neurotrophic keratitis. It is a disease caused by damage to the trigeminal nerve. This damage causes a loss of corneal sensitivity and spontaneous development of epithelial lesions, up to, in severe cases, ulceration, aseptic necrosis, and corneal perforations.

- *Congenital pathologies*

  They are pathologies that occur from birth, but which can manifest themselves in adulthood. They often lead to a reduction in transparency or a reduction in corneal size. Examples are the sclerocornea and dermoid, which cause corneal opacity (even from birth); there are also the microcornea and megalocornea, which lead to reduction and enlargement of the size of the cornea, respectively.

- *Systemic pathologies*

  These are diseases that are not inherent in the cornea but that affect the eye, other organs, or the whole organism. This group includes dry eye syndrome, respiratory tract infections, type II diabetes, Parkinson's, multiple sclerosis, and others.

2.3.1 Corneal nerve in normal and pathological subjects

In the past, the study of corneal nerves was very limited. These were analyses performed *ex vivo* after death and it is known that deterioration and degeneration of the corneal nerves occurred within 15.5 hours [1, 32]. Thanks to the introduction of IVCM, corneal nerves can now be studied and analyzed *in vivo*.

However, the introduction of this instrument did not remove all the obstacles for the study of the cornea: the determination of the values and morphology considered normal in the living human cornea is not always consistent. Furthermore, the definition of characteristics is often inconsistent between the different studies carried out. For example, with regard to the density of the sub-basal nerves, it is sometimes defined as the total length of the visible nerves within a defined area; instead, other times, nerve branches shorter than 50 μm are excluded from the analysis.

Furthermore, the criteria of the definition of nerve fiber can vary [54]. Also the number of visible nerves can vary depending on the instrument chosen instrument (studies using LSCM have reported an increasing density of nerves [2]), and according to the observed region (in the central cornea, the nerve density is significantly

higher than in the peripheral areas [55]). The latter, suggest the importance of choosing the region where to acquire images or the importance of analyzing a certain number of randomly chosen images (not overlapping by more than 20%, as reported in the literature) in order to achieve an acceptable level of accuracy in the analysis [56, 57].

Despite the difficulties encountered, numerous studies have revealed correlations between the quantitative and morphological aspects of nerve fibers with the presence and progression of pathologies. (Similar observations can be made regarding dendritic cells).
For examples, some studies have highlighted how the use of contact lenses can affect the number of nerve fibers present in the cornea, especially in the central area; in addition, this decrease is closely related to a decrease in corneal sensitivity [58, 59].

Keratoconus also leads to some variations in the sub-basal corneal nerves: in addition to a decrease in density, more tortuous nerves were observed than in controls, with abnormal architecture in the cone region [60, 61].

In recent years, a great deal of interest has been directed towards the study of dry eye disease (DED), and corneal nerves have also been taken into consideration. The results presented are conflicting: in some there is no difference between healthy and pathological, while others demonstrate an abnormal nerve morphology (presence of nerve shoots, abnormal tortuosity, increased beading and thinning of nerve fiber bundles) [62, 63]. The variability of the results could be related to different stages and severity of the disease, or to a different level of inflammation. However, studies agree that sub-basal corneal nerve tortuosity is significantly increased [62–64]. In summary, IVCM studies in patients with DED suggest the presence of a link between corneal nerves (function, density and morphology), and the pathogenesis of this disease.

Changes in corneal nerves were then detected in correlation with the treatments of other pathologies: for example, subjects with glaucoma showed a decrease in the density of the sub-basal nerves and an increase in tortuosity after treatment [65, 66].

In addition, IVCM has been shown to be useful for providing an early diagnosis and assessing the progression of systemic diseases involving peripheral neuropathy. This group includes diabetes [67, 68], Parkinson's [69, 70] and cancer (not directly, but due to chemotherapy treatment [11, 71]).

Another very interesting case study is the investigation of alterations after corneal surgery. As mentioned above, IVCM enabled visualization, quantification, and monitoring of progressive changes in nerve and cell immune responses before and after corneal surgical procedures. One of the most analyzed procedures is laser-assisted in situ keratomileusis (LASIK), in which damage to the corneal nerves was detected just a few hours after surgery. However, after a month, the appearance of new thin nerve fibers is observed [72–74].

At the moment, clinical practice remains largely subjective: in particular, the quantification of nerve density, nerve tortuosity, beadings, and the number of branches have not yet been standardized and often depend on the manual identification and tracing of nerve fibers. Indeed, the extraction of the parameters of the

sub-basal nerve plexus is mainly based on manual or semi-automatic techniques, which turn out to be tedious, time-consuming, and subjective. Furthermore, these techniques require experience and are prone to variability between and within observers [75, 76].

Over the years, more and more studies, as highlighted above, have shown the strong utility of the study of corneal IVCM images in the diagnosis, prognosis, and treatment of ocular and systemic diseases. For this reason, numerous studies have tried to standardize analysis [77] and develop fully automated analytical techniques, obviating the problems associated with manual analysis [78–82].

In the next chapters, the proposed automatic solutions will be analyzed in more detail, both for tracing and for the extraction of parameters, especially with regard to tortuosity.

2.4 Automated sub-basal nerve plexus analysis

Automatic analysis of the corneal sub-basal layer is a relatively new research subject. According to subsequent research [2, 83, 84], the first to address the problem was Scarpa et al. [85], in 2008. Generally, the automatic analyses proposed in the literature focus on three main points:

1. The improvement of image quality

   Often these are techniques used in the pre-processing phase, implemented in order to:

   - reduce image noise,
   - improve the contrast and sharpness of the image,
   - correct the lighting (which is not homogeneous in the IVCM images).

2. Detection of structures

   It is a step after the previous one and is often presented together with it. Through techniques of segmentation, description, and classification of single objects, edges, and/or structures of elements present in the images are highlighted, including nerves and dendrites.

3. Extraction of useful features for diagnostic purposes

   It involves extracting the parameters of clinical interest, such as, for example, the number of nerves, their density, morphological characteristics, ...

The sections below briefly report what is the state of the art in the three areas listed above.

2.4.1 Image quality improvement / Pre-processing

By observing Figure 2.9, it is possible to notice how the brightness of the IVCM images is non-uniform: generally, the outermost areas are darker than the central areas. This is due to numerous factors, including the cornea's own curvature, which involves a non-uniform reflection and attenuation of the lighting.
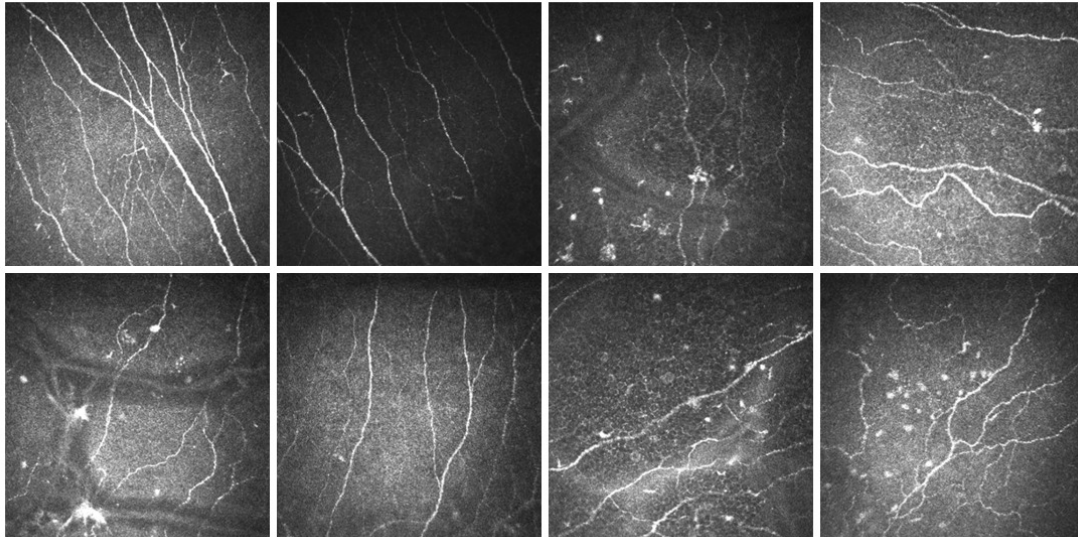
FIGURE 2.9: Examples of IVCM images of the sub-basal nerve plexus, showing the variability between images.

In addition, images often have low contrast and, due to movements during acquisition, can be blurred. Therefore, to improve image quality, different solutions have been proposed. To the best of our knowledge, there are no studies on the effects of this preprocessing phase on the subsequent phases (detection of structures and extraction of clinical features). For this reason, it is difficult to determine which are the most efficient techniques.

Scarpa et al. [85] have already taken into account the problem of non-uniform lighting and have addressed it by developing a specific equalization procedure: the image is considered as the sum of the background of the sub-basal layer and the image depicting the structures present in it. Brightness and contrast are estimated from the image that represents the background. The implemented technique has the disadvantage of increasing the noise amplitude; for this reason a median filter has been applied.

Dabbah et al. [86] also propose a pre-processing step based on the subdivision of the images into two levels: one in the background and one relating to the elements in the foreground. The two levels are modeled separately and work synchronously. In the first version [86], the proposed method improves the contrast of nerve fibers oriented in the dominant direction. Subsequently, the technique was improved thanks to a multiscale approach [87]: all the possible orientations of the fibers are calculated

at each single pixel. Based on the work of Dabbah et al. [87], Chen et al. [88] propose a further step for the reduction of residual noise through an iterative process.

In Zhang et al. [81], the separation of background and foreground elements is conserved and used to develop a method previously designed for the pre-processing of retinal images [89]: the method provides an estimation of the image brightness and contrast drifts. The author himself underlines that the method does not take into account any blurring or additive noise present in the image.

In [79, 84] a contrast-limited adaptive histogram and wavelet transforms are exploited. Similarly, [90, 91] implement a method based on local histogram equalization, dedicated to improving contrast and identifying the best dynamic threshold for noise removal, followed by a step based on local frequency analysis to enhance boundaries.

Before proceeding with nerve fibers, Sindt et al [92] implemented an opening operation in order to reduce the irregularities characterizing the background and thus improve the image quality.

Al-Fahdawi et al. [93] used anisotropic diffusion filtering and Gaussian filtering to enhance nerve contours and remove noise. There are also many studies that address the non-uniformity of brightness and contrast through Gabor filters [85, 94–97], sometimes associated with top-hat filtering, other times used in banks.

In Colonna et al. [98] and Scarpa et al. [99] the problem related to the low light of the peripheral area is addressed by cropping the image: a region of interest is selected, and everything else is discarded. Furthermore, to partially reduce the noise, an image rescaling is performed through a bi-cubic function.

In some cases, image registration techniques have been implemented to reduce image noise, improve contrast, and limit blur, as to well as widen the visible area [100, 101].

2.4.2 Structure detection

The clinical interest in the images of the sub-basal corneal nerve plexus is mainly linked to the analysis of the nerve fibers present in it. Numerous studies have been presented in the literature for the identification and automatic tracing of nerve fibers. To the best of our knowledge, none of them have yet been included in the diagnostic process.

In Scarpa et al. [85], after contrast enhancement through Gabor filters, several steps are performed. First, the pixels used as seed points are highlighted by an empirically determined threshold. The seed points work as starting points from which the direction of the nerve is found, and subsequently, according to the fuzzy c-means technique, they are classified in each cross section as belonging to the nerves or to the background. The consecutive pixels determine the nerve fibers. To further improve the result already obtained, the authors present a post-processing step, called the *two-carabinieri* (policeman) procedure. This step allows analyzing five possible connections between two end points. The connection composed of image pixels with

the brightest average gray-level intensity is selected as the candidate connection, and *two-carabinieri* arcs are drawn. The two arcs are shown on each side of the candidate connection at an empirically determined distance. The candidate connection would be accepted as a true connection if the difference between gray-level intensity of the candidate connection and those of the *carabinieri* is larger than an empirically determined threshold. The same technique, adapted to images of a different instrument, is also used by Scarpa et al. [97].

Holmes et al. [102] proposed the trace of corneal nerve fibers using segmentation and skeletonization techniques based on the calculation of the ridge map (the ridge map is described by a set of labeled pixels that are obtained from the analysis of an intensity gradient image).

In Ferreira et al. [90], tracing is developed according to the growing techniques of the region, after obtaining a binary image using thresholding techniques. Thanks to several morphological operations, the morphological skeleton of the image is computed, and branches, which are too short or do not respect certain characteristics, are removed. Furthermore, by growing the region, the nerves are reconstructed to their original dimensions. The same procedure was implemented by Otel et al. [91].

The same authors, in Ferreira et al. [84], promote a new method based on the analysis of phase symmetry, filtering of the wavelet transform. Thanks to these techniques, it is possible to identify the nerve structures and, subsequently, thanks to morphological operations, it is possible to reconstruct the nerve fiber itself: the seed points are extracted, the wrong structures are discarded, and the skeleton is calculated.

Subsequently, Dabbah et al. [87], after the enhancement technique based on the multi-scale approach, implement random forests and artificial neural networks for the classification of each pixel as a foreground or background pixel. Through the multi-scale approach functionality vectors are generated from information located on each pixel, which are used as inputs for the aforementioned techniques.

The pre-processing of Chen et al. [88] was based on the latter [87], including segmentation. In this study, the best configuration is investigated to obtain the trace of the corneal nerve fibers.

Sindt et al. [92], rejoin branches represented by nerves by closing operations. This is done after applying a hysteresis threshold to generate a binary image. However, the method is not completely automatic: further manual manipulations may be necessary to remove segments that represent other structures in the image (e.g., dendritic cells), to add some unrecognized branches in the automatic analysis, and to merge those branches that have been broken.

Poletti and Ruggeri [103] propose a new approach through a scattered tracing scheme: after the identification of the seed points, these are grouped looking for a path of minimum cost path whose weights have been estimated considering different directional measures. Poletti et al. [101] is also based on this work. This study is related to the offline montage of confocal microscopy images of the living human cornea, which requires the tracing of individual starting images.

Annunziata et al. [104] present a hybrid segmentation method, which combines an appearance model, based on a Scale and Curvature-Invariant Ridge Detector (SCIRD), with a context model, including multi-range learned context filters.

In the same year, Al-Fahdawi et al. [93] present a three-step segmentation model. After the pre-processing step mentioned above (based on diffusion filtering to enhance nerves and remove noise), morphological operations are applied to remove unwanted objects, such as epithelial cells and small nerve segments. Finally, edge detection techniques (Canny technique) are used to detect all the nerves in the input image.

In the same year, Guimarães et al. [105] propose a method for the segmentation of corneal nerve fibers. This procedure, as previously mentioned, involves processing the image through a bank of filters, which also includes the log-Gabor filter. Then, hysteresis thresholding was used to identify candidate nerve pixels, and each pixel was subsequently classified through a support vector machine.

In Salahuddin and Qidwai [106], after applying Gaussian and coherence filters as pre-processing steps, the smoothed image is subjected to binarization. The result is an image in which the white pixels represent the nerve fibers: they are often broken and need to be rejoined. This is achieved through a sequence of morphological operations (dilation, erosion, opening, closing, and skeletonized through the medial axis transform algorithm). Starting from these operations, the useful features for training the neuro-fuzzy classifier proposed in the paper are obtained. Other classifiers were investigated in a subsequent study [107].

One of the most common problems encountered with regard to the methods presented so far is the execution time. In most cases, hundreds of seconds are needed to analyze a single image. Furthermore, there is no excellent correspondence with the manual tracing performed by expert clinicians.

In Dehghani et al. [108], the abilities of automatic, semi-automatic and manual methods were analyzed to detect a decrease in the length of corneal nerves in patients with diabetes. What the study found is interesting: all three approaches are capable of distinguishing between healthy subjects and subjects with diabetes, but the analysis performed manually was better able to distinguish subjects, especially in low-contrast images. These results reveal the need to develop algorithms that better emulate human analysis knowledge.

Recent years have yielded new results obtained through deep learning techniques: these techniques have been shown to significantly reduce the analysis time (they require time for the training phase, but subsequently, their application is almost immediate), and sometimes have also been shown to surpass human capabilities in numerous fields.

In Colonna et al. [98], we presented the first study in which nerve fiber segmentation is performed using deep learning techniques. After simple pre-processing operations, the images were segmented through a convolutional neural network based on the UNet architecture. Deep learning techniques require a large dataset for the training phase. As there were no sufficiently large datasets analyzed manually, the dataset

used as ground truth was obtained starting from another algorithm presented above [95].

Subsequently, other works have also presented studies based on the UNet architecture for the segmentation of corneal nerve fibers. Zhang et al. [81], after performing some pre-processing steps for image normalization, analyzes the images by regions (in order to fit the data into the memory of the graphic card) through a network with UNet architecture. Mehrgardt et al. [109] present a method based on the UNet architecture: called UNet segmented adjacent angle detection (USAAD).

2.4.3   Extraction of features useful for diagnostic purposes.

Most studies that have dealt with the issue of obtaining characteristics for diagnostic purposes are preceded by the phases described: image preprocessing and identification/tracing of corneal structures [7, 8, 11, 79, 81, 82, 84–88, 96, 97, 104–107]. There are also some studies that overpass the pre-processing and tracing phases, providing a direct classification of the image [98, 99, 109].

Various quantitative parameters have been taken into account in the literature: the most common are nerve length, nerve density bifurcation density and tortuosity [27, 79, 84–88, 90, 92, 93, 95, 96, 102, 104, 105, 110]. Other parameters, such as nerve fibers, were analyzed to locate the corneal image within the entire corneal structure and, therefore, obtain a more accurate comparison between different patients. It is important to emphasize that the IVCM has a small field of view that allows access to only a small corneal region [75, 78, 96, 111]. In Cruzat et al. [2] it is reported that a single image covers only 0.15% of the entire corneal surface.

Other parameters frequently taken into account are: the width of the nerve fibers [88, 91, 93, 112], the number of nerve fibers [79], the area of the nerve fibers [88, 106, 107] the entropy [106, 107], the number of branch segments in the image [102], and others.

To evaluate the automatic results, various performance and evaluation metrics were taken into account. At times a comparison was made with the indices calculated by manual analysis, and at others the ability of the aforementioned indices was observed to distinguish between normal and nonnormal subjects. Sensitivity, specificity, and correlation coefficients were the most frequently analyzed. However, the application of different definitions of sensitivity and specificity also makes it difficult to conduct a direct general comparison of the results in the literature [113].

In the chapter related to tortuosity estimation, the analysis of tortuosity, its definition, and its use for diagnostic purposes will be reported more specifically.

Chapter 3

Nerve Tracing

Deep learning algorithms have quickly become the state of the art in terms of the main methodologies applied in the analysis of medical images. These modern techniques have shown a powerful learning ability and great advantages in dealing with complex patterns problems. Deep learning has shown great potential in challenges linked to image analysis, especially in the field of digital pathology. The variety of image analysis tasks in the context of deep learning include classification, object detection, and semantic segmentation. Often the part of the framework based on deep learning algorithms is preceded by a pre-processing phase and followed by a post-processing phase, both based on traditional image processing methods.

This chapter describes the deep learning techniques implemented for the tracing of corneal nerve fibers. The pre-processing phases, developed to improve the results, and post-processing, developed to perform an evaluation from the comparison with manual analysis, will also be presented.

In this chapter, the results obtained will be discussed. These are the results achieved starting from an analysis presented in [98].

3.1   Material

The images collected at a specific depth of the corneal layers, the sub-basal plexus, allow the visualization of the nerve structures present in this section of the cornea. The tool used for image acquisition is the Heidelberg Retina Tomograph (HRT-II) with the Rostock Cornea Module (Heidelberg Engineering GmbH, Heidelberg, Germany). The images cover a field of 400 x 400 μm2, corresponding to 384x384 pixels, which represent only 0.15% of the entire corneal surface [2, 12]. These are grayscale images that allow the visualization of nerve fibers and other structures of the sub-basal layer. Figure 3.1 shows two images, in which some of the present structures are highlighted.

The acquisition of the images used for the development and testing of the tracing algorithm was performed in different clinical centers, furthermore all data was anonymized, and all patient information deleted.

There are very few public datasets available (especially with regard to datasets in which the nerve fibers of the sub-basal plexus are manually traced), and those that are
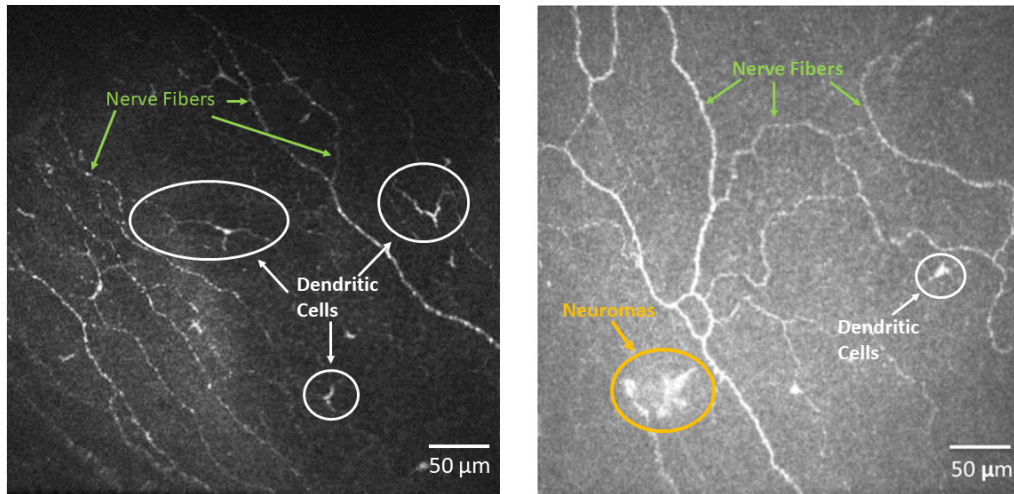
FIGURE 3.1: Examples of IVCM images of the sub-basal nerve plexus,
showing the structures that are present. The dendritic cells, circled in
white, the neuroma is circled in orange, and some nerve fibers are indi-
cated by green arrows.

publicly accessible present a very limited number of images, which is not sufficient
for the development of a solid and stable deep learning algorithm.

For the development and training phase of the convolutional neural networks
analyzed, 8909 images from healthy (6151 images, 85 subjects) and pathological
(2758 images, 424 subjects) subjects were used. Images may be partially overlap-
ping and may present noise (nonuniform luminosity and contrast, the presence of
other corneal layers, etc.). In Figure 3.2 there are some images that represent the cases
of greater noise.

Since the development of supervised deep learning techniques requires objective
images (called ground truth, which refers to what the network must learn to obtain
from the original images), to develop a deep leaning algorithm, we would need man-
ual analysis of all 8909 images.

As pointed out in the previous chapters, manual analysis is a difficult, laborious,
time-consuming, and boring task. To overcome this problem, it was decided to use
the tracing obtained by another algorithm proposed by Guimarães et al. [95]. This
algorithm was chosen because it has been shown to have good performance in trac-
ing the centerline of the nerve fibers. Furthermore, in [98] we have already verified
the ability of a deep learning algorithm to generalize well (by extracting the charac-
teristics that correctly describe the nerve fibers) and therefore provide better tracing
than that used as the ground truth.

For the testing phase, 90 images were used. These were acquired with the same
procedures as the previous ones, from 45 healthy subjects and 45 pathological sub-
jects. This set was used to evaluate the performance of the proposed algorithm,
and, to do so, all 90 images were manually analyzed by an expert. For each im-
age, the centerline, which identifies the corneal nerve fibers present in the images,
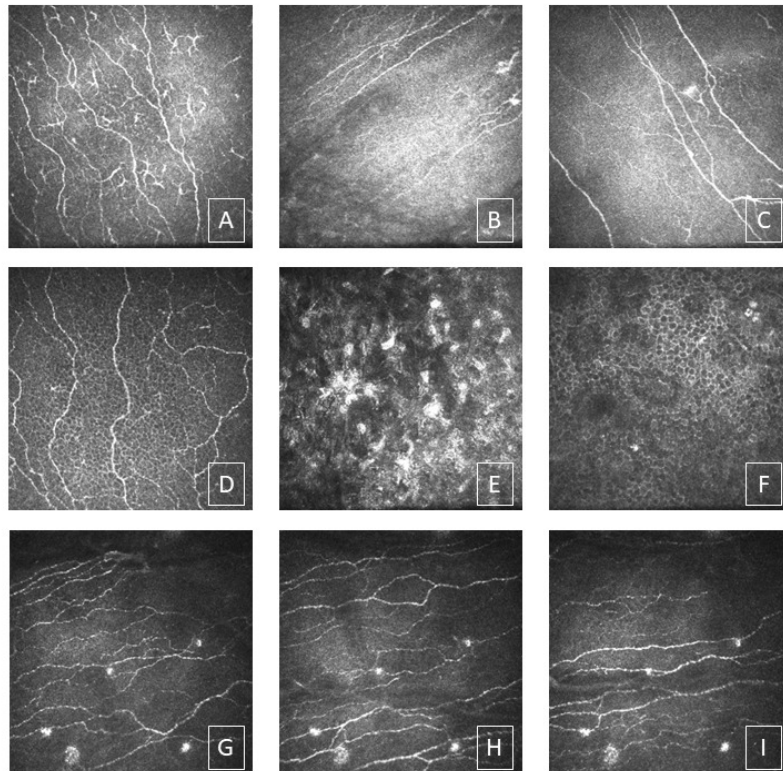
FIGURE 3.2: Examples of images of the training set that present particular noise. The first line (A-B-C) highlights the non-uniformity of the illumination, mostly linked to the sphericity of the cornea; the central row (D-E-F) shows images presenting layers other than the sub basal (D-F include the epithelium, E shows the stroma); the bottom row presents images acquired with the dirty microscope; in fact the noise is given by the repetitive spots that occur in different areas of the cornea.

was traced. The analysis was performed using NeuronJ [114], tracing plugin for ImageJ (the software is available in the public domain at http://imagescience.org/meijering/software/neuronj/).

3.2 Pre-Processing

The term 'pre-processing' refers to all the strategies applied to the raw data (i.e., to the entire image acquired by the instrument) in order to optimally prepare the network input and obtain a more robust and accurate final model.

Numerous pre-processing steps have been proposed in the literature, all aimed at improving the effectiveness of the algorithm training: it seems that the performance of convolutional neural networks is influenced by the pre-processing techniques used. However, there are few studies that verify whether the pre-processing of the image actually brings a great change in the results.

From the literature, we found that image preprocessing does not drastically affect the result of the network, but does affect its convergence speed. For this reason, in

all tested networks, it was decided to insert a very simple pre-processing step of the image suitable for normalizing data and anticipating convergence.

Only for a part of the proposed algorithms, a further pre-processing step defined as 'pixel-wise modification' was performed. The latter is described below.

3.2.1   From skeleton to pixel-wise

For the semantic segmentation, the goal is to obtain a pixel-wise prediction of the image under analysis, delimiting a precise boundary of the desired objects (in this case of the nerve fibers).

As specified in the chapter on materials, the clinical analysis that leads to the tracing of corneal neural fibers reports only the centerline of each nerve. Therefore, clinical practice involves tracing the skeleton after recognizing the pattern that identifies all the pixels belonging to the nerve.

Furthermore, since semantic segmentation is a technique that searches for pixels that belong to a structure, in order to improve the convergence of the algorithm during the training phase, we tried to emulate clinical practice. It means, first highlighted all the pixels that identify the structure under analysis (nerve fibers), and then, identify the central line. Some of the networks analyzed were trained and subsequently tested after applying the additional pre-processing step to the images, which try to emulate the steps of the clinical practice.
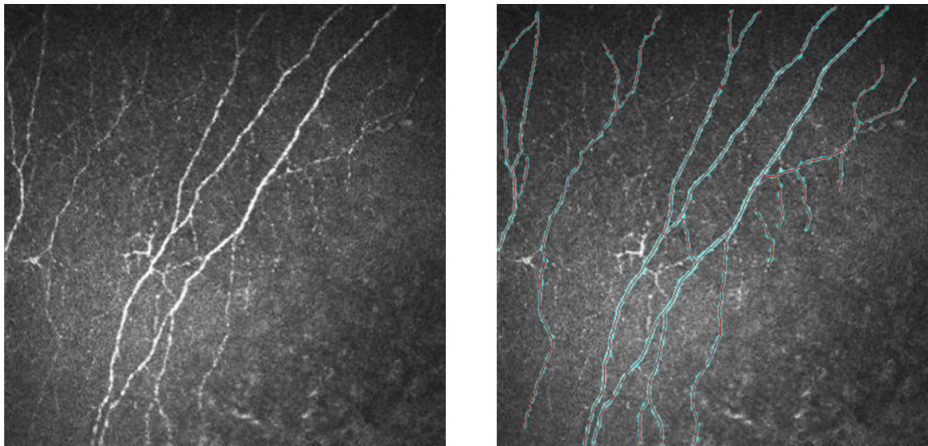
FIGURE 3.3: Original image on left, traced image on right: in red the centerline, in cyan the region (pixel-wise analysis).

This step involves editing the objective images. The original image is subjected to targeted filtering and local thresholding operations, in order to obtain a black and white image (BW-image), that highlights the brighter structures of the starting image. Subsequently, comparing the BW-image obtained and the ground truth representing the central lines of the nerve fibers, using region-growing and morphological operations, all the pixels belonging to the nerves are detected.

The images obtained will be used for the network training phase. Using the region instead of the central line allows providing the network with more information. Figure 3.3 shows an example of the result of this first analysis.

3.3 Convolutional neural network - CNN

Recently, computerized approaches have been further developed in the field of medical imaging. These approaches aim to provide clinical information (both diagnostic and prognostic), integrate second opinions, and limit, where possible, human error. Among the most developed methods of recent years are deep learning methods: various studies show how these cutting-edge techniques are approaching human performance in a series of tasks, sometimes surpassing them.

In addition, the increasing digitization of clinical studies and the consequent increase in the available size of the data sets, aided by an increase in computing power, have led to the development and widespread application of convolutional neural networks (CNN). In particular, this technique aimed at the study of images (both in the medical field and not): they can be applied to the entire image under analysis or to patches of the same. The network is trained according to a weight update process, based on a specific loss function. Once the training phase is complete, the network is then used for inference on new images or patches. The training process can be long (it can take hours, days, or months), but once trained, the network can perform in less than a second.

Speed of action is just one of the benefits of these new techniques. Another fundamental advantage linked to these techniques is the ability of such an algorithm to automatically learn useful high-level features. This is in contrast to traditional techniques, which rely heavily on manually made quantitative feature extractors.

Although deep learning techniques bring significant advantages, presenting themselves as a powerful tool for automated image analysis, they are not without drawbacks. Precisely because these networks are able to learn high-level features directly and automatically, they are sometimes seen as a black box: it is not easy to extrapolate the information on which their predictions are based. The higher-level features are incomprehensible to humans and are therefore not appreciated by the clinician.

However, the advantages often outweigh the disadvantages, and CNNs are becoming increasingly used in everyday life, becoming the most used method in image analysis. In addition, in the medical field, and in particular in the ophthalmic field, the first automated image analysis systems were introduced. In 2018, the FDA approved the first AI-based autonomous diagnostic tool in any field of medicine [115, 116], it is the first inserted into clinical practice and it regards retinal analysis for the detection of retinopathy of prematurity.

In the literature, numerous architectures are proposed, each aimed at improving performance more and more. In this regard, the simplest method to improve the

predictive capacity of a CNN is to increase its size: this includes both the increase in depth (i.e., the increase in the number of levels), and the increase in width (i.e. the increase in the number of filters or their size at each level). However, such approach is not the best solution: increasing the size requires more data for learning and, at the same time, could lead to overfitting. Another disadvantage, to be taken into consideration, is related to the increase in the size of the network, which requires the significantly increased use of computing resources.

To avoid an excessive increase in the size of the network and, therefore, to avoid the problems mentioned above, several solutions have been proposed in the literature to improve performance without strongly affecting the quantity of parameters to be estimated during the train phase. These are related both to the insertion of connections and/or modules, and to the use of specialized loss functions.

The basic structure on which the nerve tracing is based and its modifications via connections and modules will be presented in this chapter. The analyzed and proposed loss functions will also be presented.

3.3.1   UNet as Baseline

UNet [117] was chosen as the baseline for nerve tracing, it has proven to be an excellent framework for semantic segmentation of biomedical images in general [118–120] and for IVCM images [98, 109, 121, 122], in particular. The architecture used is made up of the encoding and the corresponding decoding units with four-layer depth. Furthermore, it was decided to keep the input image and output one of the same sizes as the original images (384x384 pixels). A graphic explanation of the network under analysis is shown in Figure 3.4.

Briefly, the encoding path of the network is composed of four-levels of depth, each formed in turn of 2 convolutional blocks. The convolutional block consists of two convolutional units, which are composed of convolutional layers (which allow to extrapolate the necessary features), followed by batch normalization (to increase the stability of the U-Net) and a ReLU layer as a non-linear activation function.

Each convolutional block is joined to the next block through a max-pooling layer, whose window is given by a generic 2x2 filter. This operation allows to reduce the xy dimensions of the feature maps by performing a down-sampling of half of the original xy dimensions.

The last convolutional block of the encoding part is linked via the max-pooling layer to another block, called 'bridge block'. This part of the network is composed of two convolutional units (as the ones describe above) and is followed by a transposed convolution, which determines the beginning of the decoding process.

The decoding path consists of four-level depths. Following the path of the information along the network, after the bridge block, we find the transposed convolution, which allows to double the xy dimensions of the features maps it receives in input (therefore, acts as the opposite operation of the max-pooling in the encoding part).
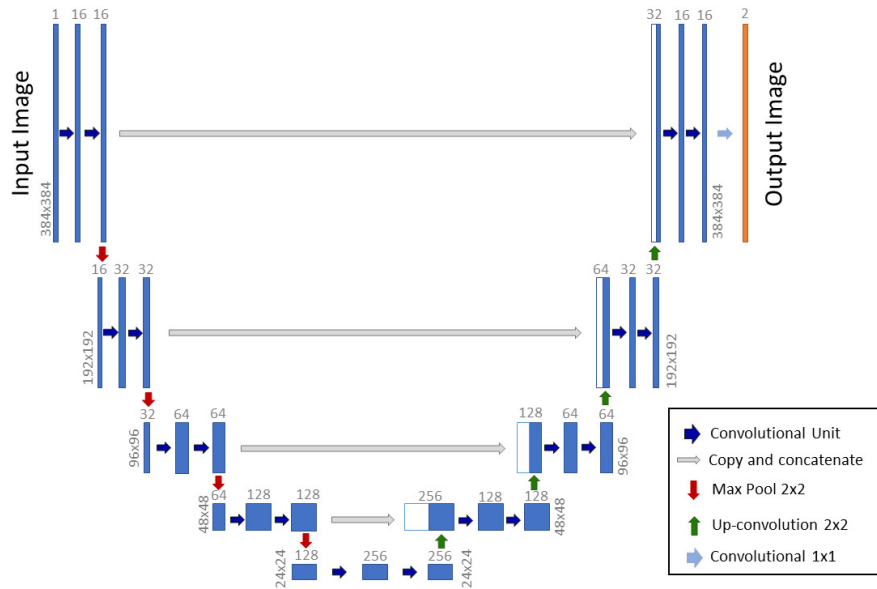
FIGURE 3.4: Neural Network architecture: U-net. Each blue box corresponds to a 3D dimensional tensor. The number on top of each box denotes the number of channels (number of filters). The numbers at the lower left edge of the box provide the xy-size. White boxes in the decoder part represent the concatenated tensor correspondent in the encoder part. The arrows denote the different operations.

The output generated by the transposed convolution is concatenated with the corresponding feature maps in the encoding path (in the figure, the concatenation can be recognized by looking at the gray arrows).

The feature maps thus concatenated are given as input to two convolutional units (which have a structure similar to those presented in the encoding path). The output of these last blocks is passed to a transposed convolution. The *transpose convolution - concatenation - convolutional unit* structure is repeated in the same way until the desired output size is reached, which in our case corresponds to the *xy* dimensions of the original image.

Once the correct *xy* dimensions are reached (after four decoding levels), the information goes through a last convolution layer: it is a $1x1$ convolution, which allows to obtain two feature maps (one for each desired class - nerve / background), and a sigmoid as activation function. The result thus obtained will be two probability layers, each showing the probability of "how likely it is, for each pixel, to be part of a nerve fiber" and "how likely it is, for each pixel, to be part of the background", respectively.

Compared to some versions of the UNet presented online (including also the one provided in MATLAB), it was decided to structure the UNet without the use of dropout layers. It has been analyzed that the introduction of dropout layers and batch normalization (BN) at the same time tends to increase the time required for convergence and, often, leads to sub-optimal results. This is related to the fact that when (for limited mini batches with respect to the total size of the dataset) the mean and variance are calculated by BN, a noise related to the individual iteration is obtained

and the ability to generalize is reduced [123, 124].

The UNet, as mentioned previously, has proved to be an excellent structure for the semantic segmentation of images in the medical field. Basically, the network learns the "what" information in the encoding phase, losing the "where"; in the decoding phase, on the other hand, it retrieves the "where" information by applying a gradual up-sampling and keeping track (through the concatenations) of the information that had been lost in encoding. In a first analysis [98], the network proved to be capable of promptly providing very promising results in the semantic segmentation of the corneal nerves of the corneal sub-basal layer.

3.4   Additional connections and modules

The UNet just presented was considered as a baseline for more complex models: the ability to improve performance by introducing connections and additional modules was analyzed. In particular, the residual connections, the atruos-spatial pyramid pooling (ASPP) module and attention modules were examined.

3.4.1   Residual connections

As explained above, data flows through the layers of the network: the output of one layer is the input to the following layer. The residual connection provides an alternative path for the data to reach a certain part of the network. This alternative way is useful in the training phase of the network: in fact, the training of a deep network is usually very difficult, due to problems such as the explosion of gradients and the disappearance of gradients.

Numerous studies have investigated the ability of adding residual connections to improve the performance of CNN in analysis [122, 125, 126]. It has been shown that this insertion helps to fight the vanishing of the gradient and the degradation of accuracy [127], also increasing the performance of the network [122, 125, 126]. Therefore, it is empirically observed that the process of training a CNN residual connection converges much faster than the same architecture to which the connections have not been added.

However, as with a large number of techniques related to deep learning, we still don't fully understand all the details about how the residual connection works.

Figure 3.5 shows a graphic explanation of how a residual connection is inserted and how it is structured. The residual connection is introduced between the input and the output of each convolutional block of the network, in both the encoding and the decoding paths.

The outgoing features maps from the convolutional block have a z dimension (number of calculated features maps) different from the incoming one (respectively doubles in the encoding part and halves in the decoding phase). To overcome the
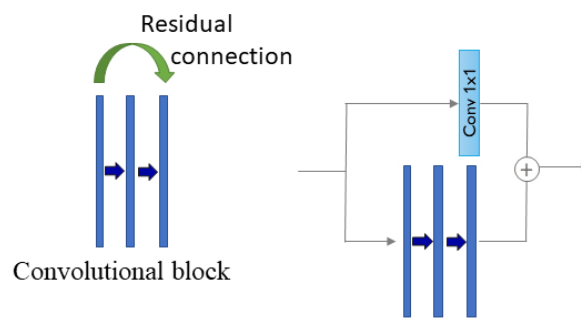
FIGURE 3.5: Residual Connection: on the left, graph of how the residual connection is inserted with respect to the convolutional block, on the right detailed implementation of the connection.

problem related to the diversity of the input and output dimensions of the convolutional block, a $1x1$ convolution is inserted within the residual connection, to adjust the number of features and allow adding the residual to the new tensor.

3.4.2 Atruos-Spatial Pyramid Pooling (ASPP) module

The introduction of the atruos-spatial pyramid pooling (ASPP) module is linked to the need, according to some studies, to extract more semantic information in image segmentation problems. Therefore, this module allows obtaining information on a multi-scale context, through the use of convolutions that have different dilation rates.

Convolutions can be performed separately in parallel as proposed in Chen et al. [128]. Otherwise, it can be used the structure called waterfall, in which the input of the branches with a higher dilation rate, is given by the output of the previous branch, as proposed in Artacho and Savakis [129].

Given the good results found in multiple studies, the structure proposed in Chen et al. [128] has been taken into consideration. The implementation of the module is shown in Figure 3.6. The ASPP module is introduced between the bridge block and the first convolution unit of the decoding path.

Four branches are created and placed in parallel. The first three branches are similar to each other: they have a convolution, followed by a normalization, and an activation function. The difference is recognizable in the dilation rate of the convolutions of each branch: the first has a dilation factor of 1, the second of 2 and the third of 4. The last branch consists of a global average pooling: this operation allows to extract an image-level feature.

After performing the operations in parallel, the outputs of each branch are concatenated (it can be seen that an up-sampling layer has been inserted in the branch of the global feature: this is necessary to bring the output feature maps to have the same size as the other branches).

Once the outputs are concatenated, they are first subjected to a $1x1$ convolution operation and, subsequently, to a normalization layer and an activation layer.
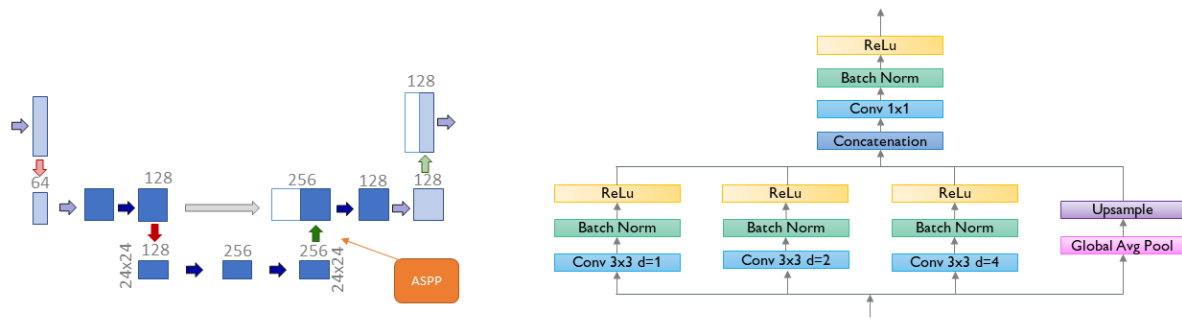
FIGURE 3.6: Atrous-Spatial Pyramid Pooling (ASPP) module: on the left, graph of how it is inserted with respect to the bottom of the UNet, on the right detailed implementation of the module.

3.4.3 Attention Module (AM)

The attention module (AM) was implemented with the idea of an application different from semantic segmentation. It was first proposed for the classification task [130]. The basic idea was to develop a module capable, through certain operations, of analyzing with greater attention those regions of the image that have the greatest influence on the prediction of the model, suppressing information that is not relevant, such as the background, and highlighting those of greatest interest, hence the name attention module or attention gate.

Given the good results, the idea was adapted and generalized to improve performance in other fields of application, including segmentation tasks [119, 131]. In semantic segmentation via UNet, the attention module amplifies the spatial information coming from the skipped connections and reduces the weights of background features.

As for the UNet, during the up-sampling of the decoding path, the recreated spatial information is inaccurate; for this reason, the skipped connections are inserted. They combine spatial information from the down-sampling path with the up-sampling path. However, this method causes a redundant extraction of low-level functionality. The introduction of attention modules on these connections allows to actively suppress activations in irrelevant regions, reducing the number of redundant features introduced, reducing computational resources, and leading to a better generalization power.

The module was implemented as described in Schlemper et al. [131]. As schematized in 3.7, the module is inserted within each of the skipped connections that derive from the encoding path. It takes as input the information deriving from the skipped connections (gray arrow of the main UNet scheme) and from the transposed convolutions of the decoding branch (green arrow of the main UNet scheme). Both inputs perform a $1x1$ convolution to obtain the same number of features maps. Then, the features maps obtained are added, the ReLu activation function was applied, and a further $1x1$ convolution operation followed by a sigmoid activation function was

inserted. At this point, the information is multiplied with that relating to the $1x1$ convolution of the transposed convolution data. The output thus generated is concatenated with the up-sampled data.
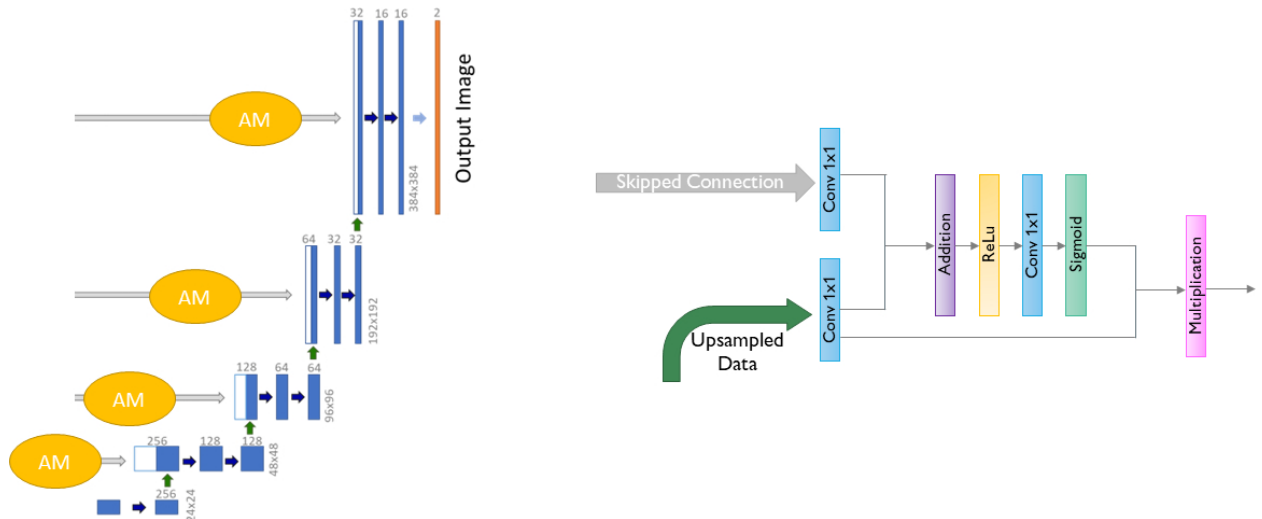
FIGURE 3.7: Attention module (AM): on the left, graph of how it is inserted with respect to the skipped connections of the UNet; on the right, a detailed implementation of the module.

The addition of the attention module has been shown to outperform a normal U-Net in overall performance [119, 132, 133]. Although the UNet with the addition of AM has a greater number of parameters, the inference time is only slightly longer and therefore not relevant in the overall analysis.

3.5 Loss Functions

The learning process of a deep learning algorithm is highly dependent on the loss function chosen when designing the architecture training phase. This is the function that allows measuring the degree of accuracy with which the model describes the empirical data of a given phenomenon. It means that the loss functions can put in relation the value predicted by the model and the correct one (the ground thruth), obtaining a measure of goodness of the result generated by CNN.

Thus, during the supervised training process, the loss function provides the model with feedback on how well it is converging to the model's optimal parameters: it serves as a guide for finding the "ideal" approximation (computation of network weights) that associates the input data to the output data. Based on this measure of accuracy and thanks to a stochastic approach for the descent of the gradient, the algorithms are optimized and learn the objective.

Therefore, for fast and accurate learning, the loss function must be able to mathematically represent the target, even in its borderline cases.

Numerous loss functions have been presented in the literature, each aimed at best describing the goal to be pursued and improving results for their datasets. The first

loss functions were introduced in traditional machine learning and were based on the distribution of the labels [134].

During the Ph.D. program, the capacity of some of the most commonly used loss functions for semantic segmentation was investigated and one aimed at improving the performance of the corneal nerve fiber tracing networks was introduced. Furthermore, the latter has been combined with a loss function present in the literature to obtain a further increase in performance. The loss functions analyzed will be briefly presented below.

3.5.1   Balanced Binary Cross-Entropy Loss (BBCE)

Balanced Binary Cross-Entropy is a variant of the well-known Binary Cross-Entropy (BCE), which is defined as the difference between two probability distributions for a given random variable [134].

The BCE is used for both classification (in a more general sense) and segmentation. The binary cross entropy loss is generally based on the Bernoulli distribution; its operation is better in the case of an equal distribution of data between classes. That is, images' masks with a very heavy class imbalance (such as in finding thin, sparse nerve fibers in IVCM images) may not be adequately assessed by BCE.

This is due to the BCE definition: it treats positive samples ('nerve fibers' in our case) and negative samples (everything that does not belong to nerve fibers and is therefore generically classified as 'background') in the same way; as a consequence, the BCE loss may not effectively represent mathematically the goal of the deep learning model in the case of corneal nerve fiber tracing. Therefore, when it comes to working with unbalanced data, an adaptation of the BCE is used: its balanced variant called Balanced Binary Cross-Entropy (BBCE). It allows giving weight to both positive (β) and negative ($1 - \beta$) examples. It is widely used in medical imaging (and other areas with highly unbalanced datasets). It is defined as follows:

$$L_{BBCE} = -\beta * ylog(\hat{y}) + (1 - \beta) * (1 - y)log(1 - \hat{y})$$

where y represents the True value, and $\hat{y}$ the predicted value. β is the weight related to the True value in the images and it is often derived from the frequency of the True value in the image. By varying the values of β it is possible to pay more attention to the reduction of false positives or false negatives.

Although the variant allows taking into consideration the imbalance of the data, the BCE (and consequently its variant, BBCE) has a further limitation: it calculates the loss as the average of the loss per pixel, without considering the adjacent pixels, and, therefore, without considering the continuity of the object to segment.

3.5.2   Dice Loss (DL)

Dice loss is another loss function widely used in the field of artificial intelligence, especially in the training of CNN aimed at the semantic segmentation task [118, 135]. It

is based on the coefficient of the same name (Dice coefficient, [136]), which calculates the similarity between two images, considering the overlap between the two samples, similar to the heuristics Intersection-over-Union. The Dice coefficient is defined as

$$Dice = (\frac{2|Y \cap \hat{Y}|)}{(|Y| + |\hat{Y}|)}$$

where $|Y|$ (respectively $|\hat{Y}|$) represents the number of pixels of object (nerve fibers in our case) in the True set Y (respectively predicted set $\hat{Y}$), and $|Y \cap \hat{Y}|$ represents the common pixels between the two datasets. The coefficient can be rewritten in an equivalent way as:

$$Dice = \frac{2\ TP}{2TP + FP + FN}$$

This definition allows us to highlight how false positives (FP) and false negatives (FN) are weighed equally, and consequently precision (proportion of nerves correctly identified among the true nerves) and recall (proportion of nerves that are correctly identified) are also weighed in the same way.

The Dice loss function is derived from this coefficient. Since the intent is to optimize the Dice coefficient (so the goal is to maximize it), the directly linked loss function (and which we want to minimize) is given by:

$$L_{Dice} = 1 - Dice$$

However, the Dice coefficient is not without its pitfalls: the most important is the possibility of running into the explosion of gradients. At the beginning of the training, the Dice coefficient is close to 0. This fact generates a certain instability during training, and therefore, due to the explosion of the gradients, the net makes big changes to the weights. However, this problem is easily managed thanks to the introduction of batch normalization and ReLU operations.

Therefore, it is a loss function that presents a simple solution to class imbalance without having to manually optimize any parameters, but at the same time has the potential for gradient explosion and it is generally slower to train than BBCE.

3.5.3 Tversky Loss (TL)

As said before for Dice Loss, The Tversky Loss function [137] derives from the homonymous coefficient [138].

The Tversky coefficient is considered a generalization of the Dice coefficient, seen above: unlike the previous one, it allows setting different weights for false positives (FP) and false negatives (FN). The Tversky coefficient is defined as:

$$Tversky = \frac{TP}{TP + \alpha * FP + \beta * FN}$$

It is interesting to note that setting $\alpha = \beta = 0.5$ the Tversky index simplifies to be the same as the Dice coefficient. Therefore, by tuning of the values of α and β it is possible to increase the emphasis on FPs or FNs, respectively. Moreover, increasing the value of β more and more, the emphasis of FNs is increases (this means that the algorithm tries to decrease the presence of FNs), which translates into boost recall, hence achieving better performance in terms of precision-recall trade-off. Starting from the Tversky coefficient, the corresponding loss function is obtained as:

$$L_{Tversky} = 1 - Tversky$$

Although the Tversky index, consequently the loss function obtained from it, is only a simple improvement with respect to the dice coefficient, it can be fundamental in borderline cases, i.e., those cases in which a finer level of control is required.

3.5.4   Focal Tversky Loss (FTL)

The Focal Tversky Loss [139] is a further variant of the Dice coefficient. Starting from the variant just described for the Tversky coefficient, its 'Focal' version provides for the insertion of a focal parameter γ. The purpose of this factor is to try to learn from the more complex examples: i.e., examples with small regions of interest. The non-linear nature of the FTL loss gives you control over how the loss behaves at different values of the tversky index obtained. In fact, it is defined as:

$$L_{FT} = (1 - Tversky)^{\frac{1}{\gamma}}$$

where γ allows to control the non-linearity of the Loss. Essentially, a value of $\gamma = 1$ simplifies the loss function to the Tversky Loss; while with a value of $\gamma > 1$, it increases the degree of focusing on more difficult examples. The optimal value reported in [139] was $\gamma = 4/3$, which improves rather than suppresses the loss of easy examples. In fact, when the model reaches the end of the training, which is when most of the examples are confidently classified at the pixel level (the Tversky index approaches 1), a value of $\gamma > 1$ increases the value loss, thus preventing premature convergence to a non-optimal solution.

In the cases of unbalanced data, such as those of corneal nerve fibers, FTL is useful if we consider a value of $\gamma < 1$. In this way, in fact, when the Tversky index has a value less than 0.5, the gradient of the loss function has a high value. This leads the model to increase the attention to learning hard examples, such as small-scale segmentations that usually receive low TI scores.

In Abraham and Khan [139], a comparison is reported between the loss functions based on the coefficient of Dice, on that of Tversky and on its FTL generalization. Looking at the results presented, the models trained with FTL did not always show the highest precision and recall values in absolute terms. However, it is important to note that the balance between the two evaluation indices, and therefore between

precision and recall considered at the same time, proved to be the best in the tested models.

3.5.5 Dice with Tolerance Loss

In manual analysis of corneal nerve fibers, what is usually done is to draw the central line that identifies each nerve fiber present in the image. Therefore, this line is representative of a larger region and, since the research for the exact center of the region is not trivial, it is customary to take into account a margin of tolerance. That is, it is correct to set a tolerance margin within which a nerve fiber can be recognized (i.e., a pixel recognized to be a nerve will be accepted as TP if it was within the tolerance margin from the reference nerve).

Starting from this assumption and knowing that the goal of the analysis is to recognize and segment the nerve fibers present in an image, trying to maximize both precision and sensitivity, a loss function was developed.

The Dice loss has been adapted in such a way as to obtain a Dice coefficient with a tolerance margin: TPs, FPs, and FNs have been calculated considering the tolerance margin. This loss function aimed at the aforementioned purpose.

Therefore, the Dice coefficient is defined as follows:

$$Dice_{tol} = \frac{2 \, |Y_{CL} \cap \hat{Y}_{CL}|_{tol}}{|Y_{CL}| + |\hat{Y}_{CL}|}$$

where $|Y_{CL}|$ (respectively $|\hat{Y}_{CL}|$) represents the number of pixels of the centerline (CL) of the nerve fibers in the True set Y (respectively predicted set $\hat{Y}$), and $|Y_{CL} \cap \hat{Y}_{CL}|_{tol}$ represents the common pixels between the two datasets calculated with the tolerance margin.

As in the previous case, the coefficient can be defined with an equivalent equation:

$$Dice_{tol} = \frac{2 \, \widetilde{TP}}{2\widetilde{TP} + \widetilde{FP} + \widetilde{FN}}$$

Where $\widetilde{TP}$, $\widetilde{FP}$, and $\widetilde{FN}$ indicate the corresponding indices calculated with tolerance margin.

In order to derive these indices, it is necessary to obtain the central line representing the region predicted by the analyzed network. Figure 3.8 shows an example of the network output processing necessary to obtain the prediction skel.

Numerous approaches for skel extraction have been proposed in the literature. However, these are non-differentiable methods, as they present discretization operations [140–142].

In order to take advantage of the Dice coefficient with tolerance, it is necessary that the thinning operations, necessary for obtaining the skel, must be differentiable. Thanks to the implementation of an iterative process based on morphological operations of dilation and erosion on grayscale images, it was possible to develop an
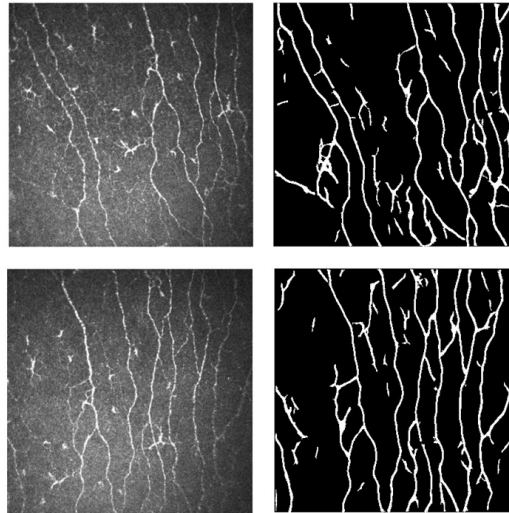
FIGURE 3.8: Example of an output of the network.

algorithm capable of extracting an approximate skeletonization from the final activation maps, maintaining a completely differentiable network. Some of the steps of the implemented process are shown in Figure 3.9.
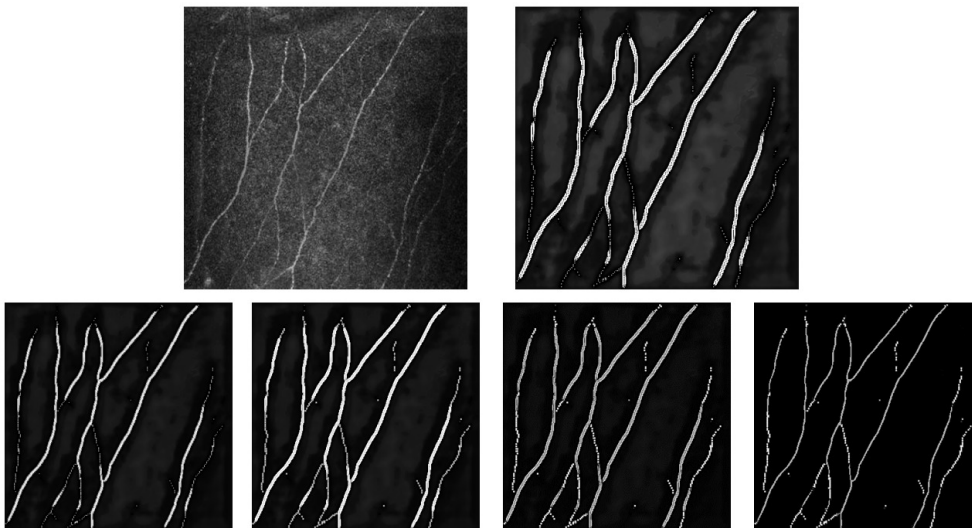
FIGURE 3.9: Up left: Original image, others are images that represent the subsequent steps necessary for obtaining the skeleton through differential operations.

As in the previous cases, also in this case the loss function is obtained starting from the coefficient just described as:

$$L_{Dice_{tol}} = 1 - Dice_{tol}$$

The function thus described allows for a consistent comparison between the central lines deriving from manual analysis and the automatic analysis. Generally, when evaluating the tracing quality of an algorithm, or even when comparing two manual

tracing, it is logical to take into account a margin of tolerance when dealing with a single pixel line that represents an extended region.

3.5.6 Dice Combination Loss

As highlighted in the pre-processing techniques, semantic segmentation involves the identification of all those pixels belonging to an object (be it the centerline or the entire nerve fiber). Wanting to emulate as much as possible the clinical process that involves tracing the skeleton after having recognized the pattern that identifies all the pixels belonging to the nerve fiber, it was decided to investigate the goodness of the networks even in the face of an extended region.

In this analysis, it would seem superfluous to use the loss function just presented (Dice with Tolerance loss, $L_{Dice_{tol}}$). However, as is evident in Figure 3.9 (but also in previous examples of IVCM images, especially in Figure 3.3, where all nerves are traced), the corneal nerve fibers present in the sub-basal plexus can have different thickness, with a large or narrow diameter.

It is important to keep this in mind when talking about coefficients such as Dice and Tversky. Indeed, the use of these indexes does not weigh the fibers of different thicknesses in the same way. Assuming that the nerve fibers are equal in length, fully recognizing a thicker nerve fiber will generate a greater coefficient value than recognizing the thinner fiber. This is because the pixels of the wide fiber are more in number than those of the thin fiber. However, in corneal nerve fiber tracing, it is important to correctly recognize as many fibers as possible.

To overcome this problem, the goodness of a new loss function obtained from the combination of two different losses was investigated; we combine the Dice Loss and the Dice with Tolerance loss presented above.

The two functions are related to each other simply by mediating their contribution:

$$L_{Dice_{comb}} = 0.5 L_{Dice} + 0.5 L_{Dice_{tol}}$$

The function thus obtained allows considering both the presence of the unbalanced classes (thanks to the Dice function) and the continuity of the nerve fibers (thanks to the Dice with tolerance function).

3.6 Experiments

Based on the architecture, loss function, and target images presented before, several experiments were carried out in order to analyze the different capabilities of the proposed algorithms to generate a semantic segmentation, as correct as possible, of the central line of the corneal nerve fibers.

Different models of convolutional neural network, different loss functions, and target images of different nature (skel and regions) were combined, and the different framework obtained were analyzed. The experiments results will be reported.

We distinguish the experiments conducted into two parts, based on the type of analysis required: in the first group, the experiments conducted on the central line of the nerve fibers will be presented and analyzed, while in the second group the experiments conducted taking into consideration the region that entirely describes the nerve fiber will be presented and analyzed.

3.6.1   Skel Analysis

Starting from the modules described in Chapter 3.3 (*Convolutional neural network - CNN*) and taking as a baseline the UNet described in the same chapter, the following convolutional neural architectures were investigated:

- UNet (the one used as baseline)

- UNet with attention modules (AM-UNet)

- UNet with residual connections and attention modules (AM-ResUnet)

- UNet with the ASPP module (ASPP-UNet)

- UNet with attention modules and the ASPP module (AM-ASPP-UNet)

The neural network algorithm was initially written in MATLAB (MATLAB 2020a, The MathWorks Inc., Natick, Massachusetts, United States). Afterward, to ensure better performance, in Python language (3.9.7) using keras API [143] with a Tensorflow 2.5.0 backend [144].

Using additional modules (residual connections, attention modules and ASPP modules) in a convolutional neural network inevitably causes an increase in the computational complexity of the model itself: in Figure 3.10 the total of the parameters describing each of the networks in analyses are reported. The total number of parameters is also distinguished from those that are actually trainable during the network training process.

Network extensions, by increasing the number of parameters, influence the time required to train the model.

From the graph in Figure 3.10, it is possible to quickly see that the greatest increase in parameters occurs with the introduction of the ASPP module: from the UNet used as a baseline, adding only the ASPP module involves an increase in the number of parameters of about 70%, while the introduction of the attention module involves an increase of less than 10%. However, the time required for prediction remains almost unchanged.

Despite the need, for more or less complex networks, of a number of different iterations to achieve good performance during training, it was decided to train all networks for a total of 60 epochs: a sufficient number of epochs for each network to reach a good convergence. Mini-batches of 32 elements were used, the Adam [145] was selected as optimization algorithm, with an initial learning rate of 0.001 and a reduction of half every 20 epochs.
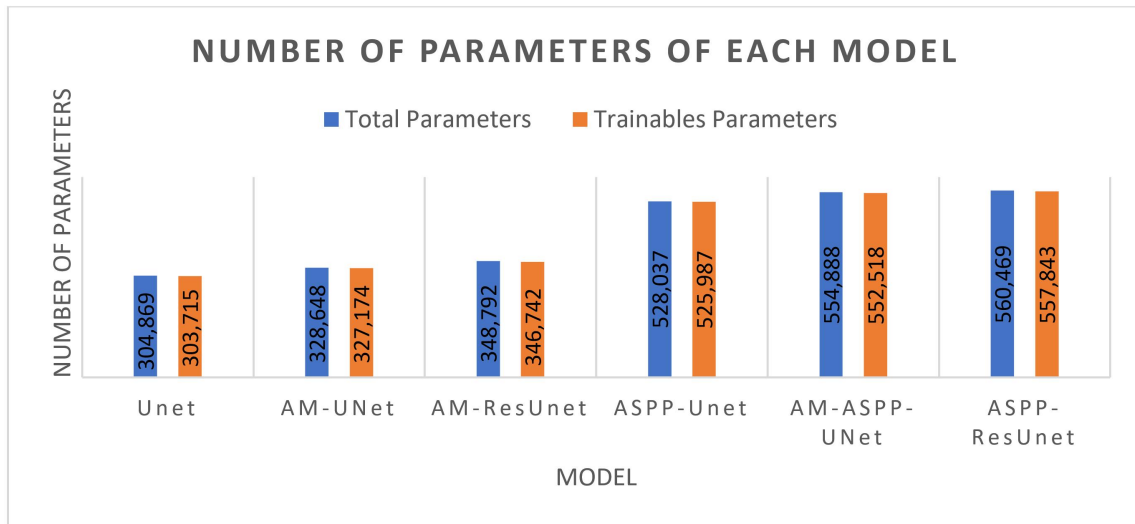
FIGURE 3.10: Number of parameters (total and trainable) for each model
tested.

The networks were trained using the loss functions presented above, with the
exception of the Dice Combination Loss (which we said is designed for pixel-wise
contexts and not just the centerline):

- Balanced Binary Cross-Entropy Loss

- Dice Loss

- Tversky Loss,

- Focal Tversky Loss

- Dice with Tolerance Loss

3.6.2 Pixel-wise Analysis

In the case of pixel-wise analysis, more attention was paid to the analysis of the pro-
posed loss function. In this case, in fact, only two network models were compared:

- Simple UNet (the one used as baseline, as in previous case)

- UNet with residual connections and Atrous-Spatial Pyramid Pooling module
  (Res-UNet with ASPP

The choice of these two extensions is related to their properties:

- The residual connections, as previously reported, provide an alternative path
  to the data to reach a certain part of the network: this alternative path is useful
  in the training phase.

- The Atrous-Spatial Pyramid Pooling (ASPP) module, thanks to the multi-scale approach performed through convolutions at different dilation rates, allows considering the continuity of the nerve fiber. This concept is even more important when analyzing fibers at the region level and not just at the centerline.

In Figure 3.10, the parameters (total and trainable) of the new proposed network are also shown: this is the network with greater number of parameters than the previous ones and, if compared to the basic UNet, an increase of more than 80% is reached. This increase, once again, translates into a longer time to converge. On an empirical basis, it was decided to bring the number of training periods to 200, with a mini-batch always of 32 elements and adopting Adam [150] as optimizer, with an initial learning rate of 0.001, with a reduction of half every 20 epochs.
In this case, only three loss functions were considered:

- Balanced Binary Cross-Entropy Loss

- Dice Loss

- Dice Combination Loss (expressly designed for this analysis)

3.7 Performance Evaluation - Results and Discussion

As at the beginning of the previous section, models were trained on 8909 images, which were labeled using the algorithm proposed by Guimarães et al. [95], and tested on 90 images analyzed manually.

The most common strategy for evaluating the results obtained by semantic segmentation algorithms is to consider segmentation as a pixel-level classification problem and evaluate it using a pixel-level confusion matrix. The first measure that is extracted from the matrix is the accuracy: in the case of unbalanced data (as in the case of corneal nerve fiber tracing), it is not the most effective index for an evaluation of the overall performance.

The Intersection-Over-Union (IoU) segmentation measure, also known as the Jaccard index, which counts the total number of incorrectly labeled pixels in the image, is now *de facto* standard.

Very similar to the Jaccard index is the Dice coefficient seen previously in the definition of the homonymous loss function: Jaccard and Dice are positively correlated, which means that if one sets out that model A is better than model B in segmenting an image, the other will set out the same.

In the case of corneal nerve segmentation, attention is paid to the centerline that identifies them. Therefore, the measures just mentioned are not optimal: the central line, in fact, may not correspond perfectly between different tracings, but this does not mean that it is incorrect. Manual annotation itself is hard and complex, so sometimes it can be inaccurate and not draw the perfectly centerline. For this reason, even when evaluating the algorithm, it is correct to take into account a tolerance margin.

Generally, for the evaluation of the identification and tracing of corneal nerve fibers, it is customary to take into account two indices:

- The True Positive Rate - TPR, (or recall) that corresponds to the proportion of nerves correctly identified by the proposed algorithm (the higher, the better) and which is calculated as:

$$\widetilde{TPR} = \frac{\widetilde{TP}}{\widetilde{TP} + \widetilde{FN}}$$

  [$\widetilde{TP}$: true positive; $\widetilde{FP}$: false positive; $\widetilde{TN}$: true negative; $\widetilde{FN}$: false negative. All are calculated considering a tolerance margin]

- The False Discovery Rate - FDR (or complementary of precision) which corresponds to the proportion of nerves mistakenly identified as such (the lower, the better), calculated as:

$$\widetilde{FDR} = \frac{\widetilde{FP}}{\widetilde{TP} + \widetilde{FP}}$$

  [$\widetilde{TP}$: true positive; $\widetilde{FP}$: false positive; $\widetilde{TN}$: true negative; $\widetilde{FN}$: false negative. All are calculated considering a tolerance margin]

Both indices were calculated taking into consideration a tolerance margin of 3 pixels (i.e., a pixel, classified by the algorithm as a nerve, will be considered a TP if it is found within an area of 3 pixels thick with respect to the reference nerve).

The best result would be a TPR index as close to 1 as possible and an FDR index as close to 0 as possible. It is not easy to assess whether the simultaneous variation of TPR and FDR leads to a better result, for this reason, an additional performance evaluation index was extrapolated. Starting from the two above-mentioned indices, a Global index was generated based on the Dice formula. It is defined as:

$$GlobalScore \ = \ 2\frac{\widetilde{TPR} * (1 - \widetilde{FDR})}{\widetilde{TPR} + (1 - \widetilde{FDR})}$$

This index tends to 1 if $(\widetilde{TPR})$ is 1 and $(\widetilde{FDR})$ is zero (case of perfect correspondence between manual and automatic analysis); it gradually decreases with the decrease of $(\widetilde{TPR})$ and the increase of $(\widetilde{FDR})$. The value of 0 is obtained in the case in which manual and automatic analysis are complementary.

3.7.1 Skel Analysis

Before being able to calculate the indices just presented, a single post processing step was carried out: therefore, the network output was subjected to skeletonization. This step has proved to be fundamental in order to calculate the indices presented above and analyze the performance of the individual networks: all the networks developed,

in fact, did not produce the only central line in output, but instead created a thicker region. An example is reported in Figure 3.11.
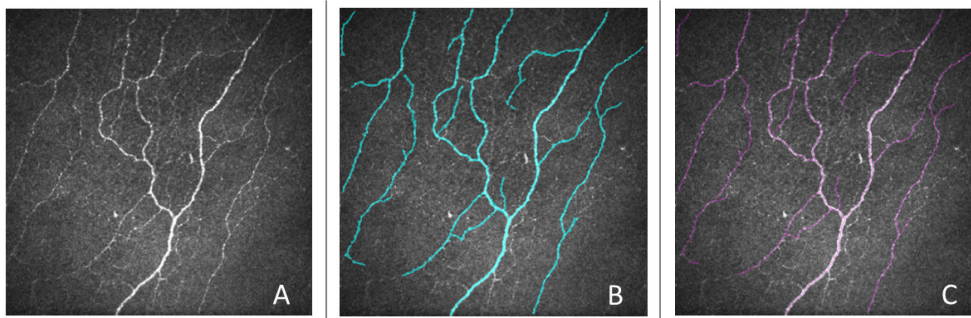
FIGURE 3.11: Representative image of the skeletonization process. (A) Original image; (B) example of an output of the network; (C) results of skeletonization.

Table 3.1 and Table 3.2 show the TPR and FDR indices, respectively. These are the indices obtained at the end of the training of the 5 proposed models, trained according to the 5 different loss functions under examination.

Considering the simple UNet, trained with Balanced Binary Cross-Entropy loss, as a baseline for comparison, it is possible to analyze how the performances improve (or worsen) both by modifying the structure (adding different connections and/or modules), and by using different loss functions.

TABLE 3.1: TPR score obtained from the evaluation of the several models examined

	BBCE	DL	TL	FTL	Proposed
UNet	85,61%	81,89%	74,22%	76,11%	85,62%
AM-UNet	87,64%	83,07%	75,56%	74,50%	86,19%
AM-ResUNet	88,33%	78,79%	76,03%	82,07%	88,65%
ASPP-UNet	85,04%	76,85%	86,74%	79,45%	84,86%
AM-ASPP-UNet	89,13%	81,46%	86,71%	84,23%	89,89%

Note: **BBCE**: Balanced Binary Cross-Entropy, **DL**: Dice Loss, **TL**: Tversky Loss, **FT**: Focal Tversky Loss, **Proposed**: Dice with tolerance loss. **UNet**: baseline, **AM-Unet**: UNet with Attention Modules, **AM-ResUNet**: UNet with Attention Modules and Residual connections, **ASPP-UNet**: UNet with Atrous-Spatial Pyramid Pooling module, **AM-ASPP-UNet**: UNet with Attention Modules and Atrous-Spatial Pyramid Pooling module.

Paying attention to the first column of both tables, it is important to observe that the variation of the architecture, through the introduction of a single module or combinations of them, leads to an improvement in the evaluation indices. Only in the case of ASPP-UNet the TPR decrease, but it is important to observe the significant

TABLE 3.2: FDR score obtained from the evaluation of the several models examined

	BBCE	*DL*	*TL*	*FTL*	*Proposed*
UNet	12,57%	8,32%	0,94%	1,39%	6,27%
AM-UNet	11,91%	9,85%	1,25%	1,06%	8,91%
AM-ResUNet	8,33%	2,10%	2,38%	3,19%	7,98%
ASPP-UNet	7,37%	1,27%	4,94%	2,87%	6,22%
AM-ASPP-UNet	8,68%	3,99%	3,85%	4,80%	4,87%

Note: **BBCE**: Balanced Binary Cross-Entropy, **DL**: Dice Loss, **TL**: Tversky Loss, **FT**: Focal Tversky Loss, **Proposed**: Dice with tolerance loss. **UNet**: baseline, **AM-Unet**: UNet with Attention Modules, **AM-ResUNet**: UNet with Attention Modules and Residual connections, **ASPP-UNet**: UNet with Atrous-Spatial Pyramid Pooling module, **AM-ASPP-UNet**: UNet with Attention Modules and Atrous-Spatial Pyramid Pooling module.

decrease also in the FDR. Therefore, it could be concluded that a decrease of approximately 0.6% in the proportion of correctly identified nerves is an acceptable loss compared to a decrease of approximately 5% in the proportion of incorrectly identified nerves.

The evaluation of the differences related to the use of the different loss functions are more complex to extrapolate, since the improvements of one of the two indices often coincide with the worst of the other index.. As regards Dice, Tversky and Focal Tversky, we observe a sometimes noticeable decrease in TPR values: the simple UNet passes from a TPR of about 86% with the BBCE to values of almost 10 percentile points less with Tversky and Focal Tversky. A similar situation occurs in the UNet with Attention Modules and Residual connections, when considering the BBCE (88.33%) and the Dice (78.79%).

However, such a significant decrease in the TPR value is associated with a significant decrease in the FDR value, which underlines that the network, when tracing a nerve fiber, has a high probability of tracing it correctly.

It is interesting to observe the values relating to the proposed loss function (Dice with Tolerance Loss): the TPR values obtained are very similar to the values obtained with the Balanced Binary Cross-Entropy. The variation in terms of TPR is less than 1% for all architectures, with a slight decrease in the case of AM-UNet and ASPP-UNet and a slight increase in the other three architectures.

Furthermore, as regards the FDR index, the proposed loss function always presents an improvement compared to the Balanced Binary Cross-Entropy: in some cases, it is a decrease of 1% or less, while in others the decrease is significant (up to over 6% in the case of the simple UNet).

For a complete and more accurate assessment, the values of the global index presented above were obtained. The results are reported in Table 3.3.

Going over again the analysis made previously, we immediately observe that the

TABLE 3.3: Dice with tolerance score obtained from the evaluation of the various models examined.

	BBCE	DL	TL	FTL	Proposed
UNet	86,51%	86,50%	84,86%	85,91%	89,49%
AM-UNet	87,86%	86,46%	85,61%	84,99%	88,57%
AM-ResUNet	89,97%	87,31%	85,49%	88,83%	90,30%
ASPP-UNet	88,67%	86,43%	90,71%	87,40%	89,09%
AM-ASPP-UNet	90,21%	88,14%	91,19%	89,38%	92,44%

Note: **BBCE**: Balanced Binary Cross-Entropy, **DL**: Dice Loss, **TL**: Tversky Loss, **FT**: Focal Tversky Loss, **Proposed**: Dice with tolerance loss. **UNet**: baseline, **AM-Unet**: UNet with Attention Modules, **AM-ResUNet**: UNet with Attention Modules and Residual connections, **ASPP-UNet**: UNet with Atrous-Spatial Pyramid Pooling module, **AM-ASPP-UNet**: UNet with Attention Modules and Atrous-Spatial Pyramid Pooling module.

inclusion of one or more modules improves the overall performance of the architectures under analysis. Observing the first column of Table 3.3, indeed, it is possible to see how the lowest value is attributed to the simple UNet, while there is an improvement, albeit slight (worst case of about 1.3%), in all other architectures. Even the network with only the ASPP module appears to have a global index value higher than the UNet: therefore, the previously observed decrease in the TPR is more than offset by the simultaneous reduction in the FDR.

Instead, as regards the different loss functions analyzed, considering the same architecture, it can be observed that in most cases the Balanced Binary Cross-Entropy Loss performs better than Dice Loss, Tversky Loss and Focal Tversky Loss. These are very slight differences in most cases. It is interesting to note that only in the architectures with ASPP module, the networks trained with Tversky loss have produced better results than the Balanced Binary Cross-Entropy Loss.

From the analysis of the last column, showing the values of the global index obtained after the training through the proposed loss function, it is possible to observe an improvement, especially in the case of the simple UNet architecture and in that of the UNet with attention module and ASPP module. This is, respectively, an improvement of 2.98% and 2.23%. Observing the tables showing the TPR and FDR indices, it can be seen that the increase in the global index is purely due to a decrease in the FDR values, since the TPR values remain almost unchanged.

To further analyze the results obtained and to make a further comparison between analyzed models and losses, boxplots were created. These graphs allow us to observe the variability of the indices between individual images: therefore, they give us an idea of how the network behaves in the test dataset and not just its average value (shown in the previous tables). The boxplots are shown in Figure 3.12 and Figure 3.13.

Each subplot of the figures represents the data related to a specific architecture. Therefore, for each architecture, the comparison between the tested loss functions becomes immediate.
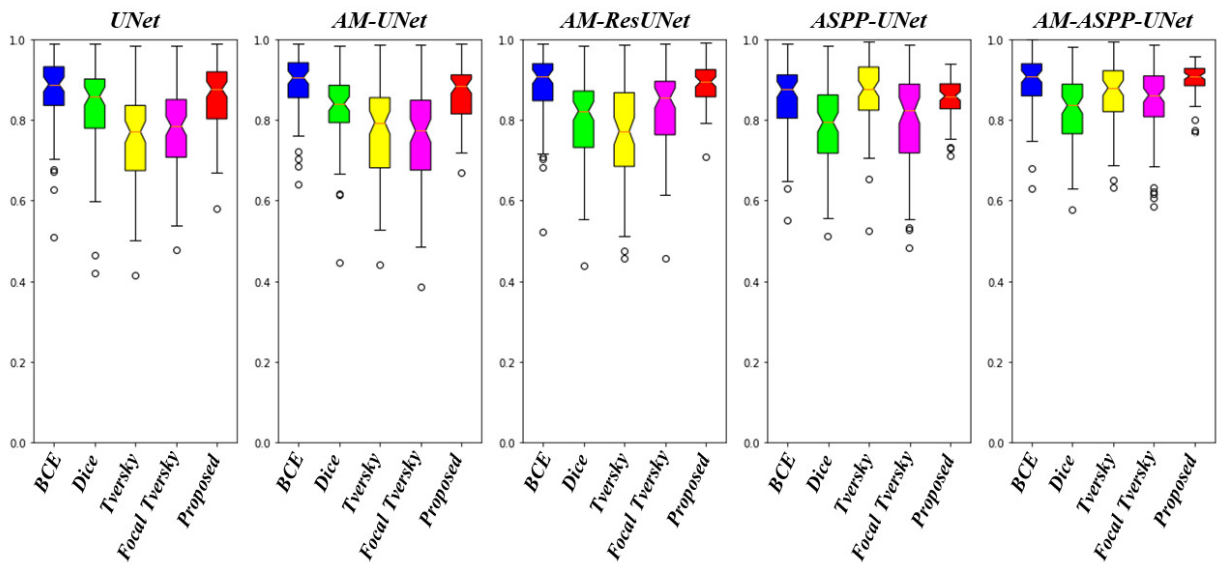
FIGURE 3.12: Boxplot comparison of models' performance in terms of TPR. Each box shows the score of a different architecture, comparing the different loss functions under examination.
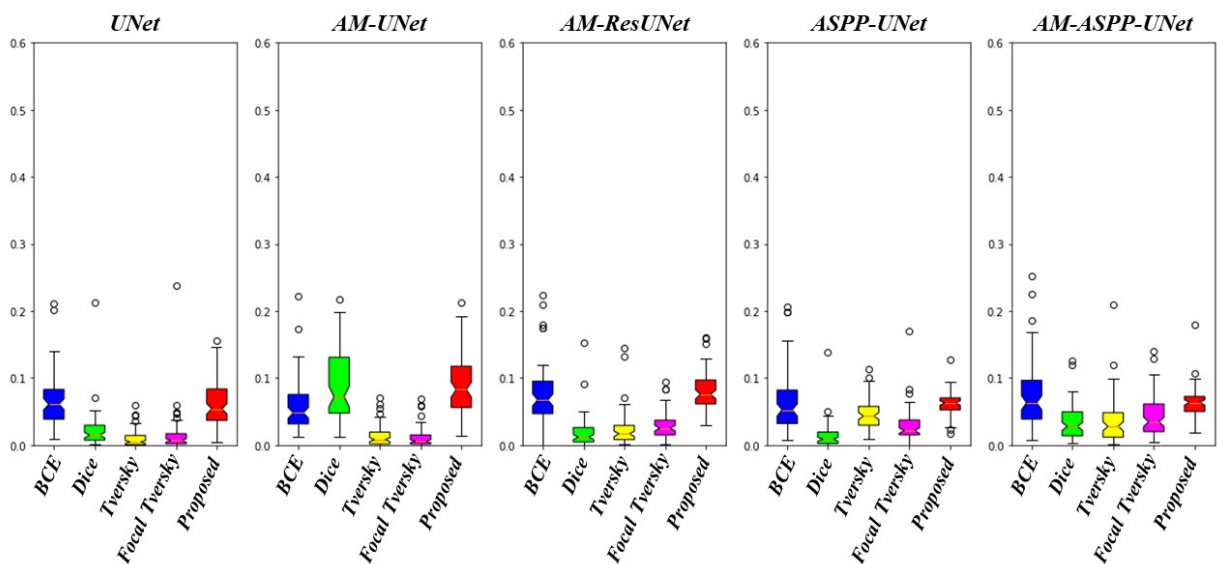
FIGURE 3.13: Boxplot comparison of models' performance in terms of FDR. Each box shows the score of a different architecture, comparing the different loss functions under examination.

It is interesting to note how the variability in TPR (Figure 3.12) of the Tversky Loss (yellow boxplots of each box) is high in the first three cases, while it decreases in the last two networks. Thus, in the architectures presented the ASPP module, not only the Tversky Loss has a better global score than the Balanced Binary Cross-Entropy Loss, but also reduces the variability in terms of TPR values of the single images.

Looking at the boxplots relating to the proposed loss function (red boxplots of each box), a reduced variability can be observed with respect to the other loss functions analyzed. It is also interesting to note that the TPR values of individual images never drop below 60%, while in other cases they even reach 40%.

With regard to Figure 3.13, showing the data relating to the FDR index, the great variability of the index in the case of the Dice loss function in the AM-UNet is immediately evident. This boxplot could highlight a problem that occurred during the train, linked, for example, to a number of epochs too small to reach convergence. The network was subsequently trained for another 10 epochs: the loss function values stabilized and the FDR and TPR indices were better on average and with a lower variability. Results were not reported in the tables because we wanted an analysis and a comparison between architectures and loss functions, without the variation of other parameters, such as, for example, the number of epochs of trains.

From the graphs relating to the FDR, it is also clear that, in the case of training through loss of Tversky and loss of Focal Tversky, there is a reduced variability and, as already mentioned by observing the tables, a rather low average value. These results are related to the choice of the values of α β and, for the FT, γ; they made it possible to the pay more attention to FPs, trying to reduce them as much as possible.

Observing the values related to the proposed loss, it can be seen that the inclusion of the ASPP module considerably reduces the variability of the index: the introduction of the multi-scale approach has probably allowed the network to discard from the result all those segments that were not connected and that, consequently, did not belong to a nerve fiber, thus reducing the FPs. Indeed, FDR reduction is linked to FPs reduction, and this is evident in more complex images. Where the nerve fibers are very thin and with a relatively low contrast, the UNet, considered as a baseline, struggles to give continuity in the segmentation. With the introduction of the ASPP module, better results are obtained: the pixels classified as FPs are reduced.

Figure 3.14 shows the results obtained through the baseline and the best analyzed models

3.7.2   Pixel-wise Analysis

Even in the case of pixel-wise analysis, before calculating the indices for performance evaluations, it was necessary to carry out the post-processing step. Since manual analysis involves tracing only the centerline of the nerve fiber, the comparison could not be made on the region representing the whole nerve. Therefore, the training was carried out in pixel-wise mode, while the test part was carried out on the centerlines: one drawn manually, the other obtained through a skeletonization process (as in the
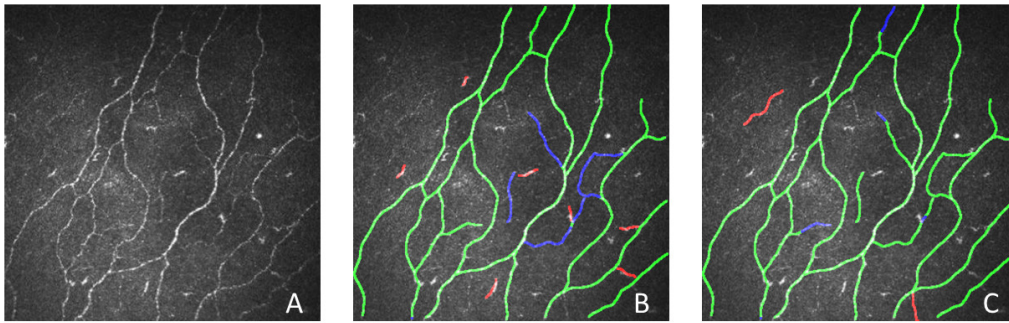
FIGURE 3.14: From left to right: (A) original corneal confocal images, (B) automatic tracing with baseline (Unet trained with binary cross-entropy loss function), and (C) automatic tracing with the best model (AM-ASPP-UNet trained with Dice with tolerance loss proposed). The green color represents the True Positive (TP), the blue color represents False Negative (FN), and the red color represents False Positive (FP).

previous analysis, starting from the regions identified by the convolutional neural network, the centerline was extracted).

All the indices obtained (TPR, FDR, and Global Score) are shown in Table 3.4.

TABLE 3.4: TPR, FDR, and Global Score obtained from the evaluation of the two architecture and three loss functions examined.

Architecture	Loss function	TPR	FDR	Global Score
UNet	BBCE	0,8751	0,0430	0,9142
Res-UNet with ASPP	BBCE	0,8989	0,0419	0,9275
UNet	DL	0,9098	0,0375	0,9354
Res-UNet with ASPP	DL	0,9080	0,0334	0,9363
UNet	Proposed	0,9196	0,0380	0,9403
Res-UNet with ASPP	Proposed	0,9275	0,0307	0,9479

Note: **BBCE**: Balanced Binary Cross-Entropy, **DL**: Dice Loss, **Proposed**: Dice with tolerance loss. **UNet**: baseline, **Res-UNet with ASPP**: UNet with residual connections and Atrous-Spatial Pyramid Pooling module.

The table shows that, taking the UNet as a baseline and comparing it with the architecture to which the residual connections and ASPP module have been added, there has been a slight improvement. Therefore, the introduction of the proposed modules has shown to improve, albeit slightly, the performance of the algorithm, reducing, in all cases analyzed, the FDR score, and, in most cases, increasing the TPR score.

As in the previous cases, also in this case it is difficult to decide whether a decrease in the TPR value is justified by a decrease in FDR. In the case of the Dice loss, it is therefore necessary to calculate the Global Score: from this value it is possible to say that the introduction of the new modules has benefited the performance in a very slight and superficial way. Overall, the GlobalScore score improved in all three cases

tested: however, these are very limited variations, the largest being about 1.33% in the case of the BBCE.

Furthermore, three different loss functions have been applied to each architecture: Balanced Binary Cross-Entropy loss, Dice loss, and the loss given by the combination of Dice (classical and with tolerance).

Comparing the first two, already present in the literature, it is possible to observe a first improvement from Cross-Entropy to Dice. This is probably related to the fact that Dice loss ignores the dominant class (in this case the background) and focuses on the nerve fibers, thus achieving better results.

At the same time, the proposed loss function balances the results of the Dice loss function with its version calculated on the center line and with the tolerance margins. In this way each nerve acquires the same importance in the tracing phase despite its thickness: it is known that it is important to identify the greatest number of nerves present in the images, in order to extract the parameters useful for diagnosis. The proposed loss function has further improved performance taking into account this concept and the continuity of the nerve fiber.
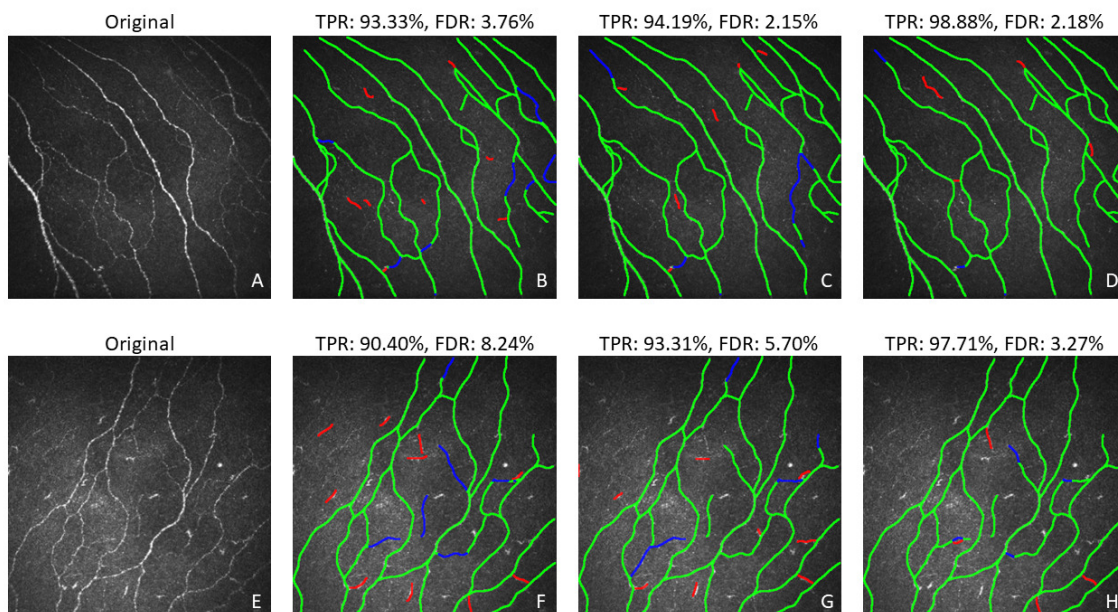
FIGURE 3.15: From left to right: original corneal confocal images (A, E), Binary Cross-Entropy results (B, F), Dice results (C, G), and proposed Dice-based results (D, H), respectively, for two representative images. In green correctly traced nerves (True Positive), in blue missing nerves (False Negative), and in red misclassified nerves (False Positive).

Figure 3.15 shows two examples of results obtained with Res-UNet with ASPP networks trained according to the different loss functions (the results of simple UNet are not reported, since the variation with respect to the proposed architecture is very limited, while the relevant difference is generated by the different losses).

Observing the figure (especially in the first example, images C and D), it is evident how the proposed loss function allows correctly identifying even the thinnest nerve fibers, which are missing (blue branch) in the results of the classical Dice. Furthermore, from the comparison between F and H, a decrease in the isolated segments can be noted: the proposed loss function, therefore, seems capable of maintaining only those branches that present a certain continuity.

For the choice of the number of epochs necessary for an accurate train, we have chosen to proceed empirically: a too small choice of the number of epochs would not have left the time for the networks to generalize the information correctly and, at the same time, a number of epochs too large would lead to possible overfitting. Therefore, it was decided to observe the trend of the graphs of the respective loss functions and at the same time to observe the trend of the metrics (TPR and FDR) during the training phase. From these observation, it was decided to bring the number of epochs to 200.

Figure 3.16 shows the trends of the evaluation indices, respectively, TPR and FDR, of the networks with UNet architecture, residual connections, and ASPP module. (The trends of the simple UNet are not reported as they are similar to those reported). From the graphs in the figure, it can be seen that, in terms of TPR, in the early epochs Binary Cross-Entropy and Dice perform better than the combined loss function (Dice Combination Loss). However, in the epochs after the 25th, a change in trend is observed, which leads the network trained according to Dice Combination Loss to have a more marked increase than the other two networks. Starting from about the 30th epoch, the TPR values are inverted; that is, the network trained with the proposed loss exceeds the other two. Observing this graph, therefore, allows understanding how the proposed loss function requires a longer period of time for convergence than the two known loss functions under consideration.
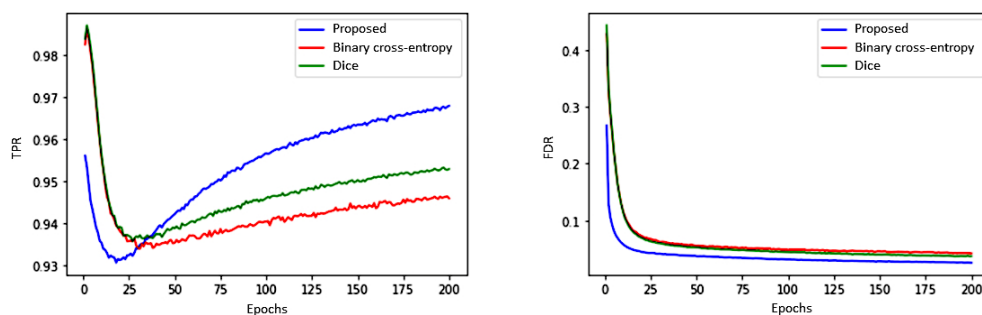
FIGURE 3.16: Metrics graphs at each epoch during the training phase of UNet with residual connections and ASPP module. On the left is the True Positive Rate (TPR, the higher the better) score, and on the right the False Discovery Rate (FDR, the lower the better) score.

Furthermore, if we had stopped the training of the network at 60 epochs (as in the previous case - Skel Analysis), we would have always obtained a higher TPR value and a lower FDR value for the proposed loss function, but the gap with the other networks would have been smaller. However, at 200 epochs we can see that the gap

between loss functions (both for TPR and FDR) has almost stabilized. However, it appears that the networks can still improve the results.

If one wanted to compare the two cases under examination (Skel and Pixel-Wise Analysis), considering the only difference given by the use of only skel or the entire region during the training phase, it would be necessary to reproduce the same conditions (i.e., same number of epochs and same architecture).

What can be seen from the tests carried out on the UNet, analyzed so far, is that an increase in the number of train epochs (from 60 to 200) and the transition from the central line to an extended region have allowed an increase in TPR values (from 85.61% to 87.51%) and a decrease in FDR values (from 12.57% to 4.30%). These variations also translate into a variation of the Global Score, which goes from a value of 86.51% to a value of 91.42%. Furthermore, if we once again focus on the trend of the TPR and FDR values obtained during pixel-wise training, we can observe that the FDR values after the 20th epoch are less than 10%. This data suggests that just the transition from centerline to region has a significant impact on the network's ability to reduce FPs and consequently reduce FDR values.

3.8   Conclusion

In-Vivo Confocal Microscopy is a technique that allows the acquisition of images of the corneal layers in a rapid and non-invasive way. Therefore, this technique becomes a fundamental tool for the direct observation, in the sub-basal plexus layer, of the nerve fibers present, which are closely related to the presence of ocular or systemic pathologies, as well as being important for studying postoperative inflammation.

It is important to emphasize that all clinical parameters (useful for the diagnostic process) depend on the identification and tracing of nerve fibers. For this reason, corneal nerve tracing is a very popular topic in scientific research.

In clinical practice, image analysis of the corneal sub-basal plexus is complicated: the manual tracing phase can be imprecise and subjective, in addition to the fact that it takes a long time.

For this reason, in recent years, attention has turned to the investigation of an automatic method that could overcome the limits dictated by manual analysis; but, as far as we know, there is still no universally accepted automatic technique for tracing.

Research in image processing has recently turned to deep learning techniques: these are techniques that have been able to provide encouraging results in all image processing tasks, whether they are classification, object detection, or semantic segmentation. In fact, with an adequate dataset and an adequate training process, it is possible to obtain excellent results.

In 2018 we began the investigation [98] aimed at verifying whether this technique could become the state-of-the-art also in the tracing of corneal nerve fibers. From the encouraging results of this first study, we wanted to investigate more in depth those

technique and pointed out what were the most suitable modifications and tools to obtain a fast, accurate and objective tracing.

First, the ability to improve tracing through changes in the architecture of the basic model (UNet) was analyzed. To do this, three different structures have been considered: residual connections, ASPP module (Atrous-Spatial Pyramid Pooling), and attention modules (AM). Starting from these structures, four different architectures have been created (AM-Unet: UNet with Attention Modules, AM-ResUNet: UNet with Attention Modules and Residual connections, ASPP-UNet: UNet with Atrous-Spatial Pyramid Pooling module, AM-ASPP- UNet: UNet with Attention Modules and Atrous-Spatial Pyramid Pooling module).

The introduction of the structures has brought about improvements in terms of Global Score, going from a score of 86.51% of the simple UNet, to a score of 90.21% in the case of the best model (AM-ASPP-UNet). Furthermore, it was possible to observe an improvement in the analyzed indexes (TPR and FDR) both in terms of mean and in terms of variance (the introduction of the ASPP module in particular reduced the variance within the test dataset).

In addition to architectural variation, the ability of different loss functions to improve the predictive results of the proposed architectures was then investigated. For this phase, some well-known loss functions in the literature have been considered: the Balanced Binary Cross-Entropy loss, the Dice Loss, the Tversky Loss, the Focal Tversky Loss. In addition, a loss function created *ad hoc* for nerve tracing has been defined and tested: it is an adaptation of the classic Dice loss that allows taking into account a margin of tolerance in comparison with manual analysis.

From the analysis of the Global Score, it is possible to note that the proposed loss function generated the best results in almost all the architectures under analysis: the TPR values remained high as in the case of the Balanced Binary Cross-Entropy loss, but the FDR values have significantly decreased.

From the standard analysis linked to the centerline of the nerve fiber alone, we then moved on to pixel-wise analysis. Starting from the skel previously used as ground truth in the train phase, a new ground truth was generated: this time each pixel of the image that belongs to the nerve fiber has been classified as such (not just the central line that identified it). Two networks were thus trained: a simple UNet (always used as a baseline for comparison) and a structure given by a UNet to which the residual connections and the ASPP module were added. Also in this case, as in the previous one, the change in structure has improved, albeit slightly, the results, bringing an increase in the Global Score.

Moreover, in this analysis we wanted to test the goodness of different losses: the Balanced Binary Cross-Entropy loss, the Dice Loss and a new loss proposed. This loss is given by the combination of the classic Dice loss and the Dice with tolerance analyzed previously. This combination allows taking into account both fundamental aspects in the tracing of nerve fibers: the presence of unbalanced classes (thanks to the Dice function) and the continuity of the nerve fibers (thanks to the Dice with tolerance function). From the analysis carried out, it is possible to deduce that, although the

proposed loss function requires more time to converge, it ultimately presents better scores for all the extracted indices: TPR, FDR and the Global Score obtained from them.

Furthermore, it seems that the introduction of pixel-wise analysis has also improved the results compared to the cases trained by using the centerline.

In conclusion, the identification and tracing of corneal nerve fibers is not a simple task: manually it is laborious, time-consuming, and subjective; while automatically it presents numerous obstacles to overcome. Thanks to deep learning techniques, fast and accurate tracing of nerve fibers seems to be increasingly possible. In this project, numerous structures and numerous loss functions have been investigated, which have led to promising results.

Chapter 4

Tortuosity estimation

The identification of nerve fibers in IVCM images of the sub-basal plexus is the first useful step for a subsequent more in-depth analysis. Tracing the nerves allows obtaining parameters of clinical interest. In this chapter we will not address all the clinical parameters present in the literature: many of them have a very precise definition and, therefore, their difference in the presented values in literature is linked only to the previous step of identification and tracing, or to instrument used to acquire the images.

The clinical indices, as seen in the *Diagnostic window* section (Section 2.3), are useful for the identification of normal or pathological corneal states: therefore, it is important to try to obtain the most correct and objective results. Clinical indices are useful for diagnosing the onset or presence of ocular/systemic pathologies, and for controlling inflammation and related healing processes, which are related to the use of devices (contact lenses) or to the undergoing surgery.

In general, it can be stated that the quantitative parameters of clinical interest most evaluated in the literature are the length of the nerve, the tortuosity of the nerve, the density of the nerve and the density of the bifurcations. Of these, the most discussed is the tortuosity that will be presented in this chapter and of which a framework for its estimation and use (more in depth in the following chapter) will be discussed.

The correlation between tortuosity of the corneal nerves and a large group of ocular and systemic diseases has already been demonstrated. However, there is no universally accepted definition of tortuosity. Consequently, the reproducibility of its measurement is poor, and it is not used in clinical practice. Furthermore, most of the recently proposed methods in literature derive a quantification of corneal nerve tortuosity from nerve tracing. This would require considering segmentation errors (especially if the tracing is done automatically), handling typical corneal nerve bifurcations, and combining individual segment values into image-level tortuosity.

In this chapter, after an in-depth analysis of the state-of-the-art in the tortuosity analysis (not strictly linked only to the corneal nerves, but also proposed for other structures), the analysis conducted for the classification into three levels of tortuosity (low, medium, high) of some confocal microscopy images is presented. All the fundamental aspects in the investigation for tortuousness values and all the solutions adopted to address the problems mentioned above will be presented.

In this chapter, the material published in the articles [146] will be discussed.

4.1 State of the art: tortuosity measures in literature

The tortuosity of the corneal nerve fibers is one of the most investigated parameters among those related to the nerve fibers of the corneal sub-basal plexus. Clinically, its importance has been demonstrated several times: numerous studies have shown strong correlations between the grading of tortuosity and the presence or progression of diseases such as dry eyes, keratoconus, and even diabetes [3, 147–150].

Currently, ophthalmologists mainly rely on a qualitative gross scale to estimate the degree of tortuosity of the corneal nerve, there is no automatic method (as for the identification and tracing seen previously) that allows obtaining an accurate and objective estimate.

In literature, there are many fields of application of a tortuosity measure: some related to the medical field, (such as the tortuosity of the retinal blood vessels [151], the tortuosity of the walking path of patients with Parkinson's and Alzheimer's [152, 153], the tortuosity of propagation in porous tissues [154], ...), others linked to other fields (such as geology, ecology, chemical-physical processes, the study of the propagation of acoustic waves ...) [155].

In each field of application, multiple aspects related to tortuosity have been taken into consideration in order to develop a framework capable of generating an accurate and automatic measurement of the parameter itself. However, there is no univocal definition of tortuosity: intuitively, it is said that when a trajectory has several turns or twists inside it, the curves in the trajectory are tortuous. However, it is often difficult to completely define the tortuosity without observing the event or phenomenon.

Regarding the tortuosity of corneal nerves, over the years, numerous definitions have been presented on which many attempts have been made to develop an accurate and automatic measure of tortuosity. Many of these studies exploited definitions already present in other fields of applications and, therefore, relied on metrics designed for other curvilinear structures (e.g., retinal blood vessels).

The tortuosity measures presented in the literature are very varied: it is important to distinguish those that can also be applied in the field of corneal nerves, in order to have measures that can be used in clinical practices. The tortuosity measures reported below are the most common and therefore most commonly used to estimate the tortuosity of the corneal nerve. They can be divided according to the approach on which they are based.

4.1.1 Methods based on geometric distances

These are the most common, given the simplicity of definition and easy implementation. Of the distance-based methods, the simplest and most widely used is the arc-to-chord ratio (AOC) [156]. Given the S curve (whose coordinates are highlighted by the pairs (x, y)), AOC refers to the ratio between the length of the curve (L_C) and the length of the chord (L_X), which is the distance between the two extremes of the curve and is defined as:

$$AOC = \frac{L_C(S)}{L_X(S)} - 1$$

where

$$L_C(S) = \sum_{i=1}^{n-1} \sqrt{(x_i - x_{i+1})^2 + (y_i - y_{i+1})^2}$$

$$L_X(S) = \sqrt{(x_n - x_1)^2 + (y_n - y_1)^2}$$

This estimate of the tortuosity gives a value for the comparison of the length of the curve with respect to the straight distance that joins the two end-points: when the curve is straight, the ratio is unitary and, after subtracting the term 1, the tortuosity index is null; this index increases as the curve is greater in length than the L_X segment.

A measurement of this kind has given good results when the S curves were small, while it struggles when it comes to larger segments. Furthermore, in a study of retinal vessels tortuosity [157], it has been shown that this measurement only gives an estimate of the deviation of the S curve from its chord, without considering how many turns or twists it performs.

Another measure based on distance, (prior to the previous one, but perhaps less simple in its description), is Relative length variation (RLV). This tortuosity measure provides for dividing the curve S into a series of single arcs with heights of the curves h_i and lengths of the chords l_i; once these values have been obtained, the tortuosity is given by the relative variation, the approximation of which is derived using a sinusoidal model of a segment of a blood vessel.

$$RLV = \frac{L_C(S)}{l} \approx \frac{8}{3} \sum_{i=1}^{n} \frac{h_i}{l_i}$$

A great limitation linked to this measure of tortuosity was the need for manual selection of the dividing points of vessels into single arches.

Also based on distance, in 2016 in [105] a measure of tortuosity, called Length Ratio (LR), was proposed.In that study, each nerve fiber was filtered according to the Savitzky-Golay filter, resulting in smooth curves, without high-frequency directional changes.

The measure of tortuosity is therefore calculated as:

$$RL = \frac{L}{L_{SG}}$$

With the length of the filtered curve L_{SG} calculated as

$$L_{SG} = \sum_{i=1}^{n} \sqrt{(\Delta x_i^{SG})^2 + (\Delta y_i^{SG})^2}$$

Where Δx_i^{SG}, respectively Δy_i^{SG}, represents the gradient between successive coordinates x_i^{SG}, respectively y_i^{SG}, of the filtered curve.

(In this case, the deviation of the curve from a smooth version of it is calculated, and not from its chord as in AOC).

4.1.2 Methods based on angles

These are methods for the estimation of tortuosity, which are concerned with quantifying the angular differences between consecutive vectors calculated in discrete steps from the curve, or which exploit the definition of the curvature. There are several implementations of this type of method, such as the tortuosity measure called Mean direction angle change (MDAC).

Proposed by Chandrinos et al. [158], it estimates the tortuosity by averaging the variation of the angle obtained in discrete steps. For each pixel P considered, two central segments are considered, one preceding the reference pixel, the other following it. Each segment is normalized (by dividing by the norm itself).

The MDAC metric is then calculated as the average of each point considered, where the dot product is obtained from the inverse of the cosine of the product of the two segments, as reported in the definition:

$$MDAC = \frac{1}{t_{length} - 2 * step} \sum_{n=step}^{t_{length-step}} arcocos(V_{-1} \bullet V_1)$$

where t_{length} stands for the particular track, V represents the unary vector (-1: before, 1: after the pixel P).

This measure of tortuosity is not reported when the number of segments is too small (e.g., ten or less), but in the case of sufficiently long curves, we have an idea of the variation of the tortuosity along the analyzed curve.

Very similar to the previous one is the definition of tortuosity proposed by Hart et al [151], and implemented as follows by Bullit et al [159]. Also in this case, the difference of angles between consecutive vectors, obtained by dividing the curve in discrete steps, is quantified. Always considering the pixel P_i as the subdivision point of the two vectors V_{-1} and V_1, respectively preceding and following the point P, the measure called Sum Of Angles Aetric (SOAM), is computed as:

$$SOAM = \sum_{i=2}^{n-1} arccos \frac{V_{-1,i} \bullet V_{1,i}}{||V_{-1,i}|| \bullet ||V_{1,i}||}$$

Always based on angles, there is the method proposed by Goh et al. [160]. This measure took into account the accumulation of changes in direction along the central line of the considered structure (in the case of the paper it was retinal vessels). A change of direction was considered if the angular difference between the angles, identifying two successive tangent lines, was greater than a fixed angle, in the case of retinal vessels, it was chosen 30°.

The measure, called Absolute Direction Angle Change (ADAC) was calculated as:

$$ADAC = \sum_{i=i+1}^{N-n} \theta(i) \geq \frac{\pi}{6}$$

Therefore, this formulation was strongly dependent on the selection of the points in which to calculate the tangent lines.

Bribiesca [161] also presented a work related to tortuosity: it is a measure based on the Slope Chain Code. Always based on the observation of angles, the proposed measure consists of discretising a continuous curve (obtaining straight line segments of constant length) and in calculating the slopes that change between contiguous segments.

This measure proved of be independent to translation, rotation, and scaling. These are important properties for the type of analysis we want to perform.

The Slope Chain Code tortuosity measure is defined as:

$$T_{SCC} = \sum_{i=1}^{n} |a_i|$$

where $|a_i|$ represents the slope changes between contiguous straightline segments scaled to a continuous range from -1 to +1.

4.1.3 Methods based on curvature

These are methods based on the common definition of curvature; in mathematics it indicates the amount by which a surface deviates from a straight line. These are measures strictly related to the previous ones, which were based on the variation of the angles.

There are a number of methods for estimating curvature. For example, given an S curve, represented by the centerline points ($S = [(x_1, y_1), (x_2, y_2), \ldots, (x_n, y_n)]$), K_i is the curvature at point i, which is estimated as

$$K_i = \frac{\Delta x_i \Delta^2 y_i - \Delta^2 x_i \Delta y_i}{(\Delta^2 x_i + \Delta^2 y_i)^{\frac{3}{2}}}$$

Starting from this definition, Smedby et al. [156] give a first calculation of the total tortuosity of the segment, in which the total curvature of the segment is calculated as:

$$tc(S) = \int_{t_0}^{t_1} |K_t| \, dt$$

Starting from this definition, many have been obtained, such as those proposed by Hart et al. [151] and reported in [162]:

- Total squared curvature:

$$tsc(S) = \int_{t_0}^{t_1} K_t^2 dt$$

- Total squared curvature normalized by the length of the blood vessels:

$$tsc_{L_c}(S) = tsc(S)/L_C(S)$$

- Total curvature normalized by the chord length of the blood vessels:

$$tsc_{L_x}(S) = tsc(S)/L_X(S)$$

These measures have zero measure for straight vessel segments and increasing positive measure for segments as they become tortuous.

As for an open curve, the absolute squared curvature (AC) is defined as:

$$AC = \sum_3^n |K_i^2|$$

Another method proposed in the literature for the calculation of tortuosity is the Mean Curvature (MC), this measure is proposed by Sinthanayothin et al. [163]. This method is based on the concept that each curve is represented by a succession of arcs of circumferences of different radius. Therefore, after obtaining the radius for each segment of the curve (r_i), using the equation of the mean curvature, the mean tortuosity of the image is calculated as:

$$MC = avg \sum_{i=1}^n \frac{1}{r_i}$$

If the result of the calculation is close to 0, the image is considered to have a low tortuosity. while, if the result is close to 1, the image is considered to have high tortuosity.

The Tortuosity Coefficient (TC), proposed by Dougherty and Varro [164], can also be reported in this group. This approach is based on second differences in the coordinates of the vessel midline: the distance δ_i represents the difference between the gradients of two successive segments. The tortuosity coefficient is defined as the sum of the absolute values of these distances divided by the sampling interval (P):

$$TC = \sum_{i=1}^n |\delta_i| \ / P$$

4.1.4   Methods based on twist estimation

Some methods rely on torsion estimation, where the focus is on the number of twists or inflections of the curve. This group includes the tortuosity measure proposed by

Smedby et al. [156] and subsequently improved by Bullitt et al. [159].

It is a measure that provides for the counting of the inflection points. Once this number is obtained, 1 is added to it and the whole value multiplies the ratio between the length of the curve and the length of the segment that connects the end points of the curve (same ratio present in AOC). The measure, adapted to the 3D case by Bullitt et al. [159], is called Inflection Count Metric (ICM) and is defined as:

$$ICM = (n_c + 1) \frac{L_C(S)}{L_X(S)}$$

Where n_c indicates the number of inflection points.

Grisan et al. [89] have also provided, and improved over the years, a twist-based metric of tortuosity: the tortuosity index (TI), in which the curve is divided into turn curves (segment between two different convexity changes), and the tortuosity was estimated by adding the deviations of each segment from the smooth curve. The tortuosity index is defined as follows:

$$TI_G = \frac{m-1}{m} \sum_1^m \left[\frac{L_{C_{si}}}{L_{X_{si}}} - 1 \right]$$

where m is the number of twists of the nerve fiber, $L_{C_{si}}$ is the length of the segment between two subsequent twists, and $L_{X_{si}}$ is the chord length between two subsequent twists. This measure of tortuosity was presented for the calculation of tortuosity of retinal vessels and was subsequently adapted for the use in the field of estimation of tortuosity of corneal nerves by Scarpa et al. [97].

The same name was used by Longmuir et al. [165] to indicate another tortuosity index: this measure evaluates the tortuosity by identifying the number of changes in curvature sign and is obtained as:

$$TI_L = \frac{(n+1) * [\sum_1^m [\theta_i]] * \sum_1^m [L_{C_i}/L_{X_i}]}{L_C * m * m}$$

Where n is the number of segments in a single vessel, m represent the angles of curvature θ_i, length of the respective area is denoted by L_C and the length of the chord is represented by L_x.

4.1.5 Other methods

This Group includes all those measures that do not belong to the categories seen above, but which are based on different aspects.

Among these is the tortuosity based on the thickness of the vessel wall (TW), presented by Azegrouz et al. [166] and later extended by Trucco et al. [157]. As can be guessed from the name of this measure, it combines the curvature with the

thickness and is defined as:

$$TW = \left(\sum_{i=3}^{n} \frac{\left|K_{B_1}(i)\right| + \left|K_{B_2}(i)\right|}{2} \right)^{\frac{1}{p}}$$

where K_{B_1} and K_{B_2} are, respectively, the boundary curvatures at the two boundary points associated with the i-th skeleton point.

Another method was proposed by Rodriguez et al. [167]. In this, the Fast Fourier transform of the vessel's curvature is used as an evaluating method for tortuosity. They computed the angle variations in three dimensions along the path of the vessel, they obtained an acute angle by looking at the tangent vectors, and divided those angles by the Euclidean distance D_i. Thus, the tortuosity (in rad / mm) was calculated as the sum of curvatures at each centroid obtained as described above.

$$FFT_T = \sum_{i=1}^{n} \frac{\theta_i}{D_i}$$

There are also methods that arise from the combination of the previous ones. Among these, the one proposed by Guimarães et al. [105] , which explores established and new tortuosity metrics for the analysis of nerve fiber tortuosity. This work is based on prior clinical investigation.

In Lagali et al. [168], the clinical perception of the tortuosity of the corneal nerves is hypothesized to have two different patterns. The latter are defined as short-renge (low amplitude and high frequency) or long-range (high amplitude and low frequency) directional changes. Thanks to this definition, the level of agreement between the different graders is increased, and therefore they wanted to emulate such a distinction also in the automatic grading.

In Guimarães et al. [105], starting from this definition of two distinct tortuosity (SRT, short-range tortuosity, and LRT, long-range tortuosity), they wanted to investigate which single metric or combination of metrics best traced the distinction performed manually. The investigation revealed that tortuosity is indeed a multifaceted problem to which a single mathematical definition cannot answer, but the combination of several aspects could solve it.

It is clear that all the measures mentioned above depend on the quality of the corneal nerve path: as repeated several times, the analysis and extraction of the characteristics of the corneal nerves are often dependent on the identification and tracing of nerve fibers. However, some investigations, such as the one proposed by Zhao et al. [169], have tried to overpass this problem and directly obtain an estimate of clinical parameters useful for diagnosis. Indeed, they proposed a framework to improve the quality of IVCM images and estimate exponential curvature without the need for nerve tracing.

Despite the many proposals present in the literature, it still seems that none of the proposed methods has achieved universal acceptance. This may be due to the fact that the description and definition of corneal nerve tortuosity is ambiguous and nonstandard [148, 168].

In addition to the lack of a precise definition of this important morphometric characteristic, a clinically useful estimate of tortuosity takes into greater consideration the most evident nerve fibers and the fibers with the greatest degree of complexity. This is because experienced ophthalmologists classify an image as highly tortuous if only a few nerves are long and twisted enough [104, 168].

It is important to underline that, in recent years, Chen et al. [170] introduced a new measurement in the fileld of nerves corneal parameters. It is not a measurement directly linked to tortuosity, but they investigated the capability of fractal dimension to identify diabetic patients with diabetic sensorimotor polyneuropathy. The fractal dimension is useful in measuring the spatial loss of nerve fibers, which may help to identify specific neurodegenerative conditions and augment the diagnosis of DSPN, like a tortuosity measure.

4.2 Materials

For the analysis and estimation of the level of tortuosity, images from a public dataset provided by Scarpa et al. [97] were used.

The dataset is composed of 30 confocal images of the sub-basal corneal nerve plexus from 30 different normal or pathological (diabetes, pseudoexfoliation syndrome, keratoconus) subjects.

As for the datasets used in the previous chapter, images were acquired using a Heidelberg Retina Tomograph (HRT-II) with the Rostock Cornea Module (Heidelberg Engineering GmbH, Heidelberg, Germany). Each image covered an area of 400×400 μm (384×384 pixels), representing a small part of the entire corneal sub-basal plexus. The images were saved in grayscale digital format. Image acquisition was performed at the Department of Ophthalmology, Ehime University School of Medicine, (Ehime, Japan), and each image was anonymized, eliminating any patient information. Each image was then manually classified as having low-, mid- or high-tortuosity. A representative image for each group is shown in Figure 4.1.

The acquisition of all the images used in this work was approved by the local ethical review committees: therefore, it took place with informed consent and according to the principles of the Declaration of Helsinki. Furthermore, no further specific ethical approval was required for the retrospective analysis of the resulting collection of images.

LOW   MID   HIGH
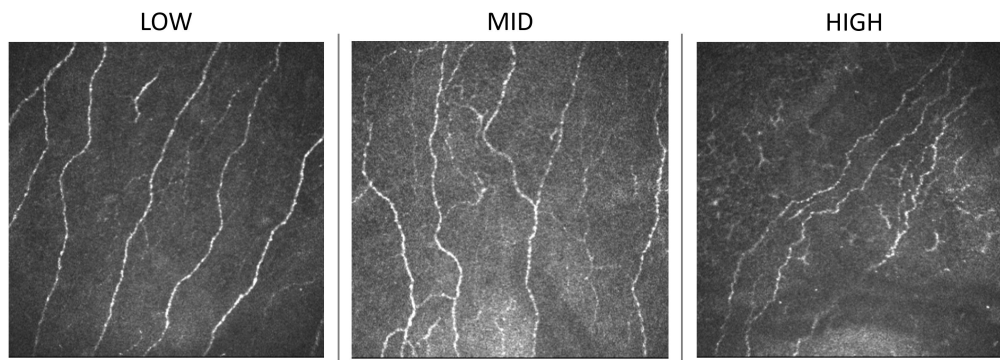
FIGURE 4.1: Representative images, one for every tortuosity group.
From left to right: low-, mid- or high tortuosity.

4.3 Pre-processing

For the estimation of tortuosity, it was decided to take into account metrics that are dependent to the tracing of the corneal nerve fibers. For this reason, the pre-procesing phase that is presented in this chapter is closely linked to the tracing phase necessary for estimating the tortuosity which is the fulcrum of the survey carried out.

As presented in the previous chapter, which focused on tracing corneal nerve fibers, a U-shaped convolutional neural network was also used in this case. The UNet used is the one whose results were presented in [171] and which provided reliable nerve tracing, with a sensitivity greater than 98% compared to manual analysis.

However, at the same time, the network also provided a high False Discovery Rate (higher than 13%). For this reason, a subsequent processing step was implemented to reduce the number of misidentified nerve fibers. This step was developed after careful observation of the errors generated by the use of the simple CNN: in most cases errors were linked to the presence of other corneal structures (e.g., dendritic cells) mistaken for nerve fibers. While, in other cases, some scattered or too short segments had been considered nerve fibers.

Generally, it has been noted that the tracing errors in the image, in most cases, corresponded to structures that appear as bright dots or small bright line-like objects. Thus, the post-processing step examines all traced segments and removes those with length and width comparable to those of these corneal structures. A False Discovery Rate lower than 5% was achieved.

Once the most accurate tracing possible has been obtained, in order to derive the required tortuosity metrics, it is necessary to manage the bifurcations: observing the tortuosity measures presented in literature and reported in the previous paragraph 4.1 (*State of the art: tortuosity measures in literature*), they are based on the coordinates of a continuous curve that has no bifurcations. Therefore, in order to evaluate the selected tortuosity measures (which will be presented in the next paragraph) the algorithm must be able to manage all bifurcations and branches that characterize the nerves in the corneal sub-basal plexus.

In this regard, an algorithm, capable of keeping a main path together and separating the branches, has been developed: thus, highlighting the fiber that will be defined later as '**main nerve fibers**' and separating what will be defined as '**secondary nerve fiber**'.

In the literature the problem of bifurcations was faced differently: the branches were used to be separated at each bifurcation, obtaining a lot of short segments. However, this solution does not seem optimal: separating all the branches at each bifurcation loses the continuity of the main fiber and, as experienced ophthalmologists classify an image as highly tortuous if only some nerves are sufficiently long and twisted, there is a risk of not having a fairly complete view of the length to be considered.

To carry out the separation, the developed framework plans to take into account a neighborhood for each bifurcation detected in the image. Through the use of morphological and thresholding operations, all pixels, belonging to the nervous branches in the neighborhood of the bifurcation under analysis, are highlighted: these pixels, separated from the background, will be part of the called 'branch region'.

To decide which branches to keep together (those that compose the main nerve) and which to separate (the ones that generate the secondary fibers), the following characteristics were extracted for each of the branches that reach the bifurcation under analysis:

- *Direction*, calculated as the angle formed by the branch itself and a horizontal line (range of 0° - 180°).

- *Thickness* of the fiber obtained from the average thickness of the corresponding branch region.

- *Brightness*, calculated as the average value of the pixel intensities of the branch region.

- *Length* of the fiber, as the length from the bifurcation to its termination.

Based on the extracted characteristics, rules were formulated for the choice of the continuity of the nerve fiber. The branches arriving at a bifurcation are compared two, by two and, to be considered as parts of a single nerve fiber, the two branches must:

- do not show sudden changes in direction near a bifurcation (similar directions suggest continuity between paths);

- have comparable thickness and, at the same time;

- have a comparable brightness.

In the event that several pairs of branches satisfy the rules just mentioned, the pair with the longest path will be selected and joined. An example of the result obtained through this framework is shown in Figure 4.2.
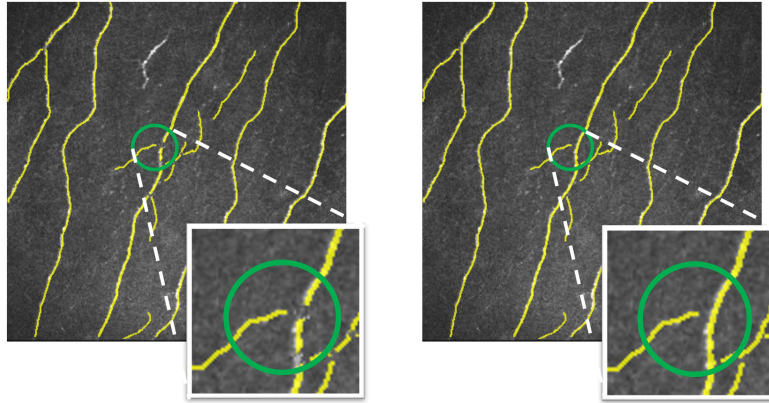
FIGURE 4.2: Examples of how the problem of bifurcations was faced. In the first case (left), as proposed in previous studies, the nerve fibers were split into different segments at every single branching. In the second case (right), the new approach devised: each branch was divided keeping the main path, which had the characteristics to be considered a continuous nerve fiber.

To verify the goodness of the new solution proposed in facing the bifurcation problem, masks were also obtained with the central lines of the nerve fibers traced and separated at each bifurcation (as it is usual to deal with the problem in the literature).

4.4 Nerve Tortuosity Metrics

The interpretation and consequently the quantification of tortuosity by clinicians varies widely: this is linked to the lack of a precise definition of this biomarker that mean that there is not universally accepted definition and formulation.

Taking into consideration some aspects highlighted in the introductory paragraph of this chapter, it was decided to investigate the ability to emulate a manual classification in three levels of tortuosity (low, mid, high), with the use of three different metrics. Two of the latter are metrics widely used in the literature and based on two different aspects: the absolute squared curvature (AC), based on the curvature, and the tortuosity index (TI), based on the twist estimation.

In the previous sections the absolute squared curvature (AC) was presented. It is defined as:

$$AC = \sum_{3}^{n} |K_i{}^2| \qquad with \qquad K_i = \frac{\Delta x_i \Delta^2 y_i - \Delta^2 x_i \Delta y_i}{(\Delta^2 x_i + \Delta^2 y_i)^{\frac{3}{2}}}$$

where given a nerve fiber segment (S), represented by the centerline points ($S = [(x_1, y_1), (x_2, y_2), \ldots, (x_n, y_n)]$), K_i is the curvature at point i.

Instead, the tortuosity index, also presented before, is computed as:

$$TI = \frac{m-1}{m} \sum_{1}^{m} \left[\frac{L_{C_{si}}}{L_{X_{si}}} - 1 \right]$$

where m is the number of twists of the nerve fiber, $L_{C_{si}}$ is the length of the segment between two subsequent twists, and $L_{X_{si}}$ is the chord length between two subsequent twists. Given its formulation, this index is also referred to as Tortuosity Density (TD).

In addition to being widely used and having provided important results in the estimation of tortuosity and in the identification of pathological states, among all the tortuosity measures, these two were chosen because they satisfy the following properties. Those properties are fundamental to define a tortuosity measure that corresponds to the evaluation made by an ophthalmologist.

Properties, as explained by Grisan et al. [89], provide for:

- independence by rigid transformations,

- modulation at constant amplitude and frequency,

- the tortuosity value of a nerve fiber must be in the middle of the values of the two single segments that compose it.

The third measure taken into consideration is the fractal dimension (FD). It is linked to the complexity of the shape and was calculated using the box-counting algorithm. Already used in the field of corneal nerve fiber imaging by Chen et al. [170] for the identification of a pathological state, however, it has never been analyzed as an index of tortuosity in the field of IVCM images of corneal nerves

The algorithm called "box-counting" consists of dividing the previously obtained image (the one depicting the central line of the identified nerve fiber and bounded by the ends of the same) into a grid of squares of equal size (side l) and, consequently, counting the number of squares, which contains a part of the central line of the nerve fiber under examination.

The procedure is repeated by varying the square size, from $l = 1$ to $l =$ the size of the entire image. By plotting the number of squares containing the nerve fiber against the corresponding size of the box (in a double logarithmic plot) and fitting the points using the least-squares method, we obtained a line whose slope indicated the value of the fractal dimension (FD).

As a consequence, the higher the value of the FD, the greater the complexity of the shape under analysis (in our case, the nerve fiber). The measurement of the fractal dimension also satisfies the properties listed above.

4.5 Measurement aggregation: from single nerve fiber to the whole image

The measures just presented provide us with values relative to a single curve. Thus, looking at the sub-basal nerve plexus images, the single curve would represent only a single nerve fiber (without bifurcations).

But, as is normal to do, the manual evaluation of tortuosity reported a single class for the whole image and not for every single nerve fiber present in it. Therefore, the final goal of the automatic analysis and estimation of the tortuosity of the corneal nerves would also be to provide an image-level parameter that is useful for the classification of the image under analysis.

To emulate the diagnostic process performed by experienced ophthalmologists, it is necessary to investigate and dwell on the choice of the best method of aggregation. That is, it is important to find that method which would allow obtaining a single tortuosity value for the entire image, obviously taking into account and combining the values associated with each of the nerve fibers.

Numerous methods have been presented in the literature to combine all individual nerve fiber tortuosity into a single image-level value. As reported in Guimarães et al. [105], most common and used are:

- the average value for all nerves,

- the maximum value for all nerves,

- the 75th percentile,

- the average value of the (at most) three longest nerves,

- the average value of all nerves whose length is within 157% of the longest nerve

These measures partly reflect the process performed by an experienced clinician. To be more precise, an experienced clinician classifies an image as high tortuous when all nerves have complex structures or, also, if only few nerves have a high complex structure, and it is long enough [104, 168]. Thus, to address both cases and emulate clinical practice as much as possible, the optimal level of length and the optimal number of twists were investigated. Therefore, these thresholds allow us to carefully select the nerve fibers to be considered in order to obtain a tortuosity value for the entire image.

Once the nerves to be taken into consideration for the estimation of tortuosity were identified and selected, the image-value of tortuosity was obtained by averaging the individual normalized values.

4.6 Performance Evaluation - Results and Discussion

For each of the 30 images available, the tortuosity indices (absolute curvature - AC, tortuosity density - TD, and fractal dimension - FD) were calculated as previously

TABLE 4.1: Classification errors and accuracy, considering each branch separated and considering the main and secondary nerve fibers. Classifications are performed using single indexes or combinations.

		Separated at each bifurcation		Main and secondary fibers	
		Number of classification errors	*Accuracy*	*Number of classification errors*	*Accuracy*
	AC	15	50.0%	15	50.0%
	FD	15	50.0%	12	60.0%
	TD	5	83.3%	5	83.3%
Metrics used	*AC & FD*	7	76.6%	6	80.0%
	FD & TD	4	86.6%	4	86.6%
	AC & TD	5	83.3%	6	80.0%
	AC, FD & TD	1	96.6%	1	96.6%

described. The values corresponding to each image were obtained according to the two different ways of dealing with the problem of bifurcations: both by dividing the branches at each bifurcation and by maintaining the main-secondary separation of the nerve fibers.

For both analyzed cases, it was decided to perform a linear discriminant analysis (LDA) in order to evaluate the ability of the tortuosity indices under analysis to classify the images available as images with low-, mid-, or high-tortuosity.

As explained above, before calculating the value of the entire image, the optimal level of corneal nerve length fibers and the minimum number of twists were investigated, to accurately select which of all nerve fibers would be taken under examination.

Linear discriminant analysis was applied to several cases: the ability to distinguish the three levels of tortuosity has been investigated both for the indices considered individually and for the indices considered in combination. All the results are reported in Table 4.1.

The worst results, as expected, were obtained by taking into account a single index at a time. The result improves when two indices are considered simultaneously, but the best result remains the one produced by the analysis with all three indices simultaneously. The best result and the separation plans obtained by LDA are reported in Figure 4.3.

From the table it is possible to observe that the classification results obtained by considering all the indices simultaneously and with the best nerve selection in both cases (considering all branches disjointed and considering the main-secondary fiber separation) show only one error classification over 30 images, thus providing an accuracy of 96,6%.

While in the analysis of only one or two indices at a time, the choice of the method for the management of bifurcations seems to affect the final result. When comparing the results obtained and reported in Table 4.1, it can be observed that in most cases
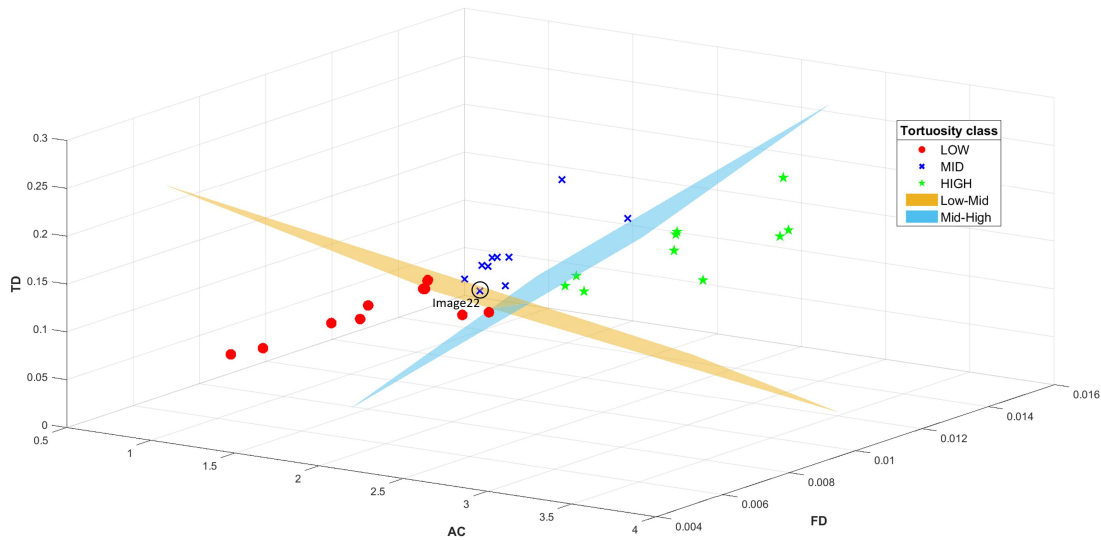
FIGURE 4.3: AC, TD, and FD values obtained for 30 images. Different symbols indicate the tortuosity class individuated manually: low (red dots), mid (blue crosses), and high tortuosity (green stars). LDA plane separators are reported as orange (low-mid separator) and blue (mid-high separator) surfaces. The classification error is highlighted by inserting the image ID (image 22).

the classification results, after taking into account the separation into main and secondary nerves, led to the same or better results than in the cases where the fibers nerves were separated at each bifurcation.

Later, in Chapter 5.1 (*Classification of healthy and diabetic with neuropathy subjects through tortuosity indices*), we will see how the choice of the method has proven important differences in the identification of healthy and pathological subjects.

A rank-sum test was performed to verify the ability of each method to correctly reproduce manual classification into the three groups. The p-values showed significant differences between all pairs of classes ($p < 0.05$). Thus, it was shown that there is a statistically significant difference between the pairs of the groups under examination: indeed, it means that the automatic tortuosity estimation proposed is able to distinguish the tortuosity in the three levels presented by the manual analysis.

4.7   Conclusion

In-vivo confocal microscopy allowed to acquire images of the corneal sub-basal layer, *in vivo*, in a rapid and non-invasive way. From the observation and analysis of the corneal nerves, it is possible to obtain multiple information of clinical interest: among many, one of the most discussed is tortuosity. This is a parameter that has been shown to be closely correlated with the onset and progression of some pathologies and with a continuous process of inflammation (sometimes linked to surgery). However, the

lack of accurate tracing step and of a precise definition of tortuosity, make the tortuosity analysis an open and unsolved issue: it appears that none of the so far proposed methods have gained universal acceptance.

During the Ph.D. project, after developing a framework for the fully automatic identification and tracing of corneal nerve fibers, the analysis of the tortuosity of the fibers themselves was the most thorough investigation taken into consideration. The developed algorithm, starting from the traced nerve fibers, tackles the problem of bifurcations by proposing a new method to keep the main nerve fiber together, and separate the secondary fibers.

For each of the nerve fibers thus highlighted (both main and secondary fibers), three measures of tortuosity were estimated, based on different aspects: absolute curvature (AC), based on the concept of curvature, tortuosity density (TD), based on the number of twists characterizing the branch, and fractal dimension (FD), based on the complexity of the shape.

Of all the nerve fibers present in an image, only those fibers that exceed the optimal length and complexity threshold were taken into consideration: this choice is related to the desire to emulate clinical practice. In fact, during the clinical process, experts in ophthalmology classify an image as highly tortuous if only some nerves are long and twisted enough.

Thus, once the optimal values of the length and twistness were investigated, the ability to distinguish three levels of tortuosity of each single metric and that of their possible combinations was analyzed through a linear discriminant analysis. An accuracy of 96.6% was achieved by using all three metrics simultaneously. This result shows that the algorithm fails to classify only one out of 30 images, considering all branches disjointed and considering the main-secondary fiber separation.

To the best of our knowledge, for the first time the separation between main and secondary nerve fibers was taken into consideration for the best estimation of tortuosity measures. The analysis of the results shows similar results in the case of the classification in low, mid, or high tortuosity: considering the nerves separated at each bifurcation or considering the distinction between main and secondary produces only one classification error, as highlighted above.

As highlighted in the results, this distinction has proven to be important when fewer than three indices are considered at a time and when we will use those indices in the healthy/pathological classification.

The results obtained are encouraging and can be a new starting point for the improvement of corneal nerve analysis: imitating the behavior of clinicians during the analysis (choosing the optimal values of the length and number of twists) and taking into consideration various aspects related to tortuosity allows to improve the results, in the classification of the level of tortuosity (low, mid, high).

4.8   Future works

The analysis of corneal tortuosity is still a undefined field of research: the description and definition of the tortuosity of the corneal nerve, and of a variety of other structures, are ambiguous and non-standard. Furthermore, the public datasets available are very limited and sometimes do not use the same classification metric.

The dataset used in this study proposes 30 images classified into three increasing levels of tortuosity (10 images for each class). The dataset proposed in Lagali et al. [168], presents 30 images, but in this case the images are ordered from the most tortuous to the least tortuous according to two different strategies, following a new definition of long-tortuosity and that of short-tortuosity.

In recent years, the Intelligent Medical Imaging Research Group (CNITECH, Cixi City, Ningbo City, Zhejiang Province) has proposed a new dataset related to the estimation of corneal tortuosity: in this case the images were analyzed by two different expert clinicians and the consensus between of them was used to define the classification of the images in 4 increasing levels of tortuosity. A total of 403 images were classified (level1: 54 images, level2: 212 images, level3: 108 images, level4: 29 images).

Therefore, the possibility of investigating whether there is a measure of tortuosity or a combination of them that can agree with the different datasets is iteresting. Thanks to the results will be probably possible to provide a completely automatic framework ro estimate tortuosity of nerve fibers. The final idea is to develop an algorithm that identifies and traces the nerve fibers automatically, and, starting from the tracing, is able to evaluate the tortuosity of the image and provide interesting parameters from a clinical point of view.

Chapter 5

Single, mosaic, and multiple-image analysis in clinical application

The investigations and studies presented so far have the ultimate aim of providing medical personnel with help in the processes of diagnosis, prognosis and monitoring of the health of the cornea and the whole human body in general.

There are many clinical situations in which corneal analysis helps, as seen in section 2.4 (*Automated sub-basal nerve plexus analysis*). Before the introduction of in-vivo confocal microscopy, the corneal nerves were analyzed ex-vivo, with the problem that they degenerate within the first 14 hours of death. Thanks to the introduction of IVCM, things have improved: there is the possibility for quantitative assessment in-vivo of corneal nerve properties (and other structures' properties) in normal health, disease, and postoperative conditions.

Thus, we can say that IVCM has brought numerous advantages: it is rapid, non-invasive and quantitative assessment of corneal nerve has demonstrated interobserver variability [2].

This chapter reports some investigations conducted on confocal microscopy images of the sub-basal nerve plexus. Based on the analyzes presented previously, some frameworks have been developed for the analysis of different pathological and inflammatory conditions, also taking into account the need for a larger visual field.

Indeed, one of the limits of IVCM is its field of view: each image acquired with this instrument allows us to analyze only a very small portion of the cornea at a time. As mentioned in Cruzat et al. [2], a single image covers only 0.15% of the entire corneal surface. Therefore, it is normal to assume that such a small region of the cornea, as represented in a single IVCM image, may not fully describe the general appearance of the corneal nerve and thus may not be sufficient to achieve a correct diagnosis.

In this chapter, the investigation begun with regard to dendritic cells is also introduced: as will be further explored, these cells are indicative of an inflammatory state and therefore can be of great interest for studying the onset and progression of some diseases or for studying the corneal healing status after surgery.

The different arguments explored will be presented separately taking into consideration multiple aspects: such as, the number of images or the type of combination, the pathology under examination and the structures analyzed. These studies were presented in the following papers [7, 8, 99, 146, 172].

5.1   Classification of healthy and diabetic with neuropathy subjects through tortuosity indices

Diabetic neuropathy is one of the most investigated systemic diseases through IVCM images. Among the many consequences associated with the presence of diabetes, there is neuropathy. It refers to damage to the nerve fibers: in particular, in diabetic patients, we can observe a reduction in corneal sensitivity, most of the time due to a loss of nerve fibers.

An increasing number of studies in the literature, trying to quantify diabetic neuropathy, have demonstrated a reduction in corneal sub-basal nerve fiber density. In addition to this decrease, an increase in the tortuosity of the fibers itself has been identified, often related to the stage and severity of neuropathy [173–177].

Therefore, we decided to investigate whether the proposed framework, developed to evaluate tortuosity level of IVCM images, could differentiate between healthy and pathological (with diabetic neuropathy) subjects, thus further investigating its clinical reliability and usefulness.

5.1.1   Material

A dataset consisting of 504 in-vivo confocal microscopy images was used. As in the previous datasets presented in this thesis, the images were acquired using the Heidelberg Retina Tomograph (HRT-II) with the Rostock Cornea Module (Heidelberg Engineering GmbH, Heidelberg, Germany), and each image was saved in a grayscale digital format and covered an area of $400 \times 400 \ \mu m$.

Image acquisition was performed at different clinical centers, and each image was anonymized to remove any patient information. The acquisition is approved by the respective local ethical review committees: it took place with informed consent and according to the principles of the Declaration of Helsinki, and for this investigation no further specific ethical approval was required.

The images were acquired from the central part of the cornea, however, without keeping track of the reciprocal position. The dataset was selected in a balanced way: 84 healthy subjects and 84 diabetics (type 1 or 2) patients with neuropathy were analyzed. For each of them, three different non-overlapping images were considered. For 112 subjects, images were acquired from the left or right eye only. For the other 56 subjects, the images were acquired separately from both eyes. In order to get the same number of images from each subject, we randomly selected the left or right eye for these 56 subjects.

5.1.2   Methods

As presented in the *Tortuosity estimation* chapter (Chapter 4), each image was analyzed using the fully automatic procedure proposed. Thanks to a U-shaped convolutional neural network, segmentation of the nerve fibers, present in the 504 images,

was obtained.

After reducing the number of nerve fibers wrongly identified through a specific processing step, the algorithm manages all bifurcations and branches. Also in this case, we investigated the ability of the two different methods: the first one, which maintains a united path (thus highlighting the fiber that are called "the main nerve fibers") and separates the branches (which we are called "secondary nerve fibers "); and the second one, which would divide all branches.

Once the tracing of each nerve fiber was obtained and the bifurcations had been separated according to both methods, the tortuosity measurements of each image were calculated. After selecting only those nerve fibers that respected the optimal level of length and number of twists (previously identified in the tortuosity study), the absolute curvature (AC), the tortuosity density (TD), and the fractal dimension (FD) were calculated for each nerve fiber. Subsequently, the entire image tortuosity metrics were obtained by averaging the individual normalized values.

5.1.3 Results

Considering both methods in facing bifurcation problems, a linear discriminant analysis (LDA) was performed to evaluate the ability of tortuosity indices to classify each image between images that belong to healthy and pathological subjects. The results, for the main-secondary fiber separation, are shown in Figure 5.1.
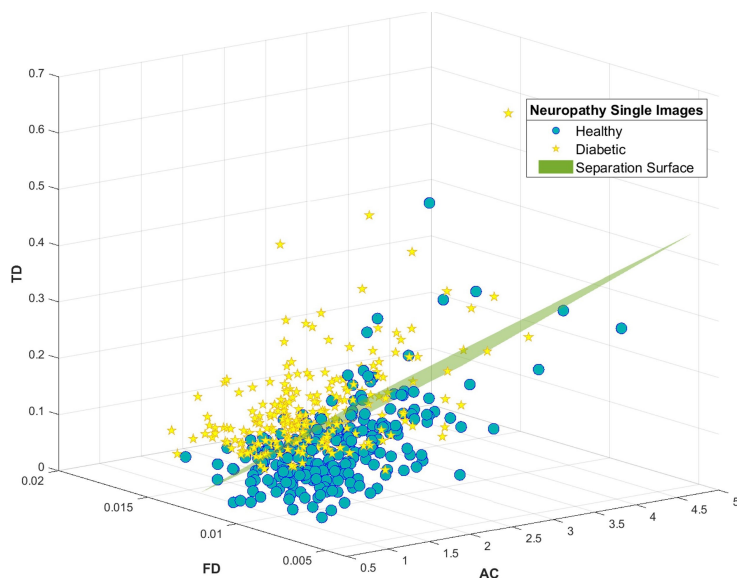
FIGURE 5.1: Values of AC, TD, and FD obtained for 504 images, half from healthy (blue dot) and half from pathological (yellow star) subjects. LDA plane separators are reported as green surfaces.

In the first row of Table 5.1, the number of classification errors and the relative accuracy are reported, both considering the two different methods to address bifurcation problems (main-secondary fiber separation and each bifurcation separation).

TABLE 5.1: Accuracy obtained through Linear Discriminant Analysis (LDA) conducted on single image analysis (504 images in total) and accuracy obtained aggregating 3 images for each subject (168 subjects in total).

	Separated at each bifurcation		Main and secondary fibers	
	Number of classification errors	Accuracy	Number of classification errors	Accuracy
Single image	182	63.89%	115	77.18%
Prevalent classification of 3 images	47	72.02%	28	83.33%
Median values of 3 images	38	77.38%	23	86.31%

As highlighted in the introduction, a single confocal microscopy image covers a limited area of the entire cornea. For this reason, it was decided to analyze three images for the same subject and investigate whether the simultaneous analysis of only three non-overlapping images of the same subject is sufficient to improve performance.

We analyze two different methods to obtain a single classification from three images. The first involves calculating the overall subject classification considering the prevalent classification of her/his images: a subject was considered properly classified if two or three images were correctly classified. Instead, the second method investigated whether the median value of the three images calculated for each of the three indices (median AC, median TD, and median FD) would improve the separation between healthy subjects and those with diabetes.

The results obtained for the two proposed methods are reported respectively in the second and third rows of Table 5.1, while the representation of the classification with median values is reported in Figure 5.2.

5.1.4   Discussion and Conclusion

Using the algorithm developed to distinguish between main and secondary fibers, and to estimate tortuosity as a combination of absolute curvature (AC), tortuosity density (TD), and fractal dimension (FD), we investigated whether the metrics obtained revealed differences between healthy and diabetic subjects.

If we consider the case in which the problem of bifurcations was addressed by separating all the branches, and in which each image was analyzed individually, the algorithm's ability to distinguish healthy and neuropathic subjects is poor. In this case, in fact, the accuracy is lower than 64%. By implementing a first modification and taking into consideration the method, proposed by us, to address the problem of bifurcations (that is, distinguishing the main nerve fibers from the secondary ones),
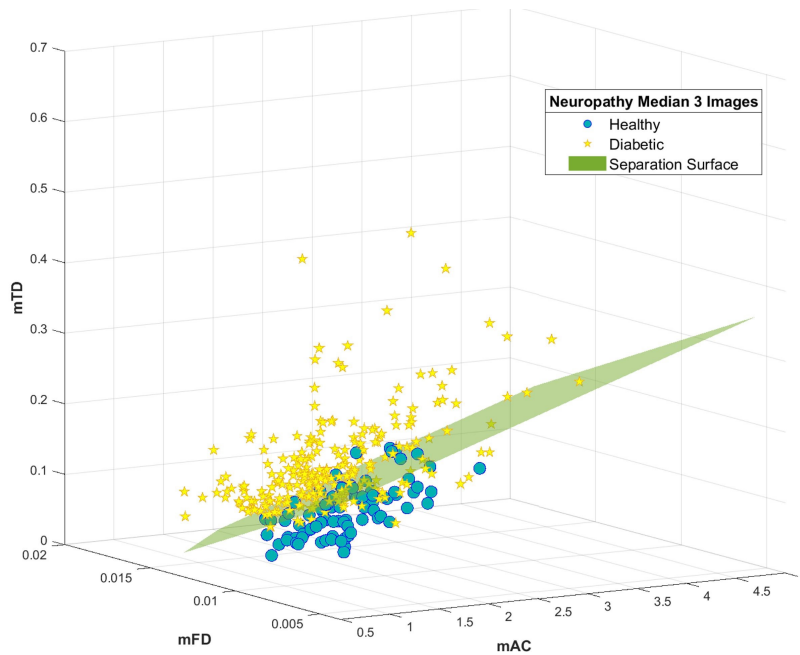
FIGURE 5.2: Values of median absolute curvature (mAC), median tortuosity density (mTD), and median fractal dimension (mFD) obtained from three images of each healthy (blue dot) and diabetic (yellow star) subject, considering the main and secondary fiber separation.

the result improves: the accuracy increases to just over 77%. This underlines the importance of taking into account the continuity of the nerve fiber.

Furthermore, by analyzing multiple images of the same subject at the same time, the information underlying the classification is increased. By choosing as final classification of a subject the prevailing classification of its images (that is, taking the classification of the individual images and obtaining the classification of the whole subject as that class that appears two or three times in the images), the result improves further: in the case of completely separated bifurcations the accuracy goes from 63.89% of the single images to 72.02% of the three images together; while in the case of the main-secondary fiber separation, the accuracy goes from 77.17% to 83.33%. Therefore, in both cases, considering three images at the same time allows improving the accuracy by about 5%, reducing the number of classification errors.

Taking into consideration the second method of aggregation of the values of the three images, by examining the median values, the classification result has improved even more. In the best case, which takes into account the continuity of the fibers, an accuracy of 86.31% is achieved, reducing the number of classification errors by 5 units, compared to the case of the prevailing classification.

In conclusion, a completely automatic framework was developed to distinguish between healthy and pathological with diabetes condition. From the results achieved, we can observe that the proposed framework produced interesting outcomes: emulating the behavior of the ophthalmologists during the analysis and taking into consideration various aspects related to tortuosity allowed us to distinguish the subjects under analysis sufficiently well.

Especially, considering the nerves separated at each bifurcation or considering the distinction between main and secondary fibers produced different results. The distinction of nerve fibers allows to reduce the number of incorrect classifications in all three cases analyzed: single image, prevalence of 3 images, median value of 3 images.

To the best of our knowledge, for the first time the separation between main and secondary nerve fibers was taken into consideration for the best estimate of the tortuosity measures and, consequently, for the distinction of the state of health of the patient.

5.2   Multiple-Image Deep Learning Analysis for Neuropathy Detection in Corneal Nerve Images

In the previous analysis, it was highlighted how the images of the corneal sub-basal plexus allow in a rapid and non-invasive way to obtain information on the patient's health status, identifying cases of diabetic patients with neuropathy and distinguishing them from healthy ones. The best result was obtained considering three images of the same subject and the median of the tortuosity indices.

There are many studies in the literature that deal with quantifying the corneal nerve parameter for the analysis of diabetic neuropathy. Many of them are based on manual tracing (a tedious, subjective, and time-consuming process), and only a few propose a fully automatic solution. Furthermore, many studies have shown the correlation of multiple morphological parameters with diabetic neuropathy, not just tortuosity.

In summary, the problems encountered during the analysis of the corneal nerves for diagnostic purposes are mainly three:

- each image covers only a small part of the cornea (0.15% of the entire corneal surface); thus, it is correct assuming that one single image may not fully describe the general corneal nerve appearance and consequently may not be sufficient to achieve a correct diagnosis.

- The extraction of parameters useful for diagnosis is based on the prior identification and tracing of corneal nerve fibers, which could present errors and be subjective.

- Identifying the features that best reveal the presence of the disease is not easy (some features are not sufficient if analyzed alone, others do not have a precise definition, ...).

To cope with the small size of the field of view problem, in previous sections we decided to use three images simultaneously, and the same principle will be used in this analysis.

Furthermore, in this work, the tracing and feature identifications problems are bypassed, and a method based on a convolutional neural network (CNN) is proposed to directly associate IVCM images to healthy subjects or to subjects with diabetic neuropathy.

5.2.1 Material

In this analysis, 600 in-vivo confocal microscopy images were considered. All images were acquired using the Heidelberg Retina Tomograph-II with the Rostock Cornea Module (Heidelberg Engineering GmbH, Heidelberg, Germany). Each image, saved in a gray-scale digital format, covers an area of $400400\mu m$ (384384 pixels), showing a small region of the corneal nerve structure.

As in the previous cases, the images were acquired in different clinical centers, in compliance with the rules established by the respective local ethical review committees. Therefore, the acquisition took place with informed consent and, also in this case, it followed the principles of the Declaration of Helsinki. The acquired images were anonymized to eliminate any patient information and no further specific ethical approval was required for the retrospective analysis of the resulting compilation of images.

The 600 images available belong to 50 diabetic (type 1 or 2) with neuropathy and 50 age-matched healthy subjects. For each subject, non-overlapping images were acquired, the left and right eye were considered separately. The images belong to the central area of the cornea and do not report any information regarding the reciprocal position.

5.2.2 Methods

The characteristic curvature of the cornea and the possible misalignment of the microscope with the corneal apex, during image acquisition, can generate some problems in the peripheral area of the acquired image (for example, poor illumination drift, spatial distortion, partial volume effect[1], and blurring).

To limit the influence of these distortions, a first pre-processing step of the acquired images was implemented: a crop of the most external area (10 pixels, empirically determined) was performed. In addition, the image has been resized by a factor of 0.7 through a bicubic function, favoring a partial noise resection. Therefore, the image subjected to these operations goes from a size of 384x384 pixels to one of 256x256 pixels.

Subsequently, in order to develop an algorithm based on deep-learning techniques, a rather large dataset is required. It was therefore decided to increase the size of the available dataset through a very common data augmentation technique:

---

[1]sometimes corneal structures belonging to layers adjacent to the sub-basal nerve plexus also appear in the image

the horizontal flip (consisting of flipping each image horizontally, obtaining the mirrored copy of each available image). With this operation, 1200 images are available, which can be divided into blocks of three images: each block will be composed of the three non-overlapping images of the same eye of a patient, and the blocks of the original images are kept separate from those of the images obtained through the flip operation.

When creating the blocks, it is also important to consider the order in which the three images are analyzed: 6 (i.e., 3!) blocks of 3 images each were built, and within them, the order of the images was rearranged.

This technique should ensure that the final classification is not influenced by the order in which the images of each subject are considered because, in this dataset, there is no information about their mutual position in the cornea.

In summary, with the operations just presented, 2400 blocks were obtained, each consisting of 3 non-overlapping images. 12 blocks (6 original and 6 flipped) are created for each of the left and right eyes of 100 subjects.

Figure 5.3 shows the blocks created for each subject and the proposed algorithm is schematized.
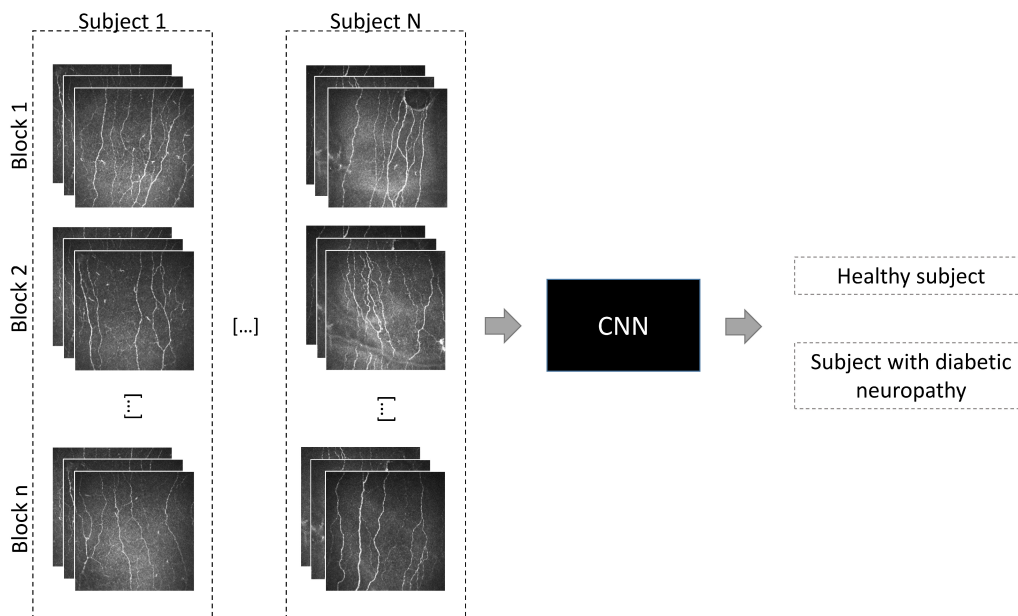
FIGURE 5.3: Diagram of the proposed algorithm. Input data correspond to N (=100) subjects, each composed by n (=24) blocks of 3 images. The algorithm uses the CNN to provide a binary classification (healthy/pathological).

From the diagram it is possible to see how, once the blocks have been obtained, they are used as input for a CNN whose goal is to classify each block of 3 images as healthy or pathological.

Figure 5.4 shows the architecture developed for this task: it is immediately clear that the CNN consists of two main parts, the first of features extraction (before the

fully connected layers) and the second of classification (composed of fully connected
and softmax layers).
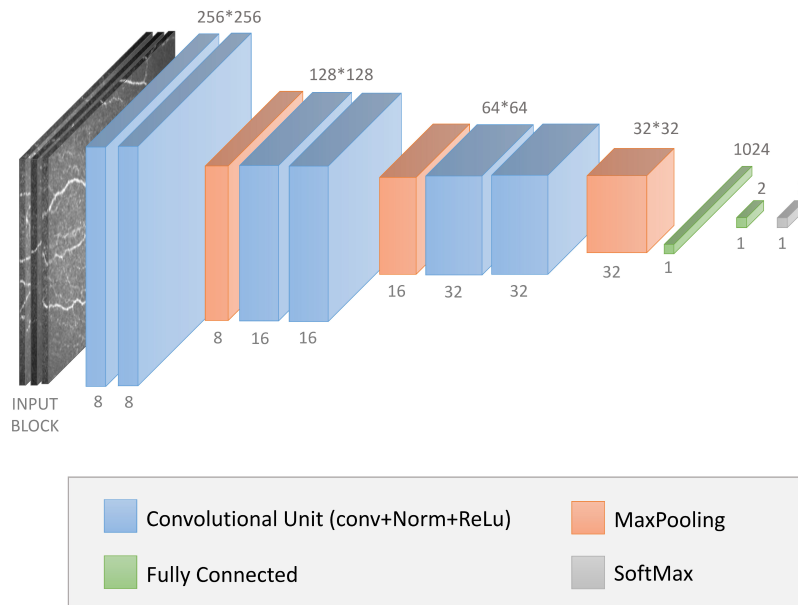
FIGURE 5.4: Convolutional neural network architecture for
healthy/pathological classification. Input is a block of 3 images.
Blue boxes correspond to a convolutional unit (which consists of a
convolutional layer, followed by a batch normalization and a ReLU acti-
vation layer). Orange boxes correspond to the activation maps obtained
by max-pooling. The 2 green boxes represent the fully connected layers,
and the gray one represents the softmax layer. The number of channels
(number of filters/kernels) is denoted at the bottom of each box. The
xy-size is provided at the top of each box.

The first part of the network is very similar to the UNet feature extraction path
seen in section 3.3.1 (*UNet as Baseline*): this branch is composed of a succession of con-
volutional units (composed of convolution, batch normalization, and rectified linear
unit - ReLU) and down-sampling layers (max-pool layer).
The first convolution unit is composed of 8 filters of $7x7$ size which allow detecting
low-level features. Moving through the network (in the direction of the information
flow), the input of the convolutional layers becomes smaller and smaller, due to the
presence of max-pool layers, while the number of channels (number of filters used)
increases.
In the deepest layer, the network is composed of 32 convolution filters of $3x3$ size,
each looking at different high-level features. The use of ReLU layers allows intro-
ducing a non-linearity in the network that allows the model to learn more complex
patterns.
The last step of the feature extraction part generates a tensor size $32x32x32$ which is
subsequently used as input for the classification part.

The latter consists of two fully connected layers, followed by a softmax layer which uses the softmax nonlinearity to normalize the result into a binominal distribution over the 2 classes, healthy and pathological subjects. This layer also provides a score that represents the confidence of the final classification.

For the training phase different hyper-parameters were tested, the best combination was selected: SGDM optimization with a momentum of 0.9 was adopted, training was performed on 10 epochs, batch size was set to 128, and initial learning rate was set to 0.0001. After training, the classification of a multiple-image block took less than 1 *ms*.

Since the dataset (despite the data augmentation) is not very large, to validate the goodness of the results, it was decided to implement the 5-fold cross-validation: training and evaluation were repeated 5 times, and each time, the CNN was trained on data from 80 subjects and evaluated on data from the other 20 subjects (10 healthy and 10 pathological each time).

This technique allows us to classify each available subject thanks to CNN, but each time the latter is trained on data that do not include the subjects (both left and right eyes and all flipped copies) under test.

5.2.3   Results

Using the 5-fold cross validation technique, results were obtained from 5 different test sets, each consisting of 20 subjects, half healthy and half pathological. For each eye of each subject, 12 blocks were considered, 6 data from the permutations of the image ordering, and another 6 obtained with the flipping operation. Each block was analyzed and classified using the proposed and trained CNN.

By analyzing each block with the respective trained network, the results highlight the good ability of the proposed algorithm to distinguish the blocks of healthy subjects from those of subjects with diabetic neuropathy. Taking into account all 2400 blocks, an average accuracy of 97% was achieved for each test group.

Then, the average sensitivity index was calculated, which indicates the percentage of pathological subjects correctly identified. Also the average specificity, which indicates the percentage of healthy subjects correctly identified, was calculated. In the case of individual blocks, the respective values are 98% and 96%. The results of the single blocks classification are reported in the first part of Table 5.2.

Also in this case, as in the case of the tortuosity discussed in the previous paragraph, for each subject we have more inputs available (in the case of the tortuosity we were referring to the 3 different images, in this case we refer to the 12 different blocks for each eye, obtained from permutation and flip operations). The final classification of the subject's eye was obtained considering the prevailing classification of the subject's blocks: it means that if 7 or more blocks are classified as pathological, then the classification of the eye will be pathological, while if 7 or more blocks are classified as healthy, then the classification of the eye will be healthy. Finally, a subject was considered properly classified if both right and left eyes were correctly classified.

TABLE 5.2: Performance achieved by the proposed CNN either on a single block of 3 images or on a single subject, using cross-validation on 100 subjects: training on 80 subjects and evaluation on the other 20, repeated for 5 times.

		mean	standard deviation
Single Block	Accuracy	97 %	2 %
	Sensitivity	98 %	3 %
	Specificity	96 %	6 %
Whole Subject	Accuracy	96 %	4 %
	Sensitivity	98 %	4 %
	Specificity	94 %	9 %

Following the reasoning just presented and averaging the results of the 5 test sets, the proposed CNN resulted in a mean accuracy of 96% (96/100 subjects were correctly classified). Also in this case, the sensitivity and specificity indices were evaluated, obtaining respectively 98% and 94%, as reported in the bottom part of Table 5.2.

Furthermore, the classification score was investigated for each available subject. This score defines the probability, for each subject, of belonging to the predicted class: when a high score is attributed to a subject, it means that the subject with an high probability belongs to the predicted class. The score can be interpreted as a percentage of how sure the algorithm is of the given classification. The score of each subject is derived from the average of the probability of all the blocks representing the subject itself.

The results are reported in Figure 5.5, keeping in evidence the separation between the 5 test sets. The average score was approximately 93%, as shown in Table 5.3. Incorrect and correct classifications were also considered separately with a mean score of 94% for the correct ones and 74% for the incorrect being obtained.

TABLE 5.3: Classification scores: mean of all data, standard deviation (sd), minimum (min) and maximum (max) values, mean of correct classification (meanCC), mean of wrong classification (meanWC)

mean	sd	min	max	meanCC	MeanWC
93%	9%	59%	100%	94%	74%

The proposed framework was also compared with a previously developed state-of-the-art method. The method proposed by Guimarães et al. [105] which analyzed the density and morphology of the nerve fibers of each image, considered individually. The tracing of the fibers occurred automatically [95], and density and tortuosity were calculated accordingly.

Tortuosity, following a clinic suggestion, was expressed by two indices: long-range and short-range tortuosity. Also in this case, starting from the indices obtained
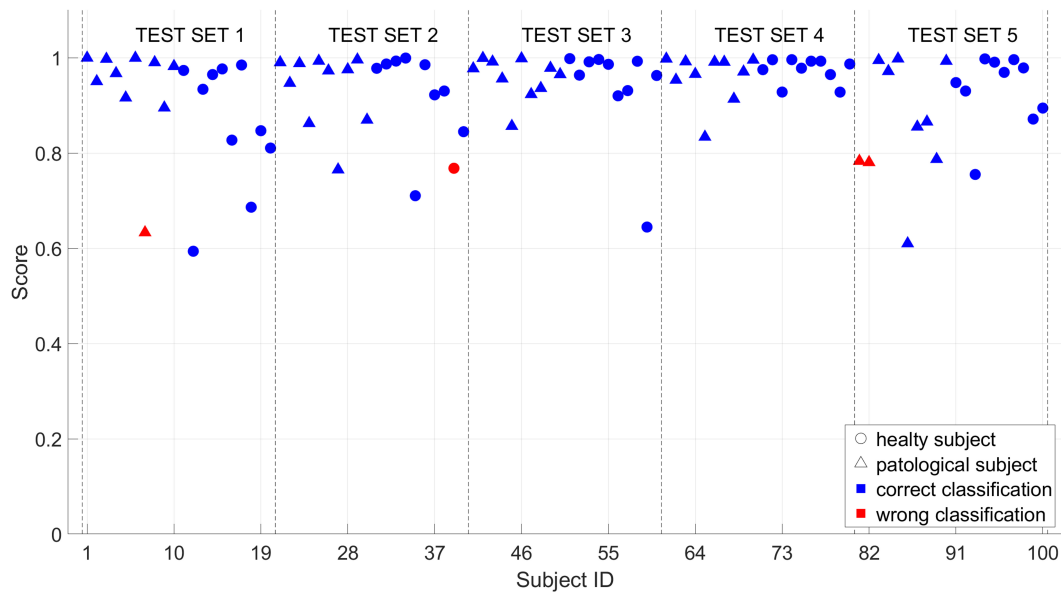
FIGURE 5.5: Classification scores for each subject. The mean scores of the blocks are reported for each subject. Dots represent healthy subjects, while triangles represent pathological ones. Blue-colored shapes (dot or triangle) correspond to correctly classified subjects, and red-colored shapes correspond to incorrectly classified subjects.

for each nerve fiber, the classification of a single image was obtained. Subsequently, for the entire subject, the classification was obtained by averaging the classifications of all of its images.

To compare this method with the one we proposed, both were evaluated on the same dataset of 100 subjects. The method proposed by Guimarães et al. [105] is based on the density and tortuosity estimation: from the literature review, a different value of density and tortuosity is expected in healthy versus pathological subjects. However, the method based on those aspects presented an accuracy much lower than that of the method proposed by us, based on CNN, which would consider the whole

TABLE 5.4: Classification accuracy achieved by the proposed multiple-image analysis and by a previously developed automated analysis of nerve density and morphology, on the same dataset (100 subjects).

Proposed **CNN**	*3 images* **simultaneously** *classified* 96%
Automated nerve tracing and **parameter estimation**: Density Short Range Tortuosity Long Range Tortuosity	**Mean** *classification of 3 images* 53% 62% 58%

images and not only some features. The results are reported in Table 5.4.

The better performances provided by the proposed framework seems to indicate an ability of CNNs to identify features that better describe the conditions of diabetic neuropathy, compared to the density and tortuosity defined by the other method under examination.

5.2.4 Discussion and conclusion

The proposed method is based on CNN: the goal is to find a correlation between IVCM images of the sub-basal plexus and the presence of diabetic neuropathy. The proposed method overcomes three common problems in this type of analysis, such as the need to identify and trace the nerve fibers, identify suitable features related to the presence of the pathology, and the limited visual field typical of the instrument used. The method bypasses the tracing problem and the feature identification one, by obtaining a direct classification between healthy and pathological subjects. Furthermore, the proposed algorithm simultaneously takes into account 3 corneal images of the left eye and 3 of the right eye of 100 subjects (50 healthy and 50 pathological). The 5-fold cross validation technique was used to evaluate the results.

Through this framework we obtained an average accuracy of 96%, which means that 96 out of 100 subjects were correctly classified, thus demonstrating the strong potential of deep learning algorithms in identifying features useful for clinical diagnosis. The proposed algorithm was compared with a state-of-the-art method: the proposed method far exceeded the results of the algorithm based on traditional techniques (tracing and subsequent extraction of predefined features).

The comparison between the two methods denotes that CNN provides a more complex analysis of the 3 images, implementing a process more similar to the human practice, than the analysis obtained by classifying each image separately and taking the average of the results. Indeed, clinical practice involves the observation of several images at the same time, looking for some characteristics that reveal the presence of pathologies (in this case diabetic neuropathy).

The idea of not considering the average, but implementing a global consideration helps to express a judgment even in those cases where the characteristics related to the pathology are present only in some of the acquired images (even only in one). This means that these features are crucial for the final diagnosis, even if they are present in only 1 in 3 images. The proposed CNN analysis appears to reproduce what clinicians do during the diagnostic process, simultaneously analyzing multiple images and, providing an overall classification for the whole subject.

In the literature, the problem of the reduced visual field of the IVCM has been addressed not only with the analysis of multiple images through the average of the results, but also with the montage/mosaicing technique, which requires acquisition of several images (mostly overlapped), is time consuming and can introduce artifacts as a result of registration errors. These characteristics of mosaicing, once again, underline the advantage of the proposed technique, which considers the information of

multiple images, without the risk of introducing errors, and which provides a result in a very fast manner. Compared to a mosaic, however, the proposed technique analyzes only three images simultaneously: better results may probably be achieved by increasing the number of simultaneously analyzed images.

Furthermore, an interesting result obtained with the proposed framework is linked to the classification score, which is a score that underlines how confident is the CNN of the class assigned to the 3 images under examination. On average, the score of the classifications is high (94%), while the score associated with incorrect classifications is on average much lower (74%). Therefore, the classification has a high score in most of the correct classifications; the score decreases when CNN assigns incorrect classes. From our point of view, this index can be interesting in clinical practice: the classification score could be used, as an example, to assess whether the proposed classification is reliable or whether more images or deeper investigations are required.

In conclusion, the proposed algorithm for CNN-based automatic classification provides, together with its confidence score, an interesting quantitative analysis that can be useful in clinical practice for the diagnosis of subjects with diabetic neuropathy.

5.3   Corneal neurodegeneration related to the level of glycemia – The Maastricht study

Diabetic neuropathy is known to be a a characteristic complication of diabetes. It is related to the tortuosity of the corneal nerve fibers, but as demonstrated by the previously presented analysis (section 5.2 *Multiple-Image Deep Learning Analysis for Neuropathy Detection in Corneal Nerve Images*), it is also linked to other aspects present in the confocal microscopy images of the sub-basal nerve plexus. In the cornea, when the subject is affected by type 2 diabetes mellitus (DM2), early morphological changes of the small nerve fibers are detectable: lower density of the corneal nerve branch, fiber density, fiber length, and fractal size are manifested. In diabetes, loss of corneal nerve fibers correlates with the severity of peripheral neuropathy manifested [173].

Physically, what happens is an imbalance in the factors present in the cornea: the corneal nerves and corneal epithelial cells provide mutual trophic support, that is they release growth factors and other mediators, which regulate the growth, mitosis, differentiation, and migration of the corneal epithelial cells and promote the extension of corneal neurites. When a person is affected by diabetes, the aqueous humor has elevated levels of glucose, which causes a decrease in the concentration of the factors and mediators mentioned above, causing corneal neuro degeneration [178].

From recent studies, it seems that the degeneration process linked to the conditions of hyperglycemia is a continuous (and linear) process, that begins before the onset of the disease. Regarding this neurodegenerative process, which begins in a prediabetic phase, numerous associations have been analyzed. Linear associations have

been shown to exist between glucose metabolism status (or higher blood glucose levels) with lower retinal nerve fiber layer thickness, more brain structural abnormalities, poorer peripheral nerve function and lower heart rate variability [179–183]. All of these aspects can be categorized as measures of neurodegeneration and/or neural dysfunction.

There are also some studies that analyze the influence of prolonged high blood sugar levels or the duration of diabetes disease with corneal degeneration [184–188]. However, these studies have some limitations: they were not population based; they had not taken into consideration the influence of other factors such as cardiovascular risk and lifestyle; and they did not investigate whether there is a linear relationship between blood glucose levels and corneal nerve fiber damage.

In collaboration with the University of Maastricht, a large and well-characterized population-based cohort study has been and is being conducted. What the study aims to investigate is whether a more adverse glucose metabolism state and higher blood glucose measurements are linearly associated with the level of the damage of the corneal nerve fibers. The level of damage is defined by some identified characteristics, such as: the density of the lower corneal nerve branch, fiber density, fiber length and fractal size.

This study is part of a larger project known as **The Maastricht Study**.

5.3.1   The Maastricht Study

Over the years, the study of type 2 diabetes mellitus (DM2) has been of great interest: data on pathogenetic pathways, diseases-related complications and comorbidities have been collected. However, in most cases, these mechanisms are considered separately.

The Maastricht study [189] aims, through state-of-the-art imaging techniques and extensive biobanking, to study the etiology and pathophysiology of type 2 diabetes, its classical complications, and its emerging comorbidities in relation to each other, using an extended phenotyping approach. Therefore, the study requires a large subset of patients with DM2, but also a population-based cohort of individuals without DM2 and individuals at high risk of developing DM2.

Thanks to the data collected, the objective of the study is, as mentioned above, to identify the determinants of the development and progression of type 2 diabetes, in particular focusing on the possible mechanisms that could give an explanation of why this disease accelerates the development of classic complications (such as cardiovascular diseases, retinopathies, neuropathies and nephropathies) and emerging comorbidities (such as cognitive decline, depression and the gastrointestinal tract, musculoskeletal and respiratory diseases). Furthermore, starting from the comorbidities, in the study, quality of life and use of health resources are assessed (at the moment, the treatment of diabetes is expensive, but it is interesting to underline that 50% of these costs are attributed to the disease itself, and the remaining 50% to the treatment of complications).

The study will include about 10,000 patients: these are people aged between 40 and 75 who reside in the southern part of the Netherlands (municipalities Maastricht, Margraten-Eijsden, Meersen and Valkenburg; Maastricht and Heuvelland in the province of Limburg). Participants were recruited through mass media campaigns, from municipal registers, and from the regional diabetes patient registry by mail starting in November 2010. Recruitment was stratified according to the known type 2 diabetes status, with an oversampling of individuals with type 2 diabetes, for efficiency reasons.

The patients are subjected to data collection, which is divided into several measurements, carried out using standardized protocols. Procedures are the same for all subjects, except for clinical contraindications. The data acquisition of each participant ends within 3 months.

The data collected include numerous aspects to investigate: laboratory data (blood and urine samples under specific conditions), physical tests (aimed at estimating total body fat and lean mass), physical function and performance (heart rate are analyzed, blood pressure and other data under specific activity / rest conditions), drug use, questionnaire (reporting medical history, diabetes familiarity, and all relevant indicators for the disease). These are the main ones related to the disease. The latter are followed by all the data collected in relation to the classic complications and comorbidities, we list some of them: oral glucose tolerance test (OGTT), end products of advanced glycation (AGE), electrocardiogram (ECG), Brachial ankle index, images of the retinal fundus, cognitive tests, questionnaires related to depression and anxiety, analysis of respiratory function and extensive ophthalmic evaluations. These include visual acuity, optical coherence tomography (OCT), ocular pressure, Scheimpflug analysis, perimetry, macula pigmentation, dynamic vessel analysis (DVA) and corneal confocal microscopy, which is the exam we were interested in during the Ph.D. project.

To the best of our knowledge, the Maastricht study is the largest prospective cohort study in the world that performs extensive phenotyping of DM2 and other chronic diseases in a population of about 10,000 individuals, providing increasingly comprehensive information to international research.

The Maastricht study has some limitations. The more important, there is no ethnic diversity in the study area, as almost all the subjects are of Caucasian origin. Therefore, the results of the Maastricht study cannot be extrapolated to other ethnic groups.

5.3.2   Material

For the analysis of the relationship between blood glucose levels (in healthy, prediabetic and diabetic patients) and the neurodegeneration of corneal nerve fibers, data from the Maastricht study were used: the rationale and methodology were described in the previous paragraph. In particular, in this study the cross-sectional data of 3,471 participants (mean age 59.4years, 48.4% were men, 14.7% with prediabetes, and 21%

with type 2 diabetes), who completed the basic data collection between November 2010 and December 2017, were analyzed: the examinations of each subject were carried out in a reduced time window of 3 months maximum.

The number of subjects analyzed (N = 3471) derives from a first selection of available data, referring to 8005 subjects: all those subjects whose corneal images were missing or of insufficiently adequate quality were rejected; those subjects who have no confounders data were also rejected.

The study was approved by the Institutional Medical Ethics Committee (NL31329.068.10) and the Netherlands Minister of Health, Welfare and Sport (permit 131088-105234-PG). All participants gave their informed consent in writing.

Each patient was subjected to in-vivo confocal microscopy analysis using Heidelberg Retina Tomograph III, equipped with the Rostock cornea module (Heidelberg Engineering, Heidelberg, Germany). Images of the corneal sub-basal plexus of each patient's left eye were acquired: individuals who had a corneal transplant or had a corneal infection of the left eye were excluded from the measurement.

The images of the corneal layer of interest were acquired randomly in a central region or in a peripheral region (i.e., at or above the lower vortex). Multiple images of standard instrument size ($400 \times 400 \ \mu m$, 384×384 pixels) were recorded and merged using a composite algorithm implemented in the HRT3 user interface (Heidelberg Engineering, Heidelberg, Germany). Real-time mapping was performed on an area up to $1600 \times 1600 \ \mu m$ (1536×1536 pixels). Figure 5.6 shows two images as an example.
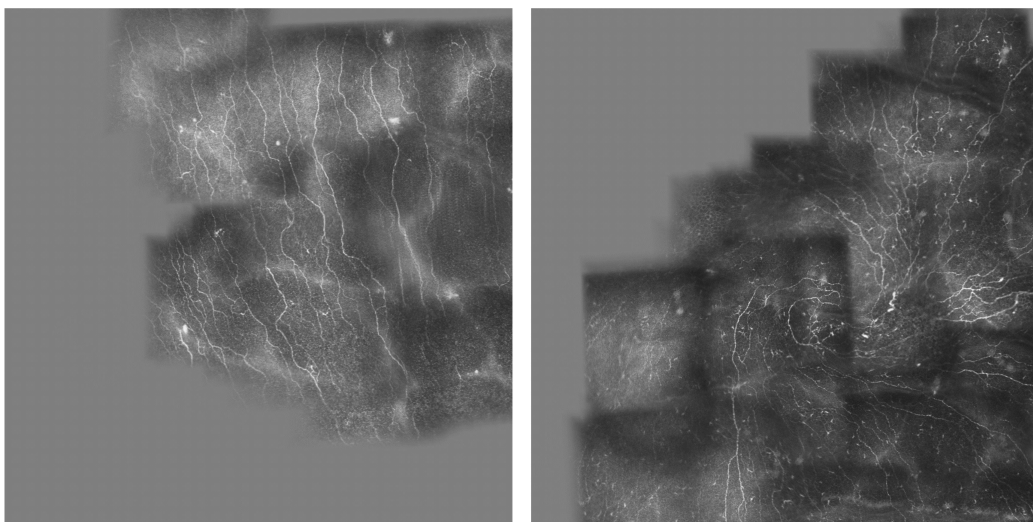
FIGURE 5.6: Representative mosaic images of the corneal sub-basal nerve plexus.

5.3.3 Methods

The study, as anticipated before, aims to investigate the association between the state of glucose metabolism (prediabetes and type 2 diabetes with respect to the normal

state of glucose metabolism) and blood glucose measurements (fasting glucose, 2-hour post-load glucose, hemoglobin A1c, skin autofluorescence and duration of diabetes) with composite Z-score of corneal nerve fiber measurements or with measurements of individual corneal nerve fibers (corneal nerve branch density, fiber density, fiber length and fractal size).This analysis is done following an adjustment for demographic, cardiovascular risk, and lifestyle factors.

In this paragraph we will mainly report the methods developed for the analysis of the IVCM images available and which allowed deriving the values of corneal nerve branch density, fiber density, fiber length, and fractal dimension, necessary to calculate the Composite Z-score characterizing the corneal nerve fiber degeneration. Instead, the methods used to study the associations between corneal features and other clinical parameters will be briefly analyzed.

As shown in the examples reported in Figure 5.6, the available images were obtained using the automatic software proposed by Heidelberg Engineering: in real time, during the acquisition, partial mosaics are generated, recording the individual images acquired. However, the mosaics thus obtained do not always cover the same area and are not always of the same size.

In Figure 5.6, a gray region can be recognized in which the corneal sub-basal layer has not been reconstructed. Therefore, the first step is to identify the reconstructed area (ROI, region of interest) to obtain an estimate of its extension and identify in which region to trace the nerve fibers.

For tracing, a U-Net-Based Convolutional Neural Network, previously trained on a single image, was used. To overcome the problem of the different size of the images, it was decided to divide the ROI identified into patches of a size equivalent to the single image (384x384 pixels).

The patches are extracted automatically, providing an overlap between them: the overlap of the regions allows for improving the results by analyzing the same region in different areas of the network input image. During the analysis on a single image, it was noticed that the edges of the images often presented worse results: this is probably due to the edge effect. In addition, the non-homogeneous illumination of the individual images is also reflected in the mosaic, and analyzing overlapping patches allows obtaining results that are less influenced by this non-homogeneous illumination.

Once all the patches of the image have been identified and analyzed, a probability map is reconstructed: the latter highlights the percentage with which each single pixel belongs to the class under observation. Starting from the probability map of each single patch, that of the original image is reconstructed, weighing the results, and taking into account possible errors related to edge effects.

The skeleton, representing the central line of each identified nerve fiber, is extracted from the probability map: some morphological and thresholding operations were carried out to improve the results and eliminate some small errors that are still present.

As presented in the chapter on tortuosity (Chapter 4), also in this case, to obtain an estimate of the parameters useful for clinical analysis, it was decided to separate the secondary nerve fibers, keeping the main fibers together. To do this, at each bifurcation, the features of the corresponding branches were extracted: direction, thickness, brightness, and length of the fiber. Subsequently, based on the extracted characteristics, the identified rules (do not show sudden changes in direction near a bifurcation, have comparable thickness, and, at the same time, have a comparable brightness) were applied to maintain or not continuity of the nerve fiber. An example of the tracing of nerve fibers and their bifurcation points is shown in Figure 5.7.
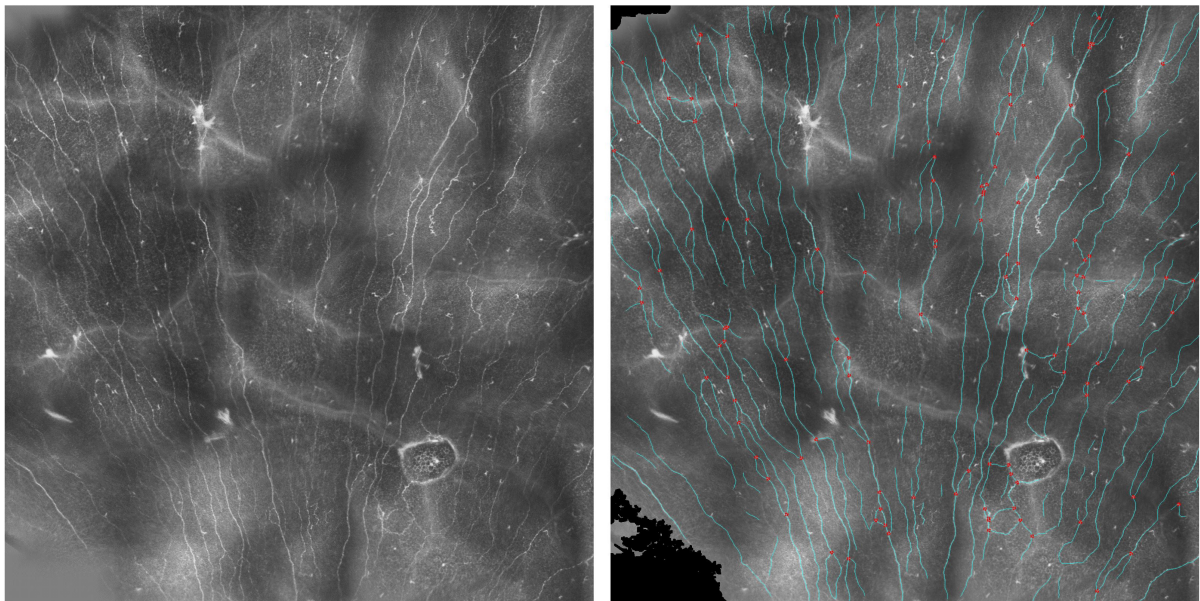
FIGURE 5.7: Representative mosaic image of the corneal sub-basal nerve plexus (left) and the results of the automatic analysis (right). On right, in black the area excluded from the analysis (area not been reconstructed from the automatic software proposed by Heidelberg Engineering), in red the bifurcation points, in light blue the skeleton of the nerve fibers recognized by the proposed algorithm.

From the tracing of nerve fibers and their analysis for the management of bifurcations, the following corneal nerves indices were estimated: corneal nerve branch density (number of corneal nerve branches per mm^2); corneal nerve fiber density (number of main corneal nerve fibers per mm^2); corneal nerve fiber length (total length of branches and main corneal nerve fibers per mm^2); and corneal nerve fractal dimension (quantification of nerve structure complexity).

The composite segmented images were reviewed manually and their quality was scored on the basis of a designated protocol. The intra-class and inter-observer correlation coefficients, both reliability indices, were ≥ 0.97 and ≥ 0.89, respectively.

The other available data are determinants (i.e., glucose metabolism status [entered as dummy variables for prediabetes, type 2 diabetes, or other types of diabetes versus normal glucose metabolism] and measures of glycemia [standardized fasting

plasma glucose, 2-hour post -load glucose, hemoglobin A1c, skin autofluorescence, and duration of diabetes]).

Through multivariate linear regression, the correlation between the latter and the outcomes was analyzed (that is, composite Z-score of corneal nerve fiber measures [main outcome] and different standardized corneal nerve fiber measures [corneal nerve branch density; corneal nerve fiber density; corneal nerve fiber length; and corneal nerve fractal dimension]).

5.3.4   Results

P was performed for trend analyzes, in order to test whether there was a linear trend in the correlation with the state of glucose metabolism as a determinant. Two statistical models were analyzed: one in which the glucose metabolism status was entered as a dummy variable and one in which the glucose metabolism status was entered as an ordinal variable. Using a likelihood ratio test, it was investigated whether the amount of variance explained by both models differed statistically significantly. Having obtained a p-value> 0.05, it was possible to state that both models are not different and, therefore, it was possible to assume a linear trend for all analyzes under study.

Several sets of adjustments were investigated, including those identified as *Model 3* reporting crude results adjusted for corneal confocal microscopy delay time, age, gender and education level [high, medium, low], systolic blood pressure outpatient, use of antihypertensive drugs [yes/no], waist circumference, total cholesterol / HDL cholesterol ratio, use of lipid-modifying drugs [yes / no], smoking status [never, previous, current] and alcohol consumption status [none, medium, high]. Biologically, these risk factors can be associated with corneal hyperglycemia and neurodegeneration. In this case, a more adverse glucose metabolism status was associated with a lower composite Z-score of corneal nerve fiber measures: beta [95% CI], type 2 diabetes versus normal glucose metabolism status -0.14 [-0.25; -0.04]; prediabetes versus normal glucose metabolism status -0.08 [-0.17; 0.03], P for trend = 0.001. By analyzing individual corneal nerve fiber measurements (not the composite Z-score, but the individual features), similar behavior in associations was observed.

Furthermore, in the same model, a correlation could also be observed between glycemia measures and corneal nerve fiber measures: higher blood glucose values corresponded to lower values of the Z-score.

Other analyzes were conducted and revealed quantitatively similar results. The only case that reported a change in the associations was gender: in women, a significant correlation was found between prediabetes, compared to the normal state of glucose metabolism, with the composite Z-score of corneal nerve fiber measurements (-0.18 [-0.33; -0.04] in women; and 0.04 [- 0.10; 0.19] in men).

5.3.5 Discussion and Conclusion

This study is the first large population-based study that investigated the association between corneal nerve damage and blood glucose level (fasting blood glucose, 2 hours post loading, hemoglobin A1c, skin autofluorescence and duration of diabetes) in healthy, pre-diabetic and type 2 diabetic patients. Furthermore, the state of glucose metabolism and other potential confounding factors were considered. We can highlight three main results:

- A more adverse glucose metabolism state and a higher blood glucose level are all linearly associated with a lower composite Z-score of the corneal nerve fiber.

- The associations found across the categories of glucose metabolism are linear in nature, highlighting the fact that the correlation of corneal nerve damage with blood glucose begins before the onset of type 2 diabetes and that there is a gradual decline in the composite Z-score of corneal neurodegenerations from the reference group (with normal glucose metabolism status) to prediabetes and type 2 diabetes.

- The betas identified for prediabetes and type 2 diabetes correspond, respectively, to 10 and 17 years of additional aging.

The results obtained are in line with previous research observations and new ones are reported (2-hour post-load glucose associations, skin autofluorescence with corneal nerve indices).

The clinical relevance of the results obtained is preventive: corneal neurodegeneration can be considered as a biomarker of diabetic neuropathy and therefore, and this kind of study for the detection of the initial stages of neuropathy is relatively inexpensive and easy to perform.

In conclusion, the presented study demonstrated more adverse glucose metabolism status and a higher blood glucose level are linearly associated with a composite Z-score of corneal nerve fiber measurements (the higher the former, the lower the Z-score). Associations have been shown to be independent of demographic, cardiovascular, or lifestyle risk factors. The morphological changes associated with glycemia in the corneal nerves have also been shown to be an early process that begins well before the onset of type 2 diabetes. It will be interesting, however, to analyze whether reduction in hyperglycemia can actually prevent corneal neurodegeneration.

5.4 Parkinson's disease with restless legs syndrome and IVCM

The human cornea is strongly innervated by small nerve fibers and, in the case of diabetes mellitus, the morphology of the small nerve fibers in the corneal sub-basal

nerve plexus has often been indicated as a marker of peripheral neuropathy associated with the disease. However, the study of the morphological characteristics of the corneal nerves has been relatively little studied in the case of Parkinson's disease (PD). Furthermore, the results in the literature are often conflicting: in one study, for example, significant increases in the values of corneal nerve fiber length (CNFL) and corneal nerve branch density (CNBD) were reported in patients with PD [190]; on the contrary, in a second study the values of CNFL and CNBD are significantly reduced in patients with PD compared to control subjects [191].

It is interesting to underline that 4-6 single image frames per eye were analyzed in 26 patients, respectively, in the first case, while in the second study 4-8 single image frames per eye of 26 patients were analyzed.

Studies in the literature have shown that imaging and analysis of a large area of the sub-basal plexus (mosaics) bring numerous advantages in the study of pathologies, as they provide more complete information and reduce inherent biases associated to the choice of a few microscope frames for nerve analysis.

For this reason, in the analysis presented below, mosaics were taken into consideration, attempting to reconstruct a sufficiently large area of the sub-basal plexus of each patient.

This study aims, in particular, to investigate whether small fiber neuropathy (SFN) is overrepresented in PD patients with concurrent restless legs syndrome (RLS) relative to PD patients without RLS, using in-vivo corneal confocal microscopy (IVCM) and quantitative sensory testing (QST) as part of small fiber assessment. SFN seems to be one of the triggering causes of restless legs syndrome (RLS), and, since a higher prevalence of peripheral neuropathy was highlighted in patients with Parkinson's disease, it is interesting to investigate this issue.

The data and results presented in this section refer to the studies presented in [7, 8].

5.4.1 The Parkinson's Disease

The interest in the study and analysis of Parkinson's starts from its spread: among the neurological disorders, it is the twelfth most common condition that leads to premature death (1.2%). Neurological disorders appear to be a significant cause of disability and death worldwide and, in the period from 1990 to 2015, there was an increase in deaths related to neurological disorders of 36.7% [192].

In particular, PD is a progressive neurological disease with clinical features of impaired motor and non-motor nerve function. There is no single definitive diagnostic test, but the final diagnosis is the result of the analysis of various clinical criteria. In addition, the classic symptoms are resting tremor, rigidity, bradykinesia and loss of postural reflexes; in some cases, to the latter, other motor (dysarthria, dysphagia, drooling, micrograph, shuffling gait, frostbite, dystonia) and non-motor (autonomic dysfunction, cognitive or neurobehavioral abnormalities, sleep disturbances, sensory abnormalities such as anosmia, paresthesia, and pain) symptoms will be added.

In PD, as well as in diabetes, multiple sclerosis, and Alzheimer's, there are cases of peripheral neuropathy, characterized by dysfunction of the sensory, motor, and autonomic nerves, which includes both small fibers neuropathy (autonomic) and large fibers neuropathy.

Peripheral neuropathy can be difficult to diagnose and for this reason the imaging technique through IVCM of the corneal nerves has been used: this technique is an equipment to visualize and quantify peripheral neuropathy in a rapid and non-invasive way, since the axons of the corneal nerves are part of the peripheral nervous system. Studies in the literature have demonstrated the clinical usefulness of these images in the analysis of peripheral neuropathy related to other diseases, first of all diabetes mellitus (already analyzed in the previous paragraphs).

5.4.2 Material

The study will cross-sectionally investigate whether small-fiber neuropathy is more present in patients with PD and who manifest RLS, compared to patients with PD without RLS or a control patient who does not have the disease. A total of 55 subjects were analyzed: these were patients with PD with RLS (n = 21) and without RLS (n = 21) and controls (n = 13).

Figure 5.8 shows sub-basal nerve plexus (SBNP) mosaics representative of healthy, PD + RLS and PD-RLS subjects. Participants, matched age and sex, were between the ages of 50 and 80 and had no previous corneal trauma, eye surgery (bilateral cataract surgery), and detection of pre-existing peripheral neuropathy, use of contact lenses, ongoing treatment with eye drops, or onset of stroke. (The control was smaller than initially expected, as some subjects refused to participate and/or did not meet the inclusion requirements).
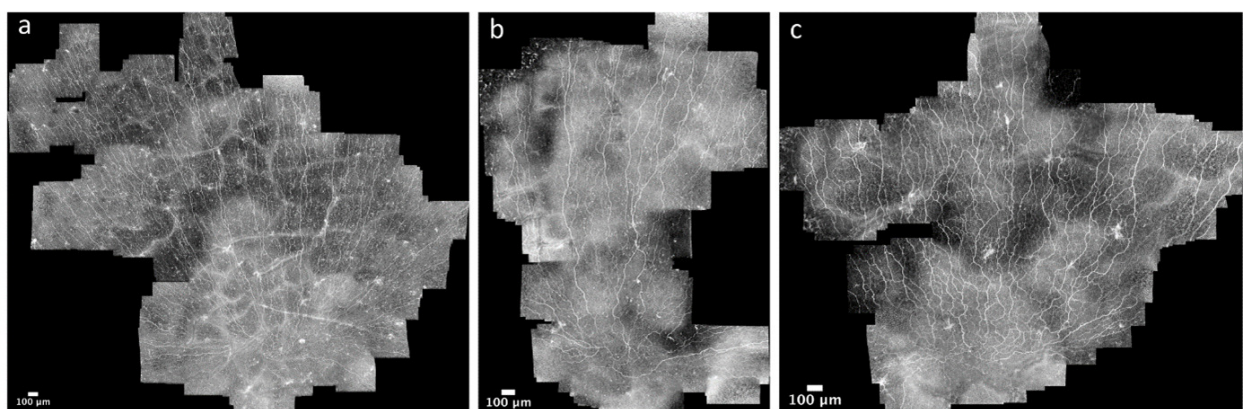
FIGURE 5.8: Representative IVCM mosaic images of the corneal sub-basal nerve plexus for the three study groups. (a) Control, (b) Subject with PD with RLS, (c) Subject with PD without RLS.

Each subject underwent confocal microscopy imaging of the corneal sub-basal plexus, and other relevant clinical diagnostic information was extracted from Utah

Early Neuropathy Scale (UENS), quantitative sensory testing (QST) and nerve conduction studies (NCS).

From IVCM images, an extended region of the cornea was reconstructed using the mosaic technique: the high quality wide-field images are a unique distinguishing feature, as they are the most extended published to date. Thanks to the reconstruction of the mosaics, it is possible to avoid the subjective selection of single visual fields (single images): this technique provides an objective view of the overall nerve plexus-base architecture, an accurate analysis of the SBNP models, and the exact quantification of the related parameters to nerve fibers and other structures present in this corneal layer.

The data are available for research and are more fully described in [8]. Written informed consent was obtained from all participants and the study was approved by the regional ethics council of Stockholm, Sweden (ref. Nr 2018/264-31/2).

5.4.3   Methods

The acquired images were first selected in order to exclude those in which there was a corneal layer different from the sub-basal plexus. This step is essential to reduce the mosaic processing time and to reduce the errors in the mosaic reconstruction phase (different layers could negatively influence the contrast of the characteristics). The selection was made through a set of classifiers based on support vector machines, each of which had been trained to separate one characteristic corneal tissue class (epithelium, SBNP, stroma) from any other tissue class.

The technique used for mosaic reconstruction is the one presented in [98]: it uses the phase correlation function, which turns out to be a consolidated approach to estimate the relative offset between two images. Briefly, each image is decomposed into 12 sub-images and their alignment with the sub-images deriving from other images is calculated: the phase correlation is calculated for all possible image pairs of a dataset.

The subdivision into 12 areas is necessary to analyze the deformation artifacts induced by movement and which are typical of the microscope, as they are closely linked to the image formation process. Once the translation vectors, that effectively estimate the position differences between the respective sub-images, have been calculated, the position coordinates of the sub-images are obtained through a system of linear equations with additional regularization terms. Finally, the mosaic is reconstructed using the weighted average of the overlaid original image data (where the coordinates of the individual lines are obtained from an appropriate interpolation).

The algorithm used to trace the nerve fibers present in mosaics is the one described previously in Guimaraes et al [97], customized for the required task, i.e., for the automated nerve fiber tracing, performed automated nerve parameter analysis and data extraction from whole and partial mosaics.

Briefly, the algorithm is based on 3 main steps: pre-processing, classification, and post-processing. The first step aims at enhanced the visibility of the corneal nerves,

through the use of a Top-Hat morphological filtering for the improvement of the contrast, a bank of log-Gabor filters (each with a different orientation) for highlights like-line objects. Through a thresholding operation, some pixels that may correspond to a nerve fiber are selected: the classification (as belonging or not belonging to the nerve fiber) occurs through a finer classification based on the support vector machines approach, whose inputs are the morphological- and intensity-based features previously extracted. The result is a binary image representing nerve segments with small gaps between each other, due to noise in the original image. To improve the results, the last post-processing step is applied: through morphological operations and assessments based on distance, angle, and intensity, the best connection-paths that correspond to the missing connections are identified and traced.

Figure 5.9 shows examples of automatically drawn mosaics.

Scale bar = 500 μm   Scale bar = 100 μm
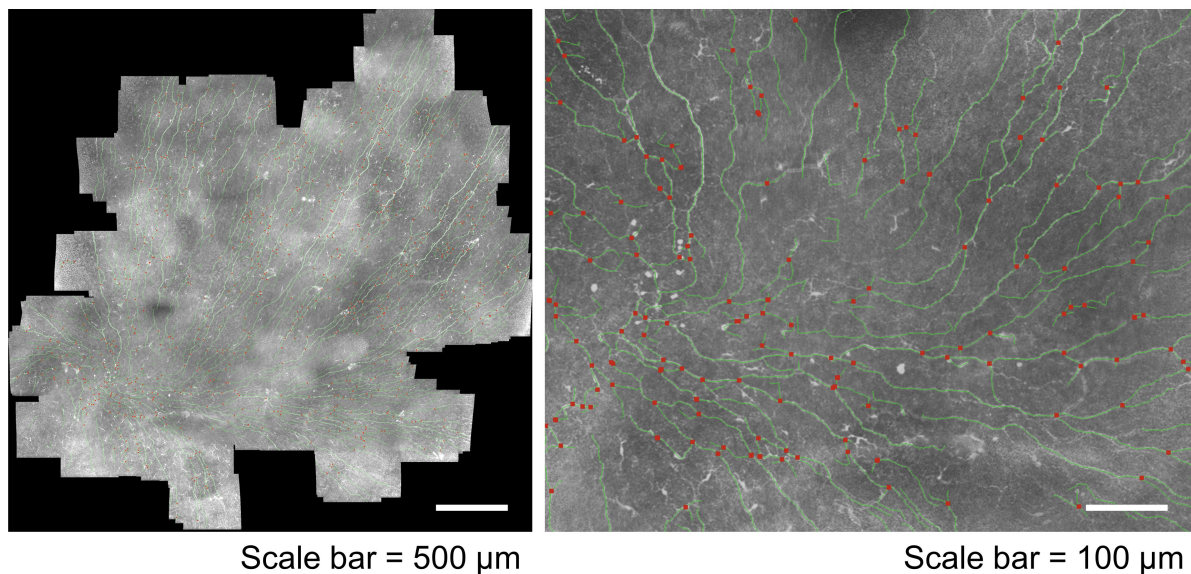
FIGURE 5.9: Left: Representative mosaic image from patient with PD and RLS showing traced nerve paths. Right: magnified region showing detailed nerve paths (green) and branching points (red).

Starting from the tracing obtained, quantitative nerve parameters were extracted. The proposed algorithm provides two common metrics in confocal microscopy studies: corneal nerve fiber length density (CNFL), defined as the total length of all nerves in the mosaic divided by the mosaic area (the region not reconstructed will be excluded), and the corneal nerve branching density (CNBD), defined as the total number of branching points divided by the mosaic area. The first is expressed in mm/mm^2, while the second is the number of branching points per mm^2.

5.4.4   Results

Regarding the parameters obtained from the in-vivo confocal microscopy mosaics, no differences were found between the groups under analysis. The length of the corneal nerve fibers (CNFL) or the density of the corneal nerve branch (CNBD) are

not altered in patients with Parkinson's Disease who have or do not have restless legs syndrome, compared to control patients.

To assess whether there were associations between neuropathy linked to peripheral nerve fibers and indirect measures of overall PD burden, a further analysis was performed by dividing the patients into two groups (with or without PD). A correlation was found between corneal parameters (CNFL and CNBD) and the duration of L-dopa therapy, however, of the two, only that with CNBD was significant once checked for both age and sex.

Other results, not directly related to IVCM images, but related to the other analyzes the patients underwent, are reported in [7]. Examples of mosaic CNFL (mCNFL) comparisons between the various groups are shown in Figures 5.10.
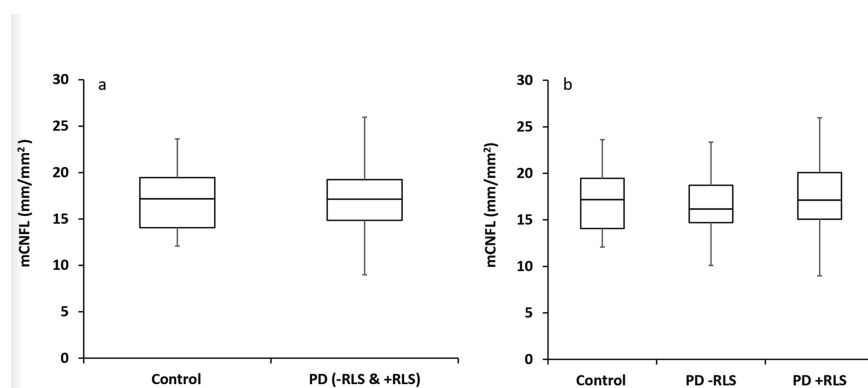
FIGURE 5.10: Box plots comparing mCNFL among the study groups. (a) Box plot comparing healthy controls vs. all Parkinson's disease (PD) patients as a single group. (b) Box plot comparing all study subgroups, including PD patients with and without RLS. Data represent quantification based on the single largest mosaic per eye.

5.4.5   Discussion and conclusion

The results obtained from this study show that small fiber neuropathy (SFN), evaluated by analyzing corneal nerve fibers present in the sub-basal plexus, does not seem to be related to restless legs syndrome (RLS) in Parkinson's disease (PD). In other words, RLS does not appear to represent a phenotypic expression of SFN in PD.

Therefore, the presented study did not confirm previous discriminatory results in corneal parameters compared to controls, but instead found similar CNBD and CNFL in all three groups. A previous study had stated that the analysis of data from 26 patients with PD, with variable duration of the disease, resulted in a significant increase in CNBD and CNFL.

For that study, 4-6 frames of IVCM images per eye were used, manually selected. Similarly, another study, also consisting of 26 patients with early-stage PD with minimal exposure to L-DOPA, presented the analysis of 4-8 frames of IVCM images per eye, again manually selected. However, in contrast to the previous case, the authors claim to have found a significant reduction in the values of CNBD and CNFL.

Compared to these previous studies, the proposed study shows great strength, namely the use of large mosaic representations of the sub-basal nerve plexus. Therefore, since the presented analysis uses a robust methodology, we are led to believe that CNBD and CNFL are not suitable as discriminatory diagnostic assessments in moderate PD.

Future analyzes may be conducted with greater attention to the analyzed region: the mosaics used present different areas and regions among the various patients. The inferocentral whorl region of the sub-basal plexus normally contains the densest concentration of sub-basal nerves, and this region has been analyzed separately in several studies. For this reason, in [8] the CNBD and CNFL values related to specific zones were also presented: within a full circular region centered on the center of the whorl with either an 800 μm diameter or 400 μm diameter, and only for the corresponding superior semicircular regions (extending from 9 to 3 o'clock).

5.5 Identification and tracing of dendritic cells

Until recently, it was thought that the cornea was a tissue with immune privilege, due to the absence of antigen presenting cells (APCs), as explained in Section 2.1.3 (*Dendritics cells*). However, recent studies have shown the existence of APCs also in the cornea, notably revealing a significant number of macrophages in the posterior stoma and inactive dendritic cells in the anterior stroma and corneal epithelium, especially between the basal and sub-basal layers [43].

In the epithelium, the dendritic cells residing in the basal and sub-basal layers are more numerous in the periphery than in the central region, where some of them insert the characteristic membranous processes between the epithelial cells in a similar way to the vertically oriented sensory nerve endings. This process serves to sample antigens present in the environment [48].

An increase in certain factors (metabolic activity, expression of membrane proteins and secretion of pro-inflammatory cytokines), and a change in morphology have been found to be closely linked to the maturation of Dendritic Cells (DCs): activated dendritic cells lose their structures adhesive and reorganize their own cytoskeleton through the projection of membranous processes capable of increasing their motility and thus allowing their migration into the secondary lymphoid organs [193].

Recent studies have reported an interesting correlation between density and morphological changes of dendritic cells and nerve density in the corneal sub-basal plexus, suggesting a potential interaction between the immune and nervous systems in the cornea [47]. In particular, the DCs and the sensory nerves of the cornea appear to be functionally and structurally interconnected. Although the DCs with characteristic dendrites are interconnected with nerve endings, rounded DCs are mainly located at nerve bifurcation points and along vertical fibers that cross the basement membrane ending in the epithelium [48].

Furthermore, the presence of dendritic cells and their state of maturation have been shown to be correlated with the presence and/or progress of some diseases, both ocular and systemic. Therefore, to study the correlation between these factors, it is necessary to identify and segment the cells present in the cornea. Until now, this process has been carried out manually by clinicians: the analysis only involves the identification of dendritic cells and their counting. Only a few more in-depth studies also investigate the distinction between mature and immature cells.

In collaboration with the University of New South Wales (UNSW, Sydney), it was decided to investigate the ability of deep learning techniques to identify and segment dendritic cells present in confocal microscopy images of the sub-basal plexus. This is the first step necessary for a subsequent more in-depth analysis in which to distinguish mature and immature cells and analyze their association with pathological or inflammatory states.

In this collaboration, the goal was to provide robust cornea descriptors in an automatic manner, with the ultimate goal of identifying and segmenting dendritic cells. Preliminary results were presented in [172].

5.5.1   Material

In this investigation, a dataset of 100 confocal images of the corneal sub-basal nerve plexus was used. Images were randomly selected from images captured at the central and mid-peripheral (temporal and superior) cornea of 20 healthy and 20 post-LASIK participants.
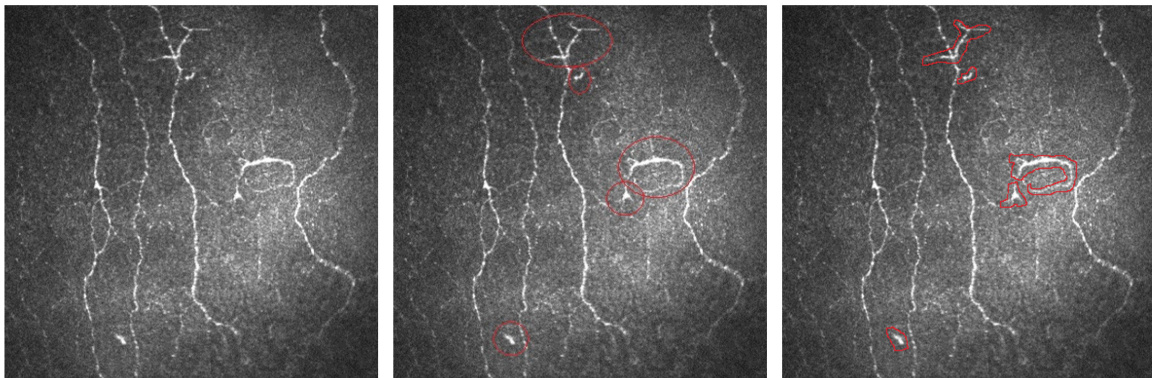
FIGURE 5.11: Representative images of manual analysis with mature and immature dendritic cells. Left: IVCM image of the original sub-basal nerve plexus. Center: identification and location of dendritic cells. Right: morphology delineated by manual contour tracing.

Images were acquired with the Heidelberg Retina Tomograph (HRT-II) instrument with the Rostock Cornea Module (Heidelberg Engineering GmbH, Heidelberg, Germany). Each image covers a field of 400x400 μm^2 (384x384 pixels). Acquisition was carried out at the School of Optometry and Vision Science of the University of New South Wales (UNSW, Sydney). Each image was anonymized by removing any patient information.

Each image was analyzed by expert clinicians: the location of the dendritic cells was identified by a red circle and the morphology was delineated by manual contour tracing.

An example of manual analysis is shown in Figure 5.11.

5.5.2 Methods

5.5.2.1 Pre-processing

In the first phase of the analysis, it was necessary to improve the characteristics of the images previously analyzed by the clinicians: tracing the contours in a precise manner is a very difficult task; for this reason, starting from the manual tracing of the contours and the identification of the region relative to the position of the cell, some thresholding and morphological operations have been carried out. Thanks to these first steps, it was possible to identify all and only the pixels that belong to dendritic cells, thus generating the masks that will be used to train the convolutional network (Ground truth).

In order to try to achieve the best possible result, given the reduced number of images available, we tried to provide the network with the greatest amount of information available: in this regard, it was decided to add to the newly created masks even the tracing of the nerve fibers. Nerve fibers appear as an important pattern in the images to be analyzed (as demonstrated in the previous chapters), and this information is certainly helpful in discriminating what appears as a "luminous object" in the IVCM images.

Not having available manual analysis of nerve fibers, it was decided to use the same technique seen for the UNet in previous chapters: nerve fibers were identified using the algorithm presented by Guimarães et al. [95], based on the use of support vector machines (SVM). Since automatic tracing is known to have a relative high percentage of False Positives, the pixels associated with the 'nerve' category and at the same time indicated by clinicians as DCs, have been labeled with the 'dendritic cell' class.

In addition, to further discriminate the nerves from the dendrites, some morphological operations were carried out: the traces of the segmented nerves were dilated and filtered according to the area of each connected region (eliminating the minor segments formed). Examples of the result of these first operations are shown in Figure 5.12 [Original figure in the top-left is the same shown in Figure 5.11; in the top right figure can be appreciate the difference with the original manual analysis].

5.5.2.2 Data augmentation

From the literature it is known that a convolutional neural network requires a large number of images for the learning phase of the network itself, in order to increase the generalization capacity of the model, while avoiding the problems related to overfitting.
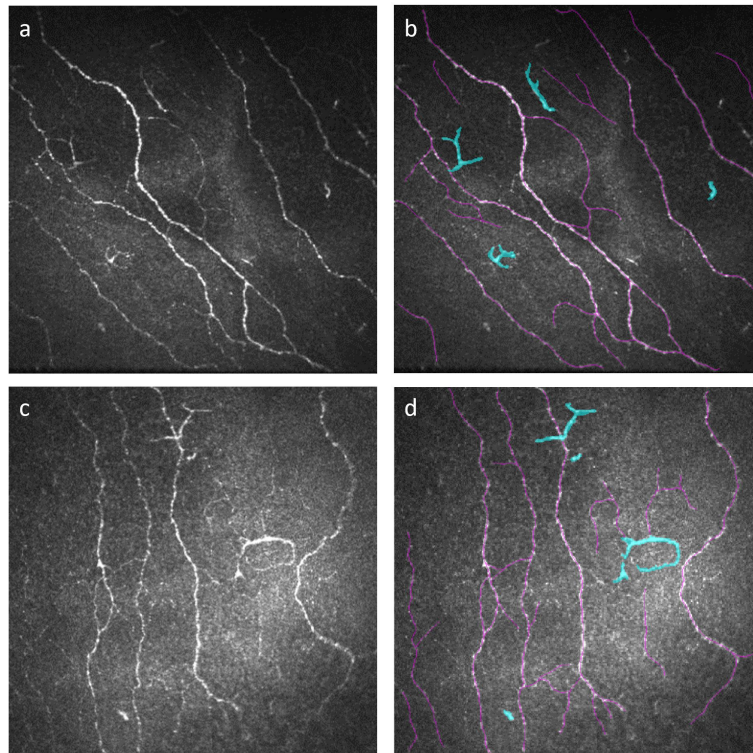
FIGURE 5.12: Representative images of the pre-processing step. (a, c) Original images. (b, d) Results of the pre-processing step, in light blue the identified and manually segmented DCs, refined automatically, in purple the automatic traced nerve fibers.

In the context of image segmentation (and more commonly in image classification), when the available training set has a restricted cardinality, a simple but effective method to increase the cardinality is represented by data augmentation, a technique that consists of processing the available data by processing them through transformations that allow label preservation. The most common are cutting, rotating, reflecting, or adding Gaussian noise to images.

In our case, some operations would not make sense: for example, the use of cropping and the subsequent resizing of the image would involve the use of images in which the dendritic cells would appear much larger than what can be seen via IVCM. Therefore, the transformations must be chosen carefully.

For this study, having available a reduced cardinality of images for the proposed task (only 100 images to train a network of millions of parameters), it was decided to implement some simple data augmentation techniques. In this regard, for each image, its own fipped version was created: each image was flipped horizontally and vertically, obtaining a larger dataset (300 images in total) for the training process.

An example of the image and its copies is shown in figure 5.13.
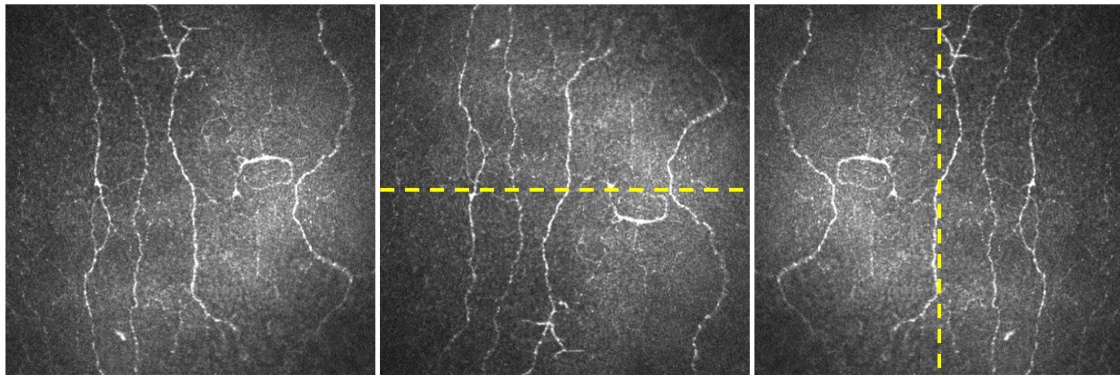
FIGURE 5.13: Data augmentation examples. From left to right: original image, horizontal flipped copy, vertical flipped copy. (The yellow line indicates the axis of reflection). The same operation is performed on ground truth images.

5.5.2.3 Convolutional neural network: structure and training

For this first analysis, it was decided to use the simplest structure seen so far, that is, the UNet used as a baseline to investigate the goodness of other structures derived from it during the study of nerve fibers. This network was chosen because, among those previously investigated in the nerve tracing analysis (Chapter 3), it is the one that has the least number of parameters. In the future, with a greater dataset available, it will be interesting to investigate how the results can improve thanks to the use of specific modules (such as ASPP seen above, which helps, through the multi-scale approach, to distinguish smaller objects such as DCs from larger objects such as nerve fibers).

The loss function used is the one used for the first analysis of the nerve fibers: the balanced cross-entropy (each category was weighted according to the inverse of the frequency of the class).

To establish the generalization capacity of a model, it is necessary to evaluate its performance on data not included in the training set and, therefore, never analyzed by the network. Given the very low cardinality of the training set, despite data augmentation, it was not possible to divide the training data into a train set and a test set.

Consequently, to validate the choice of the hyper-parameters, the leave-one-out cross-validation technique was used: the 300 images of the training set were divided into 100 subsets of three elements, each consisting of an original image and the two corresponding ones obtained with the data augmentation. Thus, 100 different training cycles were performed, each using 297 training images (99 original + 198 flipped) and excluding a different subset of 3. Of the latter, the original image was used for validation. [The correct name technique will be 100-fold cross-validation but given the nature of the three images that make up the fold (an original image and two copies), it can also be defined as leave-one-out cross-validation].

5.5.2.4   Post processing

In the decoding path, U-Net tries to recover the resolution of the original image lost in the contraction part, through layers of up-sampling and direct connections with the encoding path. However, it is very probable that the process of retrieving the spatial information is not perfectly accurate. Consequently, pixel-wise segmentation leads to many false positives, which refers to pixels classified by the network as "dendritic cell" but not labeled as such in the manual. However, false positives are not distributed throughout the image, but are typically localized in the areas surrounding the DCs. An adequate post-processing phase therefore allows the improvement of results.

Thanks to the introduction of some morphological and thresholding operations, it was possible to reduce the number of false positives: for each region classified as a "dendritic cell" by the UNet, those pixels that most likely belong to the cell were identified and, what could be FPs was discarded. This step made it possible to obtain a spatial reconstruction more in line with manual segmentation.

Other errors were eliminated thanks to a selection based on the extension: from the manual analysis, the minimum and maximum extension of the dendritic cells was estimated. With a margin of tolerance, a range was estimate in which the region representing the dendritic cell could fall. On the basis of it, those regions that present an extension outside this range were excluded from the tracing result.

Figure 5.14 shows an example of the results obtained by UNet with and without the post processing phase.
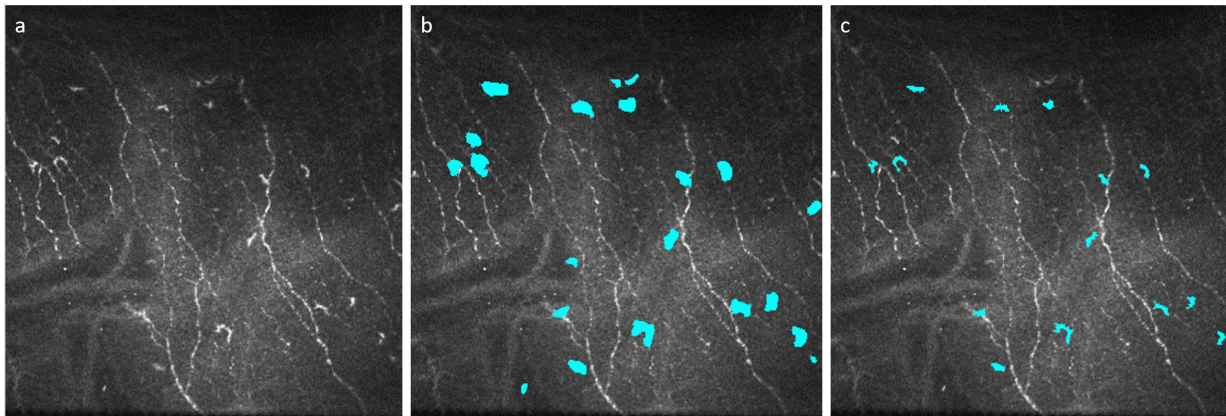
FIGURE 5.14: Example of the analysis performed by the proposed algorithm. (a) Original image. (b) Output of the CNN. (c) Result of the algorithm (result of the CNN underwent the post-processing step).

Finally, three images of the 100 analyzed were subjected to a further step of manual processing. These presented, in addition to dendritic cells and nerves, epithelial structures, or neuromas (hyperplastic proliferations of cells and nerve fibers), which were recognized by the algorithm as aggregates of DCs.

As was done for the nerves, also in this case it would have been appropriate to label the patterns represented by the epithelium or neuromas. In this case, however,

there were no manual tracings or algorithms capable of recognizing such structures. Therefore, it was decided to manually create binary masks identifying the regions presenting these patterns: these regions were excluded from the analysis of the results.

5.5.3 Results

Segmented images, obtained as a result of the proposed algorithm, were first subjected to visual inspection (qualitative analysis) and, subsequently, were automatically analyzed, extracting some quantitative statistical parameters (quantitative analysis).

Since manual analysis can be subject to errors, especially if it is a question of evaluating the pixel-by-pixel segmentation, and since the first step in the study of the DCs-pathologies correlation is related to the single identification of the dendritic cells, the performance of the model was evaluated both at the level of correspondence of the single pixels and at the level of correspondence of cells (regions of connected pixels).
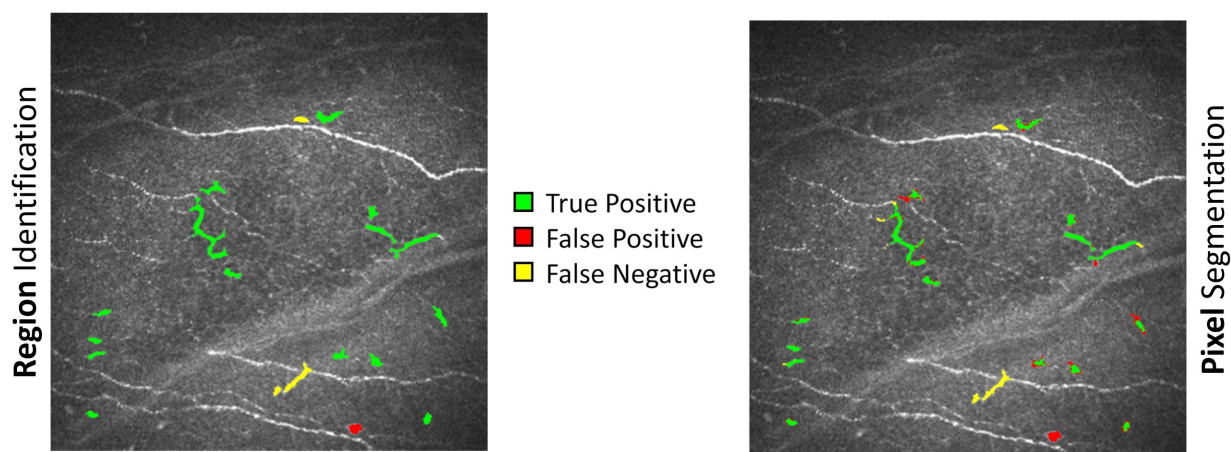
FIGURE 5.15: Representative images of the results of the quantitative analysis. On the left the comparison results in terms of region, on the right the results in terms of pixel. The figure on the right allows appreciating that some pixel classification errors are localized in the areas surrounding the DCs.

Both for the pixel-wise analysis and for the region-wise analysis (obtained from the comparison with the manual tracing, used as ground truth during the training phase), they were categorized as:

- TP (True Positive): pixels (respectively objects), correctly classified by the network as dendritic cells and therefore labeled as such also in the manual.

- FP (False Positive): pixels (respectively objects), labeled by the network as dendritic cells, but classified as "nerves" or "other" in manual segmentation.

- FN (False Negative): pixels (respectively objects), labeled by the network as "nerves" or "other", but classified as dendritic cells in manual segmentation.

Figure 5.15 shows an example of the results of the comparison: in particular, the regions/pixels corresponding to the TPs are represented in green, those corresponding to the FPs are represented in red, and the FNs are represented in blue.

Starting from the identification of the outcomes in TP, FP, and FN, two statistical indices were obtained: they were previously presented for the analysis of the results of the nerve fiber segmentation:

- *Sensitivity*, or **TPR** (True Positive Rate): the percentage of objects correctly classified as dendritic cells by the proposed algorithm.

- **FDR** (False Discovery Rate): the percentage of objects that are erroneously classified as dendritic cells by the proposed algorithm.

The results obtained are reported in Table 5.5.

TABLE 5.5: Segmentation results achieved by the proposed framework. Results are expressed as the average and standard deviation of TPR and FD for both analyses performed: region-level and pixel-level correspondence.

N=100	*TPR*	*FDR*
	Average ± Standard Deviation	
Region	96,25±8,04	19,95±16,39
Pixel	92,03±10,08	37,58±11,48

5.5.4 Discussion and Conclusion

The framework proposed for the analysis of dendritic cells in IVCM images has allowed us to obtain excellent results in terms of sensitivity. However, the FDR value is quite high. Through a visual inspection, it is possible to search for some plausible explanations about the high number of FP, found, among all, especially in some images.

For example, some acquired images turn out to be very noisy, characterized by uneven brightness and by the presence of "spots" of bright pixels whose nature is not clear but which the network has classified as DCs. An example is shown in Figure 5.16.

These regions often have a rounded shape and small size, but the difficulty of eliminating them in the post-processing phase lies in the morphological heterogeneity of the dendritic cells: in their immature form, the DCs can assume a small and globular conformation, thus preventing the definition of a morphological processing operation capable of removing false positives while preserving the automatic recognition of dendritic cells.
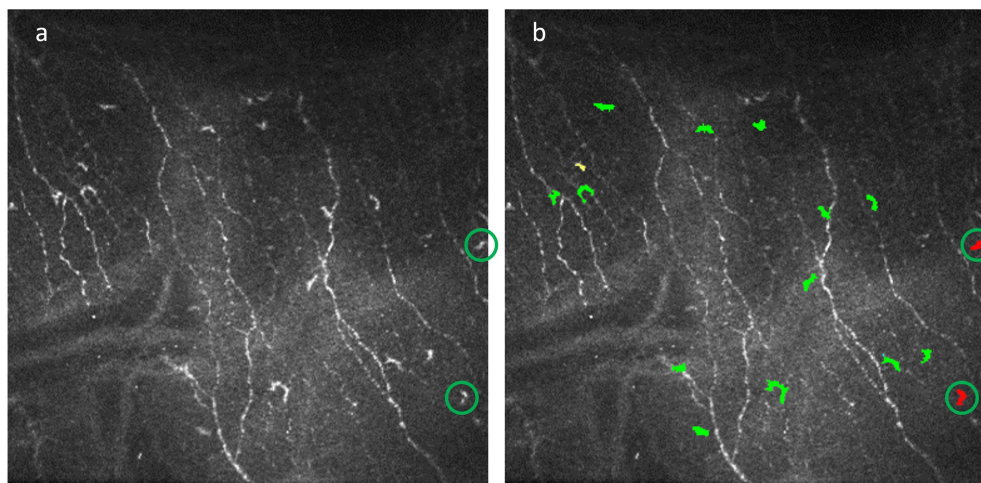
FIGURE 5.16: "Spots" of bright pixels that the network wrongly has classified as DCs. (a) Original image. (b) Results of the region-level quantitative analysis; the green color represents TPs, the red color represents FPs, and the yellow color represents the FNs.

Sometimes, it may happen that the network is able to identify some dendritic cells that may have escaped during the manual analysis: an accurate evaluation of the results of the automatic analysis by the clinicians is therefore essential ("review" phase), in which they will evaluate if the regions traced as wrong are errors.

These results encourage further developments aimed primarily at reducing the number of false positives and also at increasing sensitivity. It will therefore be important to create a better-supplied dataset: as is known the deep learning algorithms would require thousands of images during the training phase, while in this case only 100 were used. It was analyzed whether the use of other data augmentation techniques could further improve performance: from the rotation analysis, there were no major improvements.

It would also be interesting to consider more categories in the segmentation, defining more patterns:

- related to the morphological heterogeneity of dendritic cells, with the introduction of categories that distinguish the "mature dendritic cells" from the "immature dendritic cells".

- related to the presence of other structures, such as neuromas.

As reported above, the identification and segmentation of dendritic cells, present in the sub-basal layer of the cornea, is the first step in automating the study of the correlation that may occur between DCs and some ocular and/or systemic pathologies, such as post-operative inflammation. Therefore, it will be interesting to develop an algorithm capable of classifying images into healthy and pathological ones, starting from some parameters (such as, for example, the density of DCs) extracted through this first segmentation phase.

Chapter 6

Conclusion

In many cultures, it is customary to say that the eye represents *the mirror of the soul*[2]. In addition to providing a window into each person's inner world, it is also a window that allows us to obtain information on both ocular and systemic diseases. Of all the structures present in the eye, the most studied for this purpose is certainly the retina, whereas the analyzes focused on other structures, such as the cornea, are still few in comparison.

However, the cornea appears to be the most innervated tissue in the entire human body: inside it, there are numerous nerve endings, which make the entire tissue between 300 and 600 times more sensitive than human skin. Given its characteristics, the cornea and, in particular, the corneal sub-basal plexus arouse great interest in the ophthalmic sector. The analysis of corneal nerve fibers allows us to predict and monitor both ocular diseases and corneal diseases.

Thanks to the introduction of in-vivo confocal microscopy, it is possible to acquire images of all corneal layers quickly and non-invasively. This technique allows obtaining images of the sub-basal nerve plexus and therefore of the nerve fibers contained in it. The morphological features of nerve fibers and the clinical parameters calculated from them have been repeatedly shown to be related to a series of factors: advancing age, prolonged use of contact lenses, surgery (LASIK, PRK or corneal transplant), and above all to the presence and progress of ocular and systemic pathologies.

Visual inspection, manual or semi-automatic analyses are the methods often used in research and clinical practice. However, these are methodologies that are very time consuming, subjective, non-reproducible, and overall not practicable in daily clinical practice. To overcome these limits, various methods have been proposed in the literature, trying to automate the analysis of corneal nerve fibers. However, the proposed solutions have not reached universal acceptance and their use in clinical practice is not yet common.

One of the main objectives of this work was to investigate the feasibility of using the most advanced deep learning techniques for the fast and accurate tracing of corneal nerve fibers. Furthermore, since interest in clinical practice is linked to the possibility of estimating clinical parameters useful for diagnosis, an in-depth study of tortuosity has been developed. Finally, starting from the tracing and from the

---

[2]"The eyes are the mirror of the soul and reflect everything that seems to be hidden; and like a mirror, they also reflect the person looking into them". Paulo Coelho, Manuscript Found in Accra

analysis of tortuosity and other clinical parameters, the capabilities of the proposed framework were observed to generate a diagnosis (even of an early state of the disease), to carry out mass screening and to obtain information about the inflammatory state.

In this work, we have shown that the algorithm based on deep learning techniques is capable of segmenting the nerve fibers of single confocal microscopy images. The algorithm involves the use of a convolutional neural network called UNet. This architecture was used as a baseline, and numerous changes in its structure (addition of modules and/or connections) were investigated, in order to find the best one for the nerve fiber segmentation task. In addition, the necessary changes to be applied to the dataset used in the training phase were investigated, in order to provide the network with all the information available to obtain good results.

Finally, the optimal loss function to be used during the train phase was investigated. For this purpose, the most common functions present in the literature, designed for semantic segmentation, have been analyzed, with particular attention to those functions that take into account the unbalancing of classes. In addition, a new one has been proposed, developed *ad hoc* for identifying and tracing the centerline of nerve fibers.

The poposed loss function was then mediated with a function present in the literature in order to take into account the two main aspects that characterize the confocal microscopy images of the corneal nerve fibers: the presence of unbalanced classes and the interest in maintaining the continuity of the nerve fiber.

All proposed frameworks (characterized by different architectures, different datasets for the training phase, different loss functions) were tested on images other than those of the train dataset and which were manually analyzed.

The comparison between manual and automatic analysis immediately highlighted that deep learning is a technique that allows achieving excellent results in the segmentation of IVCM images. The correspondence achieved in terms of True Positive Rate and False Discovery Rate is very promising. In the best case analyzed, the indices obtained are respectively 92.75% for the TPR and 3.07% for the FDR.

The proposed technique has made it possible to improve with respect to the previously proposed methods, improving the accuracy of the tracing and decreasing the time required for the analysis.

An accurate algorithm for the segmentation of corneal nerve fibers is especially important for the extraction and estimation of clinical parameters useful for diagnosis. One of the most controversial disease markers is the tortuosity of the corneal nerves. This morphological feature has been repeatedly linked to the presence of different pathologies.

However, the lack of a precise and standard definition leads to numerous limitations in the reproducibility of the studies presented in literature. In this work, an automatic measure of corneal nerve tortuosity was proposed.

To this end, the classic problems of this type of analysis were faced: the presence of bifurcations along the nerve fibers, the need to consider numerous aspects (geometry,

angles, curvature, number of twists, complexity of the shape, ...), the need to obtain a unique index representative of the entire image, emulating as much as possible the clinical process. Therefore, in the frameworks proposed, it was taken into account that, during the clinical process, expert ophthalmologists classify an image as highly tortuous if only some nerves are long and twisted enough.

The proposed framework for the estimation of tortuosity was used to distinguish three different levels of tortuosity (low, medium, and high). Furthermore, the same automatic analysis process (tracing and estimation of tortuosity) was investigated for its ability to distinguish healthy and pathological subjects suffering from diabetic neuropathy.

In both cases, the results have been promising. In the case of classification, an accuracy of 96.6% was obtained from the comparison with the manual analysis, which consists of classification by expert clinics. Regarding the analysis of the presence of diabetic neuropathy, a first analysis of single images led to an accuracy of 77.18%.

However, it is important to emphasize that a confocal microscopy image covers a very limited field of the entire corneal surface (less than 0.02%). Some clinical parameters, such as nerve density, have been shown to be strongly influenced by the corneal region represented in the acquired image (i.e., near the center of the whirl, the density is higher than in the peripheral area). For this reason, numerous studies have underlined the importance of extracting clinical parameters from a larger field of view: this can be done by analyzing multiple images simultaneously or using the mosaic technique.

In the analysis performed, it was then decided to analyze whether the estimation of the tortuosity from multiple images of the same patient could improve the results. In this way, it was possible to achieve an accuracy of 86.31%.

The obtained results, even in this part of the work, are certainly encouraging and can be the starting point for continuous improvements in the analysis of corneal nerve fibers.

Imitating the behavior of clinicians during the analysis (choosing the optimal values of length and number of twists), taking into consideration various aspects related to tortuosity and wanting to distinguish the main fibers from their branches are aspects that improve performance and allow obtaining increasingly accurate estimates. Furthermore, the important aspect of this kind of analysis is that it takes into account clinical practice and makes the process objective.

Subsequently, in this work, some clinical investigations conducted on confocal microscopic images of the sub-basal plexus were reported. Starting from the analyzes presented above, some frameworks have been developed for the analysis of different pathological conditions (diabetes and Parkinson's disease), also taking into account the limited visual field just highlighted.

Each of the analyzes carried out has led to interesting results that make the proposed techniques an aid tool in clinical practice: the proposed methodologies have proven to be useful as tools for early diagnosis and for large-scale screening in some cases analyzed.

Finally, the last aspect related to the analysis of IVCM images reported in this work is related to the study of other corneal structures present in the sub-basal plexus: the dendritic cells. In the literature, it has been shown that thanks to the analysis of the dendritic cells present in this layer, it is possible to obtain further relevant information in the clinical field. The presence of dendritic cells and their state of maturation has been shown to be correlated with the presence and/or progress of some diseases (both ocular and systemic), as well as the inflammatory state (post-operative or not) of the cornea itself.

In this work, the ability of deep learning techniques to identify and segment dendritic cells was investigated. At the moment, manual analysis only involves the identification and counting of cells. Only the most in-depth studies provide an analysis of the state of maturation. Besides this, the cases in which the cell is entirely segmented are very rare. The goal of this analysis was to provide robust corneal descriptors in an automated way, with the ultimate goal of identifying and segmenting dendritic cells. The framework proposed for the analysis of dendritic cells in IVCM images has allowed us to obtain excellent and promising results in terms of sensitivity. However, the FDR value is quite high. Surely, a more extensive dataset and a deeper analysis will allow us to obtain excellent results in the future.

6.1 Future Development – This thesis as a start for new challenges

This research work focuses on the automation of the process of image analysis of confocal microscopy of the sub-basal plexus. It allows obtaining quantitative and reproducible descriptors capable of providing a segmentation of nerve fibers in an accurate and very rapid way. It significantly reduces image analysis times when applied to a large volume of clinical images. Thanks to this first step, it is possible to extract the clinical parameters in an easy, quantitative, and reproducible way.

Indeed, the clinical application studies presented in this thesis highlighted the ability of the proposed framework to perform an interesting analysis, which was rapid and accurate, allowing the analysis of numerous images and mosaics in a short time. However, the proposed results present only the starting point for more deep and generalized analyzes. Some limits are still present.

For example, in the analysis presented, the need to consider other structures in addition to nerve fibers, such as dendritic cells (of which a first feasibility study was reported) and neuromas, was highlighted. These structures, once identified and segmented, will be able to provide more useful information for clinical practice. With a complete segmentation of all the structures present in the individual confocal microscopy images (or in the mosaics obtained from them), it is possible to obtain an accurate estimate of the parameters of clinical interest and, therefore, generate a more reliable and precise diagnosis.

Even a study of the variability of clinical indices, in relation to the corneal region considered, is a topic of great interest: a single microscopy image is not sufficient to provide all the information necessary for diagnosis. Moreover, thanks to the mosaic technique, more and more clinicians agree that the variability between some images' parameters is related, not only to the presence of pathologies, but also to the corneal region analyzed. As it is not always possible to acquire the images necessary for the reconstruction of the entire cornea, it will be interesting to analyze the estimate of the parameters in relation to the region of acquisition.

A more in-depth analysis of the relevant parameters in the clinical setting is also needed. Standardizing the acquisition process and the segmentation of the images of the corneal sub-basal plexus, it will allow to obtain objective estimates of the parameters and therefore identify which ones highlight the presence of pathologies.

Furthermore, we should not forget the need to provide a precise description of the features of clinical interest, such as tortuosity. Expressing in greater detail what happens in clinical practice and therefore in the manual analysis of the images, will allow obtaining a more and more accurate mathematical expression of the index of interest. In this thesis, it has already been shown how emulating some passages of manual analysis (for example, considering only the nerve fibers that were sufficiently long and tortuous) has improved the results.

Finally, the studies presented are mostly based on small groups of patients, not always with great generalizability. Therefore, a larger cohort of patient data, presenting different racial or gender characteristics, could potentially increase the strength and generalizability of the proposed frameworks, further improving the results. A large dataset is essential to obtain an algorithm able to generalize well and be implemented in clinical practice

Bibliography

[1] L. J. Müller, G. F. Vrensen, L. Pels, B. N. Cardozo, and B. Willekens. "Architecture of human corneal nerves. | IOVS | ARVO Journals". In: *Investigative Ophthalmology & Visual Science* 38 (Apr. 1997), pp. 985–994. URL: https://iovs.arvojournals.org/article.aspx?articleid=2161847.

[2] Andrea Cruzat, Yureeda Qazi, and Pedram Hamrah. "In Vivo Confocal Microscopy of Corneal Nerves in Health and Disease HHS Public Access". In: *Ocul Surf* 15 (1 2017), pp. 15–47. DOI: 10.1016/j.jtos.2016.09.004.

[3] Elias Flockerzi, Loay Daas, and Berthold Seitz. "Structural changes in the corneal subbasal nerve plexus in keratoconus". In: *Acta Ophthalmologica* 98(8) (2020), e928–e932. DOI: 10.1111/aos.14432. URL: https://imagescience.org/meije.

[4] Gulfidan Bitirgen, Ahmet Ozkagnici, Rayaz A. Malik, and Refik Oltulu. "Evaluation of Contact Lens–Induced Changes in Keratoconic Corneas Using In Vivo Confocal Microscopy". In: *Investigative Ophthalmology & Visual Science* 54 (8 Aug. 2013), pp. 5385–5391. ISSN: 1552-5783. DOI: 10.1167/IOVS.13-12437. URL: www.iovs.org.

[5] Hiroshi Eguchi, Akio Hiura, Hiroshi Nakagawa, Shunji Kusaka, and Yoshikazu Shimomura. "Corneal Nerve Fiber Structure, Its Role in Corneal Function, and Its Changes in Corneal Diseases". In: *BioMed Research International* 2017 (2017). ISSN: 23146141. DOI: 10.1155/2017/3242649.

[6] Eszter A. Deák, Eszter Szalai, Noémi Tóth, Rayaz A. Malik, András Berta, and Adrienne Csutak. "Longitudinal Changes in Corneal Cell and Nerve Fiber Morphology in Young Patients with Type 1 Diabetes with and without Diabetic Retinopathy: A 2-Year Follow-up Study". In: *Investigative Ophthalmology & Visual Science* 60 (2 Feb. 2019), pp. 830–837. ISSN: 1552-5783. DOI: 10.1167/IOVS.18-24516. URL: https://doi.org/10.1167/.

[7] Mattias Andréasson, Neil Lagali, Reza A. Badian, et al. "Parkinson's disease with restless legs syndrome—an in vivo corneal confocal microscopy study". In: *npj Parkinson's Disease 2021 7:1* 7 (1 Jan. 2021), pp. 1–8. ISSN: 2373-8057. DOI: 10.1038/s41531-020-00148-5. URL: https://www.nature.com/articles/s41531-020-00148-5.

[8]   Reza A. Badian, Stephan Allgeier, Fabio Scarpa, et al. "Wide-field mosaics of the corneal subbasal nerve plexus in Parkinson's disease using in vivo confocal microscopy". In: *Scientific Data 2021 8:1* 8 (1 Nov. 2021), pp. 1–10. ISSN: 2052-4463. DOI: 10.1038/s41597-021-01087-3. URL: https://www.nature.com/articles/s41597-021-01087-3.

[9]   Giuseppe Giannaccare, Federico Bernabei, Marco Pellegrini, et al. "Bilateral morphometric analysis of corneal sub-basal nerve plexus in patients undergoing unilateral cataract surgery: A preliminary in vivo confocal microscopy study". In: *British Journal of Ophthalmology* (2020), pp. 174–179. ISSN: 14682079. DOI: 10.1136/bjophthalmol-2019-315449.

[10] Christos Theophanous, Deborah S. Jacobs, and Pedram Hamrah. "Corneal neuralgia after LASIK". In: *Optometry and Vision Science* 92 (9 Sept. 2015), e233–e240. ISSN: 15389235. DOI: 10.1097/OPX.0000000000000652. URL: https://journals.lww.com/optvissci/Fulltext/2015/09000/Corneal_Neuralgia_after_LASIK.16.aspx.

[11] Nilo Riva, Filippo Bonelli, Romina Mayra Lasagni Vitar, et al. "Corneal and Epidermal Nerve Quantification in Chemotherapy Induced Peripheral Neuropathy". In: *Frontiers in Medicine* 9 (Feb. 2022), p. 317. ISSN: 2296858X. DOI: 10.3389/FMED.2022.832344/BIBTEX.

[12] Karsten Winter, Patrick Scheibe, Bernd Köhler, Stephan Allgeier, Rudolf F. Guthoff, and Oliver Stachs. "Local Variability of Parameters for Characterization of the Corneal Subbasal Nerve Plexus". In: *http://dx.doi.org/10.3109/02713683.2015.1010686* 41 (2 Feb. 2015), pp. 186–198. ISSN: 14602202. DOI: 10.3109/02713683.2015.1010686. URL: https://www.tandfonline.com/doi/abs/10.3109/02713683.2015.1010686.

[13] John V. Forrester, Andrew D. Dick, Paul G. McMenamin, Fiona Roberts, and Eric Pearlman. "Anatomy of the eye and orbit". In: *The Eye* (Jan. 2016), 1–102.e2. DOI: 10.1016/B978-0-7020-5554-6.00001-0.

[14] Kristina Irsch and David L. Guyton. "Anatomy of Eyes". In: *Encyclopedia of Biometrics* (2009), pp. 11–16. DOI: 10.1007/978-0-387-73003-5_253.

[15] James K. Bowmaker. "Evolution of colour vision in vertebrates". In: *Eye (London, England)* 12 (Pt 3b) (3 1998), pp. 541–547. ISSN: 0950-222X. DOI: 10.1038/EYE.1998.143. URL: https://pubmed.ncbi.nlm.nih.gov/9775215/.

[16] K. M. Meek. "The cornea and sclera". In: *Collagen: Structure and Mechanics* (2008). Ed. by P. Fratzl, pp. 359–396. DOI: 10.1007/978-0-387-73906-9_13/COVER/. URL: https://link.springer.com/chapter/10.1007/978-0-387-73906-9_13.

[17] Sonal Gandhi and Sandeep Jain. "The anatomy and physiology of cornea". In: *Keratoprostheses and Artificial Corneas: Fundamentals and Surgical Applications* (Jan. 2015), pp. 19–25. DOI: 10.1007/978-3-642-55179-6_3/COVER/. URL: https://link.springer.com/chapter/10.1007/978-3-642-55179-6_3.

[18] P. Asbell and D. Brocks. "Cornea Overview". In: *Encyclopedia of the Eye* (Jan. 2010), pp. 522–531. DOI: 10.1016/B978-0-12-374203-2.00058-0.

[19] Nicholas R. Galloway, Winfried M. K. Amoaku, Peter H. Galloway, and Andrew C. Browning. "Basic Anatomy and Physiology of the Eye". In: *Common Eye Diseases and their Management* (2016), pp. 7–16. DOI: 10.1007/978-3-319-32869-0_2. URL: https://link.springer.com/chapter/10.1007/978-3-319-32869-0_2.

[20] Manik Goel, Renata G Picciani, Richard K Lee, and Sanjoy K Bhattacharya. "Aqueous Humor Dynamics: A Review". In: *The Open Ophthalmology Journal* 4 (1 Sept. 2010), p. 52. ISSN: 18743641. DOI: 10.2174/1874364101004010052. URL: /pmc/articles/PMC3032230//pmc/articles/PMC3032230/?report=abstracthttps://www.ncbi.nlm.nih.gov/pmc/articles/PMC3032230/.

[21] Helga Kolb. "Simple Anatomy of the Retina". In: *Webvision: The Organization of the Retina and Visual System* (Jan. 2012). URL: https://www.ncbi.nlm.nih.gov/books/NBK11533/.

[22] Derek W. DelMonte and Terry Kim. "Anatomy and physiology of the cornea". In: *Journal of Cataract and Refractive Surgery* 37 (3 2011), pp. 588–598. ISSN: 08863350. DOI: 10.1016/J.JCRS.2010.12.037.

[23] Mittanamalli S Sridhar. "Anatomy of cornea and ocular surface". In: (2018). DOI: 10.4103/ijo.IJO_646_17. URL: www.ijo.in.

[24] David C. Beebe. "Maintaining transparency: A review of the developmental physiology and pathophysiology of two avascular tissues". In: *Seminars in Cell and Developmental Biology* 19 (2 2008), pp. 125–133. ISSN: 10849521. DOI: 10.1016/J.SEMCDB.2007.08.014.

[25] Florian Rüfer, Anke Schröder, and Carl Erb. "White-to-white corneal diameter: Normal values in healthy humans obtained with the Orbscan II topography system". In: *Cornea* 24 (3 Apr. 2005), pp. 259–261. ISSN: 02773740. DOI: 10.1097/01.ICO.0000148312.01805.53. URL: https://journals.lww.com/corneajrnl/Fulltext/2005/04000/White_to_White_Corneal_Diameter__Normal_Values_in.3.aspx.

[26] Miguel Gonzalez-Andrades, Pablo Argüeso, and Ilene Gipson. "Corneal Anatomy". In: *Corneal Regeneration* (2019), pp. 3–12. DOI: 10.1007/978-3-030-01304-2_1. URL: https://link.springer.com/chapter/10.1007/978-3-030-01304-2_1.

[27] Usama Fares, Ahmad Muneer Otri, Mouhamed Ali Al-Aqaba, and Harminder S. Dua. "Correlation of central and peripheral corneal thickness in healthy corneas". In: *Contact Lens and Anterior Eye* 35 (1 Feb. 2012), pp. 39–45. ISSN: 1367-0484. DOI: 10.1016/J.CLAE.2011.07.004.

[28] Calvin Hanna, Donald S. Bicknell, and James E. O'brien. "Cell turnover in the adult human eye". In: *Archives of ophthalmology (Chicago, Ill. : 1960)* 65 (5 1961), pp. 695–698. ISSN: 0003-9950. DOI: 10.1001/ARCHOPHT.1961.01840020697016. URL: https://pubmed.ncbi.nlm.nih.gov/13711260/.

[29] Steven E. Wilson and Jong Wook Hong. "Bowman's layer structure and function: critical or dispensable to corneal function? A hypothesis". In: *Cornea* 19 (4 July 2000), pp. 417–420. ISSN: 0277-3740. DOI: 10.1097/00003226-200007000-00001. URL: https://pubmed.ncbi.nlm.nih.gov/10928749/.

[30] Jan Schroeter and Peter Rieck. "Endothelial evaluation in the cornea bank". In: *Developments in ophthalmology* 43 (2009), pp. 47–62. ISSN: 0250-3751. DOI: 10.1159/000223838. URL: https://pubmed.ncbi.nlm.nih.gov/19494636/.

[31] Carl F. Marfurt, Jeremiah Cox, Sylvia Deek, and Lauren Dvorscak. "Anatomy of the human corneal innervation". In: *Experimental Eye Research* 90 (4 Apr. 2010), pp. 478–492. ISSN: 0014-4835. DOI: 10.1016/J.EXER.2009.12.010.

[32] Linda J. Müller, Carl F. Marfurt, Friedrich Kruse, and Timo M.T. Tervo. "Corneal nerves: structure, contents and function". In: *Experimental Eye Research* 76 (5 May 2003), pp. 521–542. ISSN: 0014-4835. DOI: 10.1016/S0014-4835(03)00050-2.

[33] Joanna Kokot, Adam Wylęgała, Bogumił Wowra, Łukasz Wójcik, Dariusz Dobrowolski, and Edward Wylęgała. "Corneal confocal sub-basal nerve plexus evaluation: a review". In: *Acta Ophthalmologica* 96 (3 May 2018), pp. 232–242. ISSN: 1755-3768. DOI: 10.1111/AOS.13518. URL: https://onlinelibrary.wiley.com/doi/full/10.1111/aos.13518https://onlinelibrary.wiley.com/doi/abs/10.1111/aos.13518https://onlinelibrary.wiley.com/doi/10.1111/aos.13518.

[34] Ioannis N. Petropoulos, Georgios Ponirakis, Adnan Khan, et al. "Corneal confocal microscopy: ready for prime time". In: *https://doi.org/10.1111/cxo.12887* 103 (3 May 2021), pp. 265–277. ISSN: 14440938. DOI: 10.1111/CXO.12887. URL: https://www.tandfonline.com/doi/abs/10.1111/cxo.12887.

[35] Marta Sacchetti and Alessandro Lambiase. "Neurotrophic factors and corneal nerve regeneration". In: *Neural Regeneration Research* 12 (8 Aug. 2017), p. 1220. ISSN: 18767958. DOI: 10.4103/1673-5374.213534. URL: /pmc/articles/PMC5607810//pmc/articles/PMC5607810/?report=abstracthttps://www.ncbi.nlm.nih.gov/pmc/articles/PMC5607810/.

[36] Dipika V. Patel and Charles N.J. McGhee. "Mapping of the normal human corneal sub-Basal nerve plexus by in vivo laser scanning confocal microscopy". In: *Investigative ophthalmology & visual science* 46 (12 Dec. 2005), pp. 4485–4488. ISSN: 0146-0404. DOI: 10.1167/IOVS.05-0794. URL: https://pubmed.ncbi.nlm.nih.gov/16303938/.

[37] Dipika V. Patel and Charles N.J. McGhee. "In vivo laser scanning confocal microscopy confirms that the human corneal sub-basal nerve plexus is a highly dynamic structure". In: *Investigative ophthalmology & visual science* 49 (8 Aug. 2008), pp. 3409–3412. ISSN: 1552-5783. DOI: 10 . 1167 / IOVS . 08 – 1951. URL: https://pubmed.ncbi.nlm.nih.gov/18441297/.

[38] Martine J Jager, Dale S Gregerson, and J Wayne Streilein. *Regulators of immunological responses in the cornea and the anterior chamber of the eye*. 1995.

[39] Pedram Hamrah, Ying Liu, Qiang Zhang, and M. Reza Dana. "The corneal stroma is endowed with a significant number of resident dendritic cells". In: *Investigative ophthalmology & visual science* 44 (2 Feb. 2003), pp. 581–589. ISSN: 0146-0404. DOI: 10 . 1167 / IOVS . 02 – 0838. URL: https : // pubmed . ncbi . nlm . nih.gov/12556386/.

[40] Rabia Mobeen, Fiona Stapleton, Cecilia Chao, Michele C. Madigan, Nancy Briggs, and Blanka Golebiowski. "Corneal epithelial dendritic cell density in the healthy human cornea: A meta-analysis of in-vivo confocal microscopy data". In: *The Ocular Surface* 17 (4 Oct. 2019), pp. 753–762. ISSN: 1542-0124. DOI: 10.1016/J.JTOS.2019.07.001.

[41] Pedram Hamrah and M. Reza Dana. "Corneal antigen-presenting cells". In: *Chemical immunology and allergy* 92 (2007), pp. 58–70. ISSN: 1660-2242. DOI: 10 . 1159/000099254. URL: https://pubmed.ncbi.nlm.nih.gov/17264483/.

[42] Ellen J. Lee, James T. Rosenbaum, and Stephen R. Planck. "Epifluorescence intravital microscopy of murine corneal dendritic cells". In: *Investigative ophthalmology & visual science* 51 (4 Apr. 2010), pp. 2101–2108. ISSN: 1552-5783. DOI: 10 . 1167 / IOVS . 08 – 2213. URL: https : // pubmed . ncbi . nlm . nih . gov / 20007837/https://pubmed.ncbi.nlm.nih.gov/20007837/?dopt=Abstract.

[43] Takaaki Hattori, Hiroki Takahashi, and Reza Dana. "Novel insights into the immunoregulatory function and localization of dendritic cells". In: *Cornea* 35 (Suppl 1 2016), S49. ISSN: 15364798. DOI: 10 . 1097 / ICO . 0000000000001005. URL: /pmc / articles / PMC5067968 / /pmc / articles / PMC5067968 / ?report = abstracthttps://www.ncbi.nlm.nih.gov/pmc/articles/PMC5067968/.

[44] Dipyaman Ganguly, Stefan Haak, Vanja Sisirak, and Boris Reizis. "The role of dendritic cells in autoimmunity". In: *Nature reviews. Immunology* 13 (8 Aug. 2013), pp. 566–577. ISSN: 1474-1741. DOI: 10 . 1038 / NRI3477. URL: https : // pubmed.ncbi.nlm.nih.gov/23827956/.

[45] Brant R. Ward, James V. Jester, Akiko Nishibu, et al. "Local thermal injury elicits immediate dynamic behavioural responses by corneal Langerhans cells". In: *Immunology* 120 (4 Apr. 2007), p. 556. ISSN: 00192805. DOI: 10.1111/J.1365-2567 . 2006 . 02533 . X. URL: /pmc / articles / PMC2265913 / /pmc / articles / PMC2265913 / ?report = abstracthttps : // www . ncbi . nlm . nih . gov / pmc / articles/PMC2265913/.

[46] Tibor Z. Veres, Marina Shevchenko, Gabriela Krasteva, et al. "Dendritic cell-nerve clusters are sites of T cell proliferation in allergic airway inflammation". In: *The American journal of pathology* 174 (3 2009), pp. 808–817. ISSN: 1525-2191. DOI: 10.2353/AJPATH.2009.080800. URL: https://pubmed.ncbi.nlm.nih.gov/19179611/https://pubmed.ncbi.nlm.nih.gov/19179611/?dopt=Abstract.

[47] Takefumi Yamaguchi, Pedram Hamrah, and Jun Shimazaki. "Bilateral Alterations in Corneal Nerves, Dendritic Cells and Tear Cytokine Levels in Ocular Surface Disease". In: *Cornea* 35 (Suppl 1 2016), S65. ISSN: 15364798. DOI: 10.1097/ICO.0000000000000989. URL: /pmc/articles/PMC5658781//pmc/articles/PMC5658781/?report=abstracthttps://www.ncbi.nlm.nih.gov/pmc/articles/PMC5658781/.

[48] Nan Gao, Patrick Lee, and Fu Shin Yu. "Intraepithelial dendritic cells and sensory nerves are structurally associated and functional interdependent in the cornea". In: *Scientific Reports 2016 6:1* 6 (1 Nov. 2016), pp. 1–11. ISSN: 2045-2322. DOI: 10.1038/srep36414. URL: https://www.nature.com/articles/srep36414.

[49] Isabelle Jalbert, F. Stapleton, E. Papas, D. F. Sweeney, and M. Coroneo. "In vivo confocal microscopy of the human cornea". In: *The British Journal of Ophthalmology* 87 (2 Feb. 2003), p. 225. ISSN: 00071161. DOI: 10.1136/BJO.87.2.225. URL: /pmc/articles/PMC1771516//pmc/articles/PMC1771516/?report=abstracthttps://www.ncbi.nlm.nih.gov/pmc/articles/PMC1771516/.

[50] James V. Jester, H. Dwight Cavanagh, and Michael A. Lemp. "In Vivo Confocal Imaging Of The Eye Using Tandem Scanning Confocal Microscopy (TSCM):" in: *https://doi.org/10.1117/12.950323* 1028 (Feb. 1989), pp. 122–126. ISSN: 1996756X. DOI: 10.1117/12.950323. URL: https://www.spiedigitallibrary.org/conference-proceedings-of-spie/1028/0000/In-Vivo-Confocal-Imaging-Of-The-Eye-Using-Tandem-Scanning/10.1117/12.950323.fullhttps://www.spiedigitallibrary.org/conference-proceedings-of-spie/1028/0000/In-Vivo-Confocal-Imaging-Of-The-Eye-Using-Tandem-Scanning/10.1117/12.950323.short.

[51] Jay C. Erie, Jay W. McLaren, and Sanjay V. Patel. "Confocal Microscopy in Ophthalmology". In: *American Journal of Ophthalmology* 148 (5 Nov. 2009), pp. 639–646. ISSN: 0002-9394. DOI: 10.1016/J.AJO.2009.06.022.

[52] Rudolf F. Guthoff, Andrey Zhivov, and Oliver Stachs. "In vivo confocal microscopy, an inner vision of the cornea – a major review". In: *Clinical & Experimental Ophthalmology* 37 (1 Jan. 2009), pp. 100–117. ISSN: 1442-9071. DOI: 10.1111/J.1442-9071.2009.02016.X. URL: https://onlinelibrary.wiley.com/doi/full/10.1111/j.1442-9071.2009.02016.xhttps://onlinelibrary.wiley.com/doi/abs/10.1111/j.1442-9071.2009.02016.

xhttps://onlinelibrary.wiley.com/doi/10.1111/j.1442-9071.2009.02016.x.

[53] S. W. Paddock. "Principles and practices of laser scanning confocal microscopy". In: *Molecular Biotechnology 2000 16:2* 16 (2 2000), pp. 127–149. ISSN: 1559-0305. DOI: 10.1385/MB:16:2:127. URL: https://link.springer.com/article/10.1385/MB:16:2:127.

[54] Jay C. Erie, Jay W. McLaren, David O. Hodge, and William M. Bourne. "The effect of age on the corneal subbasal nerve plexus". In: *Cornea* 24 (6 Aug. 2005), pp. 705–709. ISSN: 0277-3740. DOI: 10.1097/01.ICO.0000154387.51355.39. URL: https://pubmed.ncbi.nlm.nih.gov/16015090/.

[55] Adrian Guerrero-Moreno, Christophe Baudouin, Stéphane Melik Parsadaniantz, et al. "Morphological and Functional Changes of Corneal Nerves and Their Contribution to Peripheral and Central Sensory Abnormalities". In: 14 (Dec. 2020), p. 610342. ISSN: 16625102. URL: www.frontiersin.org/pmc/articles/PMC7758484//pmc/articles/PMC7758484/?report=abstracthttps://www.ncbi.nlm.nih.gov/pmc/articles/PMC7758484/.

[56] Dimitrios Vagenas, Nicola Pritchard, Katie Edwards, et al. "Optimal image sample size for corneal nerve morphometry". In: *Optometry and vision science : official publication of the American Academy of Optometry* 89 (5 May 2012), pp. 812–817. ISSN: 1538-9235. DOI: 10.1097/OPX.0B013E31824EE8C9. URL: https://pubmed.ncbi.nlm.nih.gov/22407254/.

[57] Xin Yuan Zhang, Mengliang Wu, Holly R. Chinnery, and Laura E. Downie. "Defining an Optimal Sample Size for Corneal Epithelial Immune Cell Analysis Using in vivo Confocal Microscopy Images". In: *Frontiers in Medicine* 0 (June 2022), p. 1477. ISSN: 2296-858X. DOI: 10.3389/FMED.2022.848776. URL: https://www.frontiersin.org/articles/10.3389/fmed.2022.848776/full.

[58] Qiong Liu, Alison M. McDermott, and William L. Miller. "Elevated nerve growth factor in dry eye associated with established contact lens wear". In: *Eye & contact lens* 35 (5 Sept. 2009), pp. 232–237. ISSN: 1542-233X. DOI: 10.1097/ICL.0B013E3181B3E87F. URL: https://pubmed.ncbi.nlm.nih.gov/19672199/.

[59] Edward Lum, Blanka Golebiowski, and Helen A. Swarbrick. "Mapping the corneal sub-basal nerve plexus in orthokeratology lens wear using in vivo laser scanning confocal microscopy". In: *Investigative ophthalmology & visual science* 53 (4 2012), pp. 1803–1809. ISSN: 1552-5783. DOI: 10.1167/IOVS.11-8706. URL: https://pubmed.ncbi.nlm.nih.gov/22395884/.

[60] Mehmet C. Mocan, Pinar Topcu Yilmaz, Murat Irkec, and Mehmet Orhan. "In vivo Confocal Microscopy for the Evaluation of Corneal Microstructure in Keratoconus". In: *http://dx.doi.org/10.1080/02713680802439219* 33 (11-12 Nov.

2009), pp. 933–939. ISSN: 02713683. DOI: 10.1080/02713680802439219. URL: https://www.tandfonline.com/doi/abs/10.1080/02713680802439219.

[61]   Dipika V. Patel, Mitra Tavakoli, Jennifer P. Craig, Nathan Efron, and Charles N.J. McGhee. "Corneal sensitivity and slit scanning in vivo confocal microscopy of the subbasal nerve plexus of the normal central and peripheral human cornea". In: *Cornea* 28 (7 2009), pp. 735–740. ISSN: 1536-4798. DOI: 10.1097/ICO.0B013E318193E0E3. URL: https://pubmed.ncbi.nlm.nih.gov/19574916/.

[62]   José M. Benítez-Del-Castillo, M. Carmen Acosta, Mohamed A. Wassfi, David Díaz-Valle, José A. Gegúndez, Cristina Fernandez, and Julian García-Sánchez. "Relation between corneal innervation with confocal microscopy and corneal sensitivity with noncontact esthesiometry in patients with dry eye". In: *Investigative ophthalmology & visual science* 48 (1 Jan. 2007), pp. 173–181. ISSN: 0146-0404. DOI: 10.1167/IOVS.06-0127. URL: https://pubmed.ncbi.nlm.nih.gov/17197530/.

[63]   B. M. Hoçal, Nurgul Örnek, G. Zilielioğlu, and A. H. Elhan. "Morphology of corneal nerves and corneal sensation in dry eye: a preliminary study". In: *Eye (London, England)* 19 (12 2005), pp. 1276–1279. ISSN: 0950-222X. DOI: 10.1038/SJ.EYE.6701760. URL: https://pubmed.ncbi.nlm.nih.gov/15550934/.

[64]   Edoardo Villani, Daniela Galimberti, Francesco Viola, Chiara Mapelli, and Roberto Ratiglia. "The cornea in Sjogren's syndrome: an in vivo confocal study". In: *Investigative ophthalmology & visual science* 48 (5 May 2007), pp. 2017–2022. ISSN: 0146-0404. DOI: 10.1167/IOVS.06-1129. URL: https://pubmed.ncbi.nlm.nih.gov/17460255/.

[65]   Antoine Labbé, Haiyan Alalwani, Charles Van Went, Emmanuelle Brasnu, Dan Georgescu, and Christophe Baudouin. "The relationship between subbasal nerve morphology and corneal sensation in ocular surface disease". In: *Investigative ophthalmology & visual science* 53 (8 July 2012), pp. 4926–4931. ISSN: 1552-5783. DOI: 10.1167/IOVS.11-8708. URL: https://pubmed.ncbi.nlm.nih.gov/22695962/.

[66]   Luca Agnifili, Lorenza Brescia, Edoardo Villani, et al. "In Vivo Confocal Microscopy of the Corneal Sub-Basal Nerve plexus in Medically Controlled Glaucoma". In: *Microscopy and Microanalysis* 28 (2 Apr. 2022), pp. 496–503. ISSN: 1431-9276. DOI: 10.1017/S1431927621013969. URL: https://www.cambridge.org/core/journals/microscopy-and-microanalysis/article/abs/in-vivo-confocal-microscopy-of-the-corneal-subbasal-nerve-plexus-in-medically-controlled-glaucoma/5FC881DD43AE6178A1F77F7E9D444AE4.

[67] Nobuo Ishida, Gullapalli N. Rao, Manuel Del Cerro, and James V. Aquavella. "Corneal Nerve Alterations in Diabetes Mellitus". In: *Archives of Ophthalmology* 102 (9 1984), pp. 1380–1384. ISSN: 15383601. DOI: `10.1001/ARCHOPHT.1984.01040031122038`.

[68] Solomon Tesfaye and Dinesh Selvarajah. "Advances in the epidemiology, pathogenesis and management of diabetic peripheral neuropathy". In: *Diabetes/Metabolism Research and Reviews* 28 (SUPPL. 1 Feb. 2012), pp. 8–14. ISSN: 1520-7560. DOI: `10.1002/DMRR.2239`. URL: `https://onlinelibrary.wiley.com/doi/full/10.1002/dmrr.2239https://onlinelibrary.wiley.com/doi/abs/10.1002/dmrr.2239https://onlinelibrary.wiley.com/doi/10.1002/dmrr.2239`.

[69] Roberto Ceravolo, Giovanni Cossu, Monica Bandettini di Poggio, et al. "Neuropathy and levodopa in Parkinson's disease: evidence from a multicenter study". In: *Movement disorders : official journal of the Movement Disorder Society* 28 (10 Sept. 2013), pp. 1391–1397. ISSN: 1531-8257. DOI: `10.1002/MDS.25585`. URL: `https://pubmed.ncbi.nlm.nih.gov/23836370/https://pubmed.ncbi.nlm.nih.gov/23836370/?dopt=Abstract`.

[70] Cory Toth, Kim Breithaupt, Shaohua Ge, et al. "Levodopa, methylmalonic acid, and neuropathy in idiopathic Parkinson disease". In: *Annals of neurology* 68 (1 July 2010), pp. 28–36. ISSN: 1531-8249. DOI: `10.1002/ANA.22021`. URL: `https://pubmed.ncbi.nlm.nih.gov/20582991/https://pubmed.ncbi.nlm.nih.gov/20582991/?dopt=Abstract`.

[71] Giulio Ferrari, Franco Gemignani, and Claudio Macaluso. "Chemotherapy-associated peripheral sensory neuropathy assessed using in vivo corneal confocal microscopy". In: *Archives of neurology* 67 (3 Mar. 2010), pp. 364–365. ISSN: 1538-3687. DOI: `10.1001/ARCHNEUROL.2010.17`. URL: `https://pubmed.ncbi.nlm.nih.gov/20212239/`.

[72] Oliver Stachs, Andrey Zhivov, Robert Kraak, Marine Hovakimyan, Andreas Wree, and Rudolf Guthoff. "Structural-functional correlations of corneal innervation after LASIK and penetrating keratoplasty". In: *Journal of Refractive Surgery* 26 (3 2010), pp. 159–167. ISSN: 1081597X. DOI: `10.3928/1081597x-20100224-01`.

[73] Cecilia Chao, Blanka Golebiowski, and Fiona Stapleton. "The role of corneal innervation in LASIK-induced neuropathic dry eye". In: *The ocular surface* 12 (1 2014), pp. 32–45. ISSN: 1937-5913. DOI: `10.1016/J.JTOS.2013.09.001`. URL: `https://pubmed.ncbi.nlm.nih.gov/24439045/`.

[74] Linna TU, Vesaluoma MH, Pérez-Santonja JJ, Petroll WM, Alió JL, and Tervo TM. "Effect of myopic LASIK on corneal sensitivity and morphology of subbasal nerves - PubMed". In: *Invest Ophthalmol Vis Sci* 41(2) (Feb. 2000), pp. 393–397. URL: `https://pubmed.ncbi.nlm.nih.gov/10670467/`.

[75]   Ioannis N. Petropoulos, Tauseef Manzoor, Philip Morgan, et al. "Repeatability of in vivo corneal confocal microscopy to quantify corneal nerve morphology". In: *Cornea* 32 (5 May 2013). ISSN: 1536-4798. DOI: `10.1097/ICO.0B013E3182749419`. URL: `https://pubmed.ncbi.nlm.nih.gov/23172119/`.

[76]   T. Wu, A. Ahmed, V. Bril, A. Orszag, E. Ng, P. Nwe, and B. A. Perkins. "Variables associated with corneal confocal microscopy parameters in healthy volunteers: implications for diabetic neuropathy screening". In: *Diabetic medicine : a journal of the British Diabetic Association* 29 (9 Sept. 2012). ISSN: 1464-5491. DOI: `10.1111/J.1464-5491.2012.03678.X`. URL: `https://pubmed.ncbi.nlm.nih.gov/22519850/`.

[77]   Marlen Parissi, Georgios Karanis, Stefan Randjelovic, et al. "Standardized Baseline Human Corneal Subbasal Nerve Density for Clinical Investigations With Laser-Scanning in Vivo Confocal Microscopy". In: *Investigative Ophthalmology & Visual Science* 54 (10 Oct. 2013), pp. 7091–7102. ISSN: 1552-5783. DOI: `10.1167/IOVS.13-12999`. URL: `www.iovs.org`.

[78]   D. V. Patel and C. N.J. McGhee. "In vivo confocal microscopy of human corneal nerves in health, in ocular and systemic disease, and following corneal surgery: a review". In: *British Journal of Ophthalmology* 93 (7 July 2009), pp. 853–860. ISSN: 0007-1161. DOI: `10.1136/BJO.2008.150615`. URL: `https://bjo.bmj.com/content/93/7/853https://bjo.bmj.com/content/93/7/853.abstract`.

[79]   Ana Ferreira, João Lamas, Luís Gomes, et al. "NeuroCornea-Diabetic peripheral neuropathy early diagnosis and follow-up through in vivo automatic analysis of corneal nerves morphology". In: *1st Portuguese Meeting in Biomedical Engineering, ENBENG 2011* (2011). DOI: `10.1109/ENBENG.2011.6026071`.

[80]   Bryan M. Williams, Davide Borroni, Rongjun Liu, et al. "An artificial intelligence-based deep learning algorithm for the diagnosis of diabetic neuropathy using corneal confocal microscopy: a development and validation study". In: *Diabetologia* 63 (2 Feb. 2020), pp. 419–430. ISSN: 14320428. DOI: `10.1007/S00125-019-05023-4/FIGURES/5`. URL: `https://link.springer.com/article/10.1007/s00125-019-05023-4`.

[81]   Dan Zhang, Fan Huang, Maziyar Khansari, et al. "Automatic corneal nerve fiber segmentation and geometric biomarker quantification". In: *The European Physical Journal Plus 2020 135:2* 135 (2 Feb. 2020), pp. 1–16. ISSN: 2190-5444. DOI: `10.1140/EPJP/S13360-020-00127-Y`. URL: `https://link.springer.com/article/10.1140/epjp/s13360-020-00127-y`.

[82]   Sheng Zhang, Han Yan, Jidong Teng, and Daichao Sheng. "A mathematical model of tortuosity in soil considering particle arrangement". In: *Vadose Zone Journal* 19 (1 Jan. 2020), e20004. ISSN: 1539-1663. DOI: `10.1002/VZJ2.20004`. URL: `https://onlinelibrary.wiley.com/doi/full/10.1002/vzj2.20004https://onlinelibrary.wiley.com/doi/abs/10.1002/vzj2.`

20004https://acsess.onlinelibrary.wiley.com/doi/10.1002/vzj2.20004.

[83] Dipika V. Patel and Charles N. McGhee. "Quantitative analysis of in vivo confocal microscopy images: A review". In: *Survey of Ophthalmology* 58 (5 Sept. 2013), pp. 466–475. ISSN: 0039-6257. DOI: 10.1016/J.SURVOPHTHAL.2012.12.003. URL: http://www.surveyophthalmol.com/article/S0039625712003025/fulltexthttp://www.surveyophthalmol.com/article/S0039625712003025/abstracthttps://www.surveyophthalmol.com/article/S0039-6257(12)00302-5/abstract.

[84] Ana Ferreira, António Miguel Morgado, and José Silvestre Silva. "A method for corneal nerves automatic segmentation and morphometric analysis". In: *Computer Methods and Programs in Biomedicine* 107 (1 July 2012), pp. 53–60. ISSN: 0169-2607. DOI: 10.1016/J.CMPB.2011.09.014.

[85] Fabio Scarpa, Enrico Grisan, and Alfredo Ruggeri. "Automatic Recognition of Corneal Nerve Structures in Images from Confocal Microscopy". In: *Investigative Ophthalmology & Visual Science* 49 (11 Nov. 2008), pp. 4801–4807. ISSN: 1552-5783. DOI: 10.1167/IOVS.08-2061.

[86] M. A. Dabbah, J. Graham, I. Petropoulos, M. Tavakoli, and R. A. Malik. "Dual-model automatic detection of nerve-fibres in corneal confocal microscopy images". In: *Lecture Notes in Computer Science (including subseries Lecture Notes in Artificial Intelligence and Lecture Notes in Bioinformatics)* 6361 LNCS (PART 1 2010), pp. 300–307. ISSN: 03029743. DOI: 10.1007/978-3-642-15705-9_37/COVER/. URL: https://link.springer.com/chapter/10.1007/978-3-642-15705-9_37.

[87] M. A. Dabbah, J. Graham, I. N. Petropoulos, M. Tavakoli, and R. A. Malik. "Automatic analysis of diabetic peripheral neuropathy using multi-scale quantitative morphology of nerve fibres in corneal confocal microscopy imaging". In: *Medical Image Analysis* 15 (5 Oct. 2011), pp. 738–747. ISSN: 1361-8415. DOI: 10.1016/J.MEDIA.2011.05.016.

[88] Xin Chen, Jim Graham, Mohammad A. Dabbah, Ioannis N. Petropoulos, Mitra Tavakoli, and Rayaz A. Malik. "An automatic tool for quantification of nerve fibers in corneal confocal microscopy images". In: *IEEE Transactions on Biomedical Engineering* 64 (4 2017), pp. 786–794. ISSN: 15582531. DOI: 10.1109/TBME.2016.2573642.

[89] Enrico Grisan, Marco Foracchia, and Alfredo Ruggeri. "A novel method for the automatic grading of retinal vessel tortuosity". In: *IEEE Transactions on Medical Imaging* 27 (3 Mar. 2008). https://ieeexplore.ieee.org/stamp/stamp.jsp?tp=&arnumber=4359043, pp. 310–319. ISSN: 02780062. DOI: 10.1109/TMI.2007.904657.

[90] Ana Ferreira, António Miguel Morgado, and José Silvestre Silva. "Corneal nerves segmentation and morphometric parameters quantification for early detection of diabetic neuropathy". In: *IFMBE Proceedings* 29 (2010), pp. 264–267. ISSN: 16800737. DOI: `10.1007/978-3-642-13039-7_66/COVER/`. URL: `https://link.springer.com/chapter/10.1007/978-3-642-13039-7_66`.

[91] Iulian Otel, Pedro Cardoso, Leonor Gomes, et al. "Diabetic peripheral neuropathy assessment through corneal nerve morphometry". In: *3rd Portuguese Bioengineering Meeting, ENBENG 2013 - Book of Proceedings* (2013). DOI: `10.1109/ENBENG.2013.6518436`.

[92] Christine W. Sindt, Bruno Lay, Helene Bouchard, and Jami R. Kern. "Rapid image evaluation system for corneal in vivo confocal microscopy". In: *Cornea* 32 (4 Apr. 2013), pp. 460–465. ISSN: 02773740. DOI: `10.1097/ICO.0b013e31825ab9e2`. URL: `https://journals.lww.com/corneajrnl/Fulltext/2013/04000/Rapid_Image_Evaluation_System_for_Corneal_In_Vivo.20.aspx`.

[93] Shumoos Al-Fahdawi, Rami Qahwaji, Alaa S. Al-Waisy, Stanley Ipson, Rayaz A. Malik, Arun Brahma, and Xin Chen. "A fully automatic nerve segmentation and morphometric parameter quantification system for early diagnosis of diabetic neuropathy in corneal images". In: *Computer Methods and Programs in Biomedicine* 135 (Oct. 2016), pp. 151–166. ISSN: 0169-2607. DOI: `10.1016/J.CMPB.2016.07.032`.

[94] Pedro Guimarães, Jeff Wigdahl, Enea Poletti, and Alfredo Ruggeri. "A fully-automatic fast segmentation of the sub-basal layer nerves in corneal images". In: *2014 36th Annual International Conference of the IEEE Engineering in Medicine and Biology Society, EMBC 2014* (Nov. 2014), pp. 5422–5425. DOI: `10.1109/EMBC.2014.6944852`.

[95] Pedro Guimarães, Jeffrey Wigdahl, and Alfredo Ruggeri. "A fast and efficient technique for the automatic tracing of corneal nerves in confocal microscopy". In: *Translational Vision Science and Technology* 5 (5 2016). ISSN: 21642591. DOI: `10.1167/tvst.5.5.7`.

[96] Neil S. Lagali, Stephan Allgeier, Pedro Guimarães, et al. "Wide-field corneal subbasal nerve plexus mosaics in age-controlled healthy and type 2 diabetes populations". In: *Scientific Data 2018 5:1* 5 (1 Apr. 2018), pp. 1–12. ISSN: 2052-4463. DOI: `10.1038/sdata.2018.75`. URL: `https://www.nature.com/articles/sdata201875`.

[97] Fabio Scarpa, Xiaodong Zheng, Yuichi Ohashi, and Alfredo Ruggeri. "Automatic evaluation of corneal nerve tortuosity in images from in vivo confocal microscopy". In: *Investigative Ophthalmology and Visual Science* 52 (9 Aug. 2011), pp. 6404–6408. ISSN: 01460404. DOI: `10.1167/iovs.11-7529`.

[98] Alessia Colonna, Fabio Scarpa, and Alfredo Ruggeri. "Segmentation of Corneal Nerves Using a U-Net-Based Convolutional Neural Network". In: *Lecture Notes in Computer Science (including subseries Lecture Notes in Artificial Intelligence and Lecture Notes in Bioinformatics)* 11039 LNCS (2018), pp. 185–192. ISSN: 16113349. DOI: 10.1007/978-3-030-00949-6_22. URL: http://link.springer.com/10.1007/978-3-030-00949-6_22.

[99] Fabio Scarpa, Alessia Colonna, and Alfredo Ruggeri. "Multiple-Image Deep Learning Analysis for Neuropathy Detection in Corneal Nerve Images". In: *Cornea* 39 (3 2020), pp. 342–347. ISSN: 15364798. DOI: 10.1097/ICO.0000000000002181.

[100] Stephan Allgeier, Andrey Zhivov, Franz Eberle, et al. "Image Reconstruction of the Subbasal Nerve Plexus with In Vivo Confocal Microscopy". In: *Investigative Ophthalmology & Visual Science* 52 (9 Aug. 2011), pp. 5022–5028. ISSN: 1552-5783. DOI: 10.1167/IOVS.10-6065. URL: http://rsb.info.nih.gov/ij/index..

[101] Enea Poletti, Jeffrey Wigdahl, Pedro Guimarães, and Alfredo Ruggeri. *Automatic montaging of corneal sub-basal nerve images for the composition of a wide-range mosaic*. 2014. ISBN: 9781424479290. DOI: 10.1109/EMBC.2014.6944853.

[102] Timothy J. Holmes, Marco Pellegrini, Clayton Miller, Thomas Epplin-Zapf, Sean Larkin, Saverio Luccarelli, and Giovanni Staurenghi. "Automated Software Analysis of Corneal Micrographs for Peripheral Neuropathy". In: *Investigative Ophthalmology & Visual Science* 51 (9 Sept. 2010), p. 4480. ISSN: 01460404. DOI: 10.1167/IOVS.09-4108. URL: /pmc/articles/PMC2941165//pmc/articles/PMC2941165/?report=abstracthttps://www.ncbi.nlm.nih.gov/pmc/articles/PMC2941165/.

[103] Enea Poletti and Alfredo Ruggeri. "Automatic nerve tracking in confocal images of corneal subbasal epithelium." In: *Proceedings of CBMS 2013 - 26th IEEE International Symposium on Computer-Based Medical Systems* (2013), pp. 119–124. DOI: 10.1109/CBMS.2013.6627775.

[104] Roberto Annunziata, Ahmad Kheirkhah, Shruti Aggarwal, Pedram Hamrah, and Emanuele Trucco. "A fully automated tortuosity quantification system with application to corneal nerve fibres in confocal microscopy images". In: *Medical Image Analysis* 32 (Aug. 2016), pp. 216–232. ISSN: 13618423. DOI: 10.1016/j.media.2016.04.006.

[105] Pedro Guimarães, Jeff Wigdahl, and Alfredo Ruggeri. "Automatic estimation of corneal nerves focused tortuosities". In: *Proceedings of the Annual International Conference of the IEEE Engineering in Medicine and Biology Society, EMBS* 2016-Octob (316990 2016), pp. 1332–1335. ISSN: 1557170X. DOI: 10.1109/EMBC.2016.7590953.

[106] Tooba Salahuddin and Uvais Qidwai. "Neuro-fuzzy classifier for corneal nerve images". In: *2018 IEEE EMBS Conference on Biomedical Engineering and Sciences, IECBES 2018 - Proceedings* (Jan. 2019), pp. 131–136. DOI: `10.1109/IECBES.2018.8626633`.

[107] Tooba Salahuddin and Uvais Qidwai. "Classification of corneal nerve images using machine learning techniques". In: *International Journal of Integrated Engineering* 11 (3 2019), pp. 1–9. ISSN: 2229838X. DOI: `10.30880/IJIE.2019.11.03.001`.

[108] Cirous Dehghani, Nicola Pritchard, Katie Edwards, Anthony W. Russell, Rayaz A. Malik, and Nathan Efron. "Fully automated, semiautomated, and manual morphometric analysis of corneal subbasal nerve plexus in individuals with and without diabetes". In: *Cornea* 33 (7 2014), pp. 696–702. ISSN: 15364798. DOI: `10.1097/ICO.0000000000000152`. URL: `https://journals.lww.com/corneajrnl/Fulltext/2014/07000/Fully_Automated,_Semiautomated,_and_Manual.9.aspx`.

[109] Philip Mehrgardt, Seid Miad Zandavi, Simon K Poon, Juno Kim, Maria Markoulli, and Matloob Khushi. "U-Net Segmented Adjacent Angle Detection (USAAD) for Automatic Analysis of Corneal Nerve Structures". In: *Data* 5.2 (2020). ISSN: 2306-5729. DOI: `10.3390/data5020037`. URL: `www.mdpi.com/journal/data`.

[110] Roberto Annunziata, Ahmad Kheirkhah, Shruti Aggarwal, Bernardo M. Cavalcanti, Pedram Hamrah, and Emanuele Trucco. "Tortuosity classification of corneal nerves images using a multiple-scale-multiple-window approach". In: The University of Iowa, May 2017, pp. 113–120. DOI: `10.17077/omia.1016`.

[111] Edoardo Villani, Christophe Baudouin, Nathan Efron, et al. "In Vivo Confocal Microscopy of the Ocular Surface: From Bench to Bedside". In: *Current eye research* 39 (3 Mar. 2014), p. 213. ISSN: 02713683. DOI: `10.3109/02713683.2013.842592`. URL: `/pmc/articles/PMC3960287//pmc/articles/PMC3960287/?report=abstracthttps://www.ncbi.nlm.nih.gov/pmc/articles/PMC3960287/`.

[112] Ana Ferreira, António Miguel Morgado, and José Silvestre Silva. "Automatic corneal nerves recognition for earlier diagnosis and follow-up of diabetic neuropathy". In: *Lecture Notes in Computer Science (including subseries Lecture Notes in Artificial Intelligence and Lecture Notes in Bioinformatics)* 6112 LNCS (PART 2 2010), pp. 60–69. ISSN: 03029743. DOI: `10.1007/978-3-642-13775-4_7/COVER/`. URL: `https://link.springer.com/chapter/10.1007/978-3-642-13775-4_7`.

[113] Raidel Herrera-Pereda, Alberto Taboada Crispi, Danilo Babin, Wilfried Philips, and Márcio Holsbach Costa. "A Review On digital image processing techniques for in-Vivo confocal images of the cornea". In: *Medical Image*

Analysis 73 (Oct. 2021), p. 102188. ISSN: 1361-8415. DOI: `10.1016/J.MEDIA.2021.102188`.

[114] Erik Meijering, M. Jacob, J. C.F. Sarria, P. Steiner, H. Hirling, and M. Unser. "Design and Validation of a Tool for Neurite Tracing and Analysis in Fluorescence Microscopy Images". In: *Cytometry Part A* 58 (2 2004), pp. 167–176. ISSN: 15524922. DOI: `10.1002/CYTO.A.20022`.

[115] Amber A. van der Heijden, Michael D. Abramoff, Frank Verbraak, Manon V. van Hecke, Albert Liem, and Giel Nijpels. "Validation of automated screening for referable diabetic retinopathy with the IDx-DR device in the Hoorn Diabetes Care System". In: *Acta ophthalmologica* 96 (1 Feb. 2018), pp. 63–68. ISSN: 1755-3768. DOI: `10.1111/AOS.13613`. URL: `https://pubmed.ncbi.nlm.nih.gov/29178249/`.

[116] *FDA permits marketing of artificial intelligence-based device to detect certain diabetes-related eye problems | FDA*. URL: `https://www.fda.gov/news-events/press-announcements/fda-permits-marketing-artificial-intelligence-based-device-detect-certain-diabetes-related-eye`.

[117] Olaf Ronneberger, Philipp Fischer, and Thomas Brox. "U-net: Convolutional networks for biomedical image segmentation". In: *Lecture Notes in Computer Science (including subseries Lecture Notes in Artificial Intelligence and Lecture Notes in Bioinformatics)* 9351 (2015), pp. 234–241. ISSN: 16113349. DOI: `10.1007/978-3-319-24574-4_28`. URL: `http://lmb.informatik.uni-freiburg.de/`.

[118] Toufique A Soomro, Ahmed J Afifi, Junbin Gao, Olaf Hellwich, Manoranjan Paul, and Lihong Zheng. *Strided U-Net Model: Retinal Vessels Segmentation using Dice Loss; Strided U-Net Model: Retinal Vessels Segmentation using Dice Loss*. 2018. ISBN: 9781538666029.

[119] Ozan Oktay, Jo Schlemper, Loic Le Folgoc, et al. "Attention U-Net: Learning Where to Look for the Pancreas". In: 2018. ISBN: 1804.03999v3.

[120] Muhammad Islam, Kaleem Nawaz Khan, and Muhammad Salman Khan. *EasyChair Preprint Evaluation of Preprocessing Techniques for U-Net Based Automated Liver Segmentation Evaluation of Preprocessing Techniques for U-Net Based Automated Liver Segmentation*. 2021.

[121] Anna Fabijańska. "Segmentation of corneal endothelium images using a U-Net-based convolutional neural network". In: *Artificial Intelligence in Medicine* 88 (2018), pp. 1–13. ISSN: 18732860. DOI: `10.1016/j.artmed.2018.04.004`.

[122] Shanshan Wei, Faqiang Shi, Yuexin Wang, Yilin Chou, and Xuemin Li. "A Deep Learning Model for Automated Sub-Basal Corneal Nerve Segmentation and Evaluation Using In Vivo Confocal Microscopy". In: *Translational Vision Science & Technology* 9 (2 Jan. 2020), pp. 32–32. ISSN: 2164-2591. DOI: `10.1167/tvst.9.2.32`. URL: `https://doi.org/10.1167/tvst.9.2.32`.

[123] Xiang Li, Shuo Chen, Xiaolin Hu, and Jian Yang. "Understanding the Disharmony between Dropout and Batch Normalization by Variance Shift". In: *Proceedings of the IEEE Computer Society Conference on Computer Vision and Pattern Recognition* 2019-June (Jan. 2018), pp. 2677–2685. ISSN: 10636919. DOI: `10.48550/arxiv.1801.05134`. URL: `https://arxiv.org/abs/1801.05134v1`.

[124] Christian Garbin, · Xingquan Zhu, · Oge Marques, and Xingquan Zhu. "Dropout vs. batch normalization: an empirical study of their impact to deep learning". In: *Multimedia Tools and Applications* 79 (2020), pp. 12777–12815. DOI: `10.1007/s11042-019-08453-9`. URL: `https://doi.org/10.1007/s11042-019-08453-9`.

[125] Xiao Xiao, Sheng Lian, Zhiming Luo, and Shaozi Li. "Weighted Res-UNet for High-Quality Retina Vessel Segmentation; Weighted Res-UNet for High-Quality Retina Vessel Segmentation". In: *2018 9th International Conference on Information Technology in Medicine and Education (ITME)* (2018). DOI: `10.1109/ITME.2018.00080`. URL: `https://www.isi.uu.nl/Research/Databases/DRIVE/`.

[126] Zhengquan Chu, Tian Tian, Ruyi Feng, and Lizhe Wang. *Sea-Land Segmentation With Res-UNet And Fully Connected CRF; Sea-Land Segmentation With Res-UNet And Fully Connected CRF*. 2019. ISBN: 9781538691540.

[127] Kaiming He, Xiangyu Zhang, Shaoqing Ren, and Jian Sun. "Deep Residual Learning for Image Recognition". In: 2016, pp. 770–778. URL: `http://image-net.org/challenges/LSVRC/2015/`.

[128] Liang-Chieh Chen, George Papandreou, Florian Schroff, and Hartwig Adam. *Rethinking Atrous Convolution for Semantic Image Segmentation*. 2017.

[129] Bruno Artacho and Andreas Savakis. "Waterfall Atrous Spatial Pooling Architecture for Efficient Semantic Segmentation". In: *Sensors (Switzerland)* 19 (24 Dec. 2019). DOI: `10.3390/s19245361`. URL: `http://arxiv.org/abs/1912.03183http://dx.doi.org/10.3390/s19245361`.

[130] Saumya Jetley, Nicholas A Lord, Namhoon Lee, and Philip H S Torr. "Learn to pay attention". In: 2018.

[131] Jo Schlemper, Ozan Oktay, Michiel Schaap, Mattias Heinrich, Bernhard Kainz, Ben Glocker, and Daniel Rueckert. "Attention gated networks: Learning to leverage salient regions in medical images". In: *Medical Image Analysis* 53 (Apr. 2019), pp. 197–207. ISSN: 13618423. DOI: `10.1016/J.MEDIA.2019.01.012`. URL: `https://doi.org/10.1016/j.media.2019.01.012`.

[132] Kevin Trebing, Tomasz Staczyk, and Siamak Mehrkanoon. "SmaAt-UNet: Precipitation nowcasting using a small attention-UNet architecture". In: *Pattern Recognition Letters* 145 (May 2021), pp. 178–186. ISSN: 0167-8655. DOI: `10.1016/J.PATREC.2021.01.036`.

[133] Xiaoning Cui, Qicai Wang, Jinpeng Dai, Yanjin Xue, and Yun Duan. "Intelligent crack detection based on attention mechanism in convolution neural network". In: 24 (9 2021), pp. 1859–1868. DOI: 10.1177/1369433220986638.

[134] Shruti Jadon. "A survey of loss functions for semantic segmentation". In: 2020, pp. 1–7. ISBN: 9781728194684. DOI: 10.1109/CIBCB48159.2020.9277638. URL: https://github.com/shruti-jadon/Semantic-.

[135] Carole H. Sudre, Wenqi Li, Tom Vercauteren, Sebastien Ourselin, and M. Jorge Cardoso. "Generalised Dice Overlap as a Deep Learning Loss Function for Highly Unbalanced Segmentations". In: *Lecture Notes in Computer Science (including subseries Lecture Notes in Artificial Intelligence and Lecture Notes in Bioinformatics)* 10553 LNCS (2017), pp. 240–248. ISSN: 16113349. DOI: 10.1007/978-3-319-67558-9_28. URL: https://link.springer.com/chapter/10.1007/978-3-319-67558-9_28.

[136] Lee R. Dice. "Measures of the Amount of Ecologic Association Between Species". In: *Ecology* 26 (3 July 1945), pp. 297–302. ISSN: 1939-9170. DOI: 10.2307/1932409. URL: https://onlinelibrary.wiley.com/doi/full/10.2307/1932409https://onlinelibrary.wiley.com/doi/abs/10.2307/1932409https://esajournals.onlinelibrary.wiley.com/doi/10.2307/1932409.

[137] Seyed Sadegh, Mohseni Salehi, Deniz Erdogmus, Ali Gholipour, Seyed Sadegh Mohseni Salehi, Deniz Erdogmus, and Ali Gholipour. "Tversky Loss Function for Image Segmentation Using 3D Fully Convolutional Deep Networks". In: *Machine Learning in Medical Imaging. MLMI 2017. Lecture Notes in Computer Science* 10541 LNCS (2017), pp. 379–387. ISSN: 16113349. DOI: 10.1007/978-3-319-67389-9_44. URL: https://link.springer.com/chapter/10.1007/978-3-319-67389-9_44.

[138] Amos Tversky. "Features of similarity". In: *Psychological Review* 84 (4 July 1977), pp. 327–352. ISSN: 0033295X. DOI: 10.1037/0033-295X.84.4.327.

[139] Nabila Abraham and Naimul Mefraz Khan. "A Novel Focal Tversky loss function with improved Attention U-Net for lesion segmentation". In: 2019, pp. 683–687. DOI: 10.1109/ISBI.2019.8759329. URL: https://github.com/nabsabraham/focal-tversky-unet.

[140] Grégoire Malandain and Sara Fernández-Vidal. "Euclidean skeletons". In: *Image and Vision Computing* 16 (5 Apr. 1998), pp. 317–327. ISSN: 0262-8856. DOI: 10.1016/S0262-8856(97)00074-7.

[141] Louisa Lam and Seong Whan Lee. "Thinning methodologies—a comprehensive survey". In: *IEEE Transactions on Pattern Analysis and Machine Intelligence* 14 (9 1992), pp. 869–885. ISSN: 01628828. DOI: 10.1109/34.161346.

[142] Punam K. Saha, Gunilla Borgefors, and Gabriella Sanniti di Baja. "A survey on skeletonization algorithms and their applications". In: *Pattern Recognition Letters* 76 (June 2016), pp. 3–12. ISSN: 0167-8655. DOI: 10.1016/J.PATREC.2015.04.006.

[143] Francois Chollet et al. "Keras". In: (2015). URL: https://github.com/fchollet/keras.

[144] Martín Abadi, Ashish Agarwal, Paul Barham, et al. "TensorFlow: Large-Scale Machine Learning on Heterogeneous Systems". In: (2015). Software available from tensorflow.org. URL: http://tensorflow.org/.

[145] Diederik P. Kingma and Jimmy Lei Ba. "Adam: A Method for Stochastic Optimization". In: *3rd International Conference on Learning Representations, ICLR 2015 - Conference Track Proceedings* (Dec. 2014). DOI: 10.48550/arxiv.1412.6980. URL: https://arxiv.org/abs/1412.6980v9.

[146] Alessia Colonna, Fabio Scarpa, and Alfredo Ruggeri. "Automatic estimation of nerve tortuosity in corneal images". In: *VII Congress of the National Group of Bioengineering (GNB2020)* (2020), pp. 10–13.

[147] Luisa Simo Mannion, Cindy Tromans, and Clare O'Donnell. "Corneal nerve structure and function in keratoconus: A case report". In: *Eye and Contact Lens* 33 (2 Mar. 2007), pp. 106–108. ISSN: 15422321. DOI: 10.1097/01.ICL.0000235270.45379.9C. URL: https://journals.lww.com/claojournal/Fulltext/2007/03000/Corneal_Nerve_Structure_and_Function_in.11.aspx.

[148] Baikai Ma, Jianyang Xie, Tingting Yang, et al. "Quantification of Increased Corneal Subbasal Nerve Tortuosity in Dry Eye Disease and Its Correlation With Clinical Parameters". In: *Translational Vision Science & Technology* 10 (6 May 2021), pp. 26–26. ISSN: 2164-2591. DOI: 10.1167/TVST.10.6.26. URL: https://doi.org/10.1167/tvst.10.6.26.

[149] Stefano De Cillà, Stefano Ranno, Elisa Carini, Paolo Fogagnolo, Gaia Ceresara, Nicola Orzalesi, and Luca M. Rossetti. "Corneal Subbasal Nerves Changes in Patients with Diabetic Retinopathy: An In Vivo Confocal Study". In: *Investigative Ophthalmology & Visual Science* 50 (11 Nov. 2009), pp. 5155–5158. ISSN: 1552-5783.

[150] Giuseppe Giannaccare, Marina Buzzi, Michela Fresina, Claudio Velati, and Piera Versura. "Efficacy of 2-Month Treatment with Cord Blood Serum Eye Drops in Ocular Surface Disease: An in Vivo Confocal Microscopy Study". In: *Cornea* 36 (8 Aug. 2017), pp. 915–921. ISSN: 15364798. DOI: 10.1097/ICO.0000000000001257. URL: https://journals.lww.com/corneajrnl/Fulltext/2017/08000/Efficacy_of_2_Month_Treatment_With_Cord_Blood.4.aspx.

[151] William E. Hart, Michael Goldbaum, Brad Côté, Paul Kube, and Mark R. Nelson. "Measurement and classification of retinal vascular tortuosity". In: *International Journal of Medical Informatics* 53 (2-3 Feb. 1999), pp. 239–252. ISSN: 13865056. DOI: 10.1016/S1386-5056(98)00163-4.

[152] W. D. Kearns, V. O. Nams, and J. L. Fozard. "Tortuosity in movement paths is related to cognitive impairment wireless fractal Estimation in assisted living facility residents". In: *Methods of Information in Medicine* 49 (6 2010), pp. 592–598. ISSN: 00261270. DOI: 10.3414/ME09-01-0079/ID/JR0079-19. URL: http://www.thieme-connect.de/products/ejournals/html/10.3414/ME09-01-0079http://www.thieme-connect.de/DOI/DOI?10.3414/ME09-01-0079.

[153] William D. Kearns, James L. Fozard, Lawrence Schonfeld, Steven Scott, and Katharine Marshall. "Elevated movement path tortuosity in voluntary outdoor ambulation in community-dwelling veterans with a history of traumatic brain injury". In: *Journal of Head Trauma Rehabilitation* 30 (1 Jan. 2015), E8–E14. ISSN: 1550509X. DOI: 10.1097/HTR.0000000000000021. URL: https://journals.lww.com/headtraumarehab/Fulltext/2015/01000/Elevated_Movement_Path_Tortuosity_in_Voluntary.9.aspx.

[154] David P. Fyhrie and Roger Zauel. "Directional Tortuosity as a Predictor of Modulus Damage for Vertebral Cancellous Bone". In: *Journal of Biomechanical Engineering* 137 (1 Jan. 2015). ISSN: 15288951. DOI: 10.1115/1.4029177/370933. URL: https://asmedigitalcollection.asme.org/biomechanical/article/137/1/011007/370933/Directional-Tortuosity-as-a-Predictor-of-Modulus.

[155] Adam Li and Shahram Payandeh. "An overview of path tortuosity measures for tracking and monitoring". In: *7th IEEE Annual Information Technology, Electronics and Mobile Communication Conference, IEEE IEMCON 2016* (Nov. 2016). DOI: 10.1109/IEMCON.2016.7746271.

[156] Örjan Smedby, Nils Högman, Sven Nilsson, Uno Erikson, Anders G. Olsson, and Goran Walldius. "Two-Dimensional Tortuosity of the Superficial Femoral Artery in Early Atherosclerosis". In: *Journal of Vascular Research* 30 (4 1993), pp. 181–191. ISSN: 1018-1172. DOI: 10.1159/000158993. URL: https://www.karger.com/Article/FullText/158993https://www.karger.com/Article/Abstract/158993.

[157] Emanuele Trucco, Hind Azegrouz, and Baljean Dhillon. "Modeling the Tortuosity of Retinal Vessels:Does Caliber Play a Role?" In: *IEEE TRANSACTIONS ON BIOMEDICAL ENGINEERING* 57 (9 Sept. 2010), pp. 2239–2247. ISSN: 00189294. DOI: 10.1109/TBME.2010.2050771. URL: http://ieeexplore.ieee.org.

[158] K. V. Chandrinos, M. Pilu, R. B. Fisher, and P.E. Trahanias. "Image Processing Techniques for the Quantification of Atherosclerotic Changes". In: (1998). URL: http://130.203.136.95/viewdoc/summary?doi=10.1.1.48.5956.

[159] Elizabeth Bullitt, Guido Gerig, Stephen M Pizer, et al. "Measuring Tortuosity of the Intracerebral Vasculature from MRA Images". In: *IEEE Trans Med Imaging* 22(9) (2003), pp. 1163–1171. DOI: 10.1109/TMI.2003.816964.

[160] Goh Kheng Guan, Wynne Hsu, M. Li Lee, and Huan Wang. "ADRIS: an Automatic Diabetic Retinal Image Screening system". In: *Studies in Fuzziness and Soft Computing* 60 (2001), pp. 181–210.

[161] Ernesto Bribiesca. "A measure of tortuosity based on chain coding". In: *Pattern Recognition* 46 (3 Mar. 2013), pp. 716–724. ISSN: 0031-3203. DOI: 10.1016/J.PATCOG.2012.09.017.

[162] Mowda Abdalla, Andrew Hunter, and Bashir Al-Diri. "Quantifying retinal blood vessels' tortuosity - Review". In: *Proceedings of the 2015 Science and Information Conference, SAI 2015* (Sept. 2015), pp. 687–693. DOI: 10.1109/SAI.2015.7237216.

[163] Chanjira Sinthanayothin, Pattheera Panitsuk, and Bunyarit Uyyanonvara. "Automatic retinal vessel tortuosity measurement". In: 2010, pp. 505–507.

[164] Geoffrey Dougherty and Jozsef Varro. "A quantitative index for the measurement of the tortuosity of blood vessels". In: *Medical Engineering & Physics* 22 (8 Oct. 2000), pp. 567–574. ISSN: 1350-4533. DOI: 10.1016/S1350-4533(00)00074-6.

[165] Susannah Q. Longmuir, Katherine D. Mathews, Reid A. Longmuir, Vinayak Joshi, Richard J. Olson, and Michael D. Abrmoff. "Retinal arterial but not venous tortuosity correlates with facioscapulohumeral muscular dystrophy severity". In: *Journal of AAPOS : the official publication of the American Association for Pediatric Ophthalmology and Strabismus* 14 (3 June 2010), pp. 240–243. ISSN: 1528-3933. DOI: 10.1016/J.JAAPOS.2010.03.006. URL: https://pubmed.ncbi.nlm.nih.gov/20603058/.

[166] Hind Azegrouz, Emanuele Trucco, Baljean Dhillon, Thomas MacGillivray, and I. J. MacCormick. "Thickness dependent tortuosity estimation for retinal blood vessels". In: *Annual International Conference of the IEEE Engineering in Medicine and Biology - Proceedings* (2006), pp. 4675–4678. ISSN: 05891019. DOI: 10.1109/IEMBS.2006.260558.

[167] Z. Martin Rodriguez, P. Kenny, and L. Gaynor. "Improved characterisation of aortic tortuosity". In: *Medical Engineering & Physics* 33 (6 July 2011), pp. 712–719. ISSN: 1350-4533. DOI: 10.1016/J.MEDENGPHY.2011.01.008.

[168] Neil Lagali, Enea Poletti, Dipika V. Patel, et al. "Focused tortuosity definitions based on expert clinical assessment of corneal subbasal nerves". In: *Investigative Ophthalmology and Visual Science* 56 (9 2015), pp. 5102–5109. ISSN: 15525783. DOI: 10.1167/iovs.15-17284. URL: https://pubmed.ncbi.nlm.nih.gov/26241397/.

[169] Yitian Zhao, Jiong Zhang, Ella Pereira, et al. "Automated Tortuosity Analysis of Nerve Fibers in Corneal Confocal Microscopy". In: *IEEE Transactions on Medical Imaging* 39 (9 2020), pp. 2725–2737. ISSN: 1558254X. DOI: 10.1109/TMI.2020.2974499.

[170] Xin Chen, Jim Graham, Ioannis N. Petropoulos, et al. "Corneal Nerve Fractal Dimension: A Novel Corneal Nerve Metric for the Diagnosis of Diabetic Sensorimotor Polyneuropathy". In: *Investigative Ophthalmology & Visual Science* 59 (2 Feb. 2018), pp. 1113–1118. ISSN: 1552-5783. URL: https://doi.org/10.1167/.

[171] Alessia Colonna, Fabio Scarpa, Alfredo Ruggeri, and Fabio; Ruggeri Alfredo Colonna Alessia; Scarpa. "Automatic tracing of corneal sub-basal nerves using deep learning". In: 2019, Vol.60, 4237. URL: https://iovs.arvojournals.org/article.aspx?articleid=2745820.

[172] Alessia Colonna, Fabio Scarpa, Riccardo Zorzan, et al. "Automatic identification of corneal epithelial dendritic cells via deep learning". In: *Investigative Ophthalmology & Visual Science* 61 (7 June 2020), pp. 4309–4309. ISSN: 1552-5783.

[173] R. A. Malik, P. Kallinikos, C. A. Abbott, C. H.M. Van Schie, P. Morgan, N. Efron, and A. J.M. Boulton. "Corneal confocal microscopy: a non-invasive surrogate of nerve fibre damage and repair in diabetic patients". In: *Diabetologia* 46 (5 May 2003), pp. 683–688. ISSN: 0012-186X. DOI: 10.1007/S00125-003-1086-8. URL: https://pubmed.ncbi.nlm.nih.gov/12739016/.

[174] Nicola Pritchard, Katie Edwards, Ayda M. Shahidi, Geoff P. Sampson, Anthony W. Russell, Rayaz A. Malik, and Nathan Efron. "Corneal markers of diabetic neuropathy". In: *The ocular surface* 9 (1 2011), pp. 17–28. ISSN: 1542-0124. DOI: 10.1016/S1542-0124(11)70006-4. URL: https://pubmed.ncbi.nlm.nih.gov/21338566/.

[175] Mitra Tavakoli, Ioannis N. Petropoulos, and Rayaz A. Malik. "Assessing corneal nerve structure and function in diabetic neuropathy". In: *Clinical & experimental optometry* 95 (3 May 2012), pp. 338–347. ISSN: 1444-0938. DOI: 10.1111/J.1444-0938.2012.00743.X. URL: https://pubmed.ncbi.nlm.nih.gov/22594548/.

[176] Mitra Tavakoli, Cristian Quattrini, Caroline Abbott, et al. "Corneal confocal microscopy: a novel noninvasive test to diagnose and stratify the severity of human diabetic neuropathy". In: *Diabetes care* 33 (8 Aug. 2010), pp. 1792–1797. ISSN: 1935-5548. DOI: 10.2337/DC10-0253. URL: https://pubmed.ncbi.nlm.nih.gov/20435796/.

[177] Pei Yao Chang, Hyman Carrel, Jen Shang Huang, et al. "Decreased density of corneal basal epithelium and subbasal corneal nerve bundle changes in patients with diabetic retinopathy". In: *American journal of ophthalmology* 142 (3

2006). ISSN: 0002-9394. DOI: 10.1016/J.AJO.2006.04.033. URL: https://pubmed.ncbi.nlm.nih.gov/16935596/.

[178] Bernard E. McCarey and Fredrick H. Schmidt. "Modeling glucose distribution in the cornea". In: *Current eye research* 9 (11 1990), pp. 1025–1039. ISSN: 0271-3683. DOI: 10.3109/02713689008997577. URL: https://pubmed.ncbi.nlm.nih.gov/2095317/.

[179] Charlotte Coopmans, Tan Lai Zhou, Ronald M.A. Henry, et al. "Both Prediabetes and Type 2 Diabetes Are Associated With Lower Heart Rate Variability: The Maastricht Study". In: *Diabetes Care* 43 (5 May 2020), pp. 1126–1133. ISSN: 0149-5992. DOI: 10.2337/DC19-2367. URL: https://diabetesjournals.org/care/article/43/5/1126/35711/Both-Prediabetes-and-Type-2-Diabetes-Are.

[180] Jeroen H.P.M. van der Velde, Annemarie Koster, Elsa S. Strotmeyer, et al. "Cardiometabolic risk factors as determinants of peripheral nerve function: the Maastricht Study". In: *Diabetologia* 63 (8 Aug. 2020), pp. 1648–1658. ISSN: 1432-0428. DOI: 10.1007/S00125-020-05194-5. URL: https://pubmed.ncbi.nlm.nih.gov/32537727/.

[181] Laura W. Vergoossen, Miranda T. Schram, Joost J. De Jong, et al. "White Matter Connectivity Abnormalities in Prediabetes and Type 2 Diabetes: The Maastricht Study". In: *Diabetes Care* 43 (1 Jan. 2020), pp. 201–208. ISSN: 0149-5992. DOI: 10.2337/DC19-0762. URL: https://diabetesjournals.org/care/article/43/1/201/35816/White-Matter-Connectivity-Abnormalities-in.

[182] Marnix J.M. Van Agtmaal, Alfons J.H.M. Houben, Vera De Wit, et al. "Prediabetes Is Associated With Structural Brain Abnormalities: The Maastricht Study". In: *Diabetes care* 41 (12 Dec. 2018), pp. 2535–2543. ISSN: 1935-5548. DOI: 10.2337/DC18-1132. URL: https://pubmed.ncbi.nlm.nih.gov/30327356/.

[183] Heide FCvd, Foreman Y, Franken I, et al. "(Pre)Diabetes, Greater Glycemia, and Greater Daily Glucose Variability are Associated with Lower Retinal Nerve Fiber Layer Thickness, an Index of Neurodegeneration and Precursor of Diabetic Retinopathy– The Maastricht Study". In: (Oct. 2021). DOI: 10.21203/RS.3.RS-970767/V1. URL: https://europepmc.org/article/ppr/ppr423414.

[184] Neil S. Lagali, Stephan Allgeier, Pedro Guimarães, et al. "Reduced Corneal Nerve Fiber Density in Type 2 Diabetes by Wide-Area Mosaic Analysis". In: *Investigative ophthalmology & visual science* 58 (14 Dec. 2017), pp. 6318–6327. ISSN: 1552-5783. DOI: 10.1167/IOVS.17-22257. URL: https://pubmed.ncbi.nlm.nih.gov/29242906/.

[185] Hassan Mansoor, Hong Chang Tan, Molly Tzu Yu Lin, Jodhbir S. Mehta, and Yu Chi Liu. "Diabetic Corneal Neuropathy". In: *Journal of clinical medicine* 9 (12 Dec. 2020), pp. 1–24. ISSN: 2077-0383. DOI: 10.3390/JCM9123956. URL: https://pubmed.ncbi.nlm.nih.gov/33291308/.

[186] Cecilia Chao, Rachel Wang, Morgan Jones, et al. "The Relationship Between Corneal Nerve Density and Hemoglobin A1c in Patients With Prediabetes and Type 2 Diabetes". In: *Investigative ophthalmology & visual science* 61 (12 Oct. 2020). ISSN: 1552-5783. DOI: 10.1167/IOVS.61.12.26. URL: https://pubmed.ncbi.nlm.nih.gov/33112943/.

[187] K. Co Shih, Ks L. Lam, and L. Tong. "A systematic review on the impact of diabetes mellitus on the ocular surface". In: *Nutrition & diabetes* 7 (3 2017). ISSN: 2044-4052. DOI: 10.1038/NUTD.2017.4. URL: https://pubmed.ncbi.nlm.nih.gov/28319106/.

[188] Eline E.B. De Clerck, Jan S.A.G. Schouten, Tos T.J.M. Berendschot, et al. "Reduced corneal nerve fibre length in prediabetes and type 2 diabetes: The Maastricht Study". In: *Acta ophthalmologica* 98 (5 Aug. 2020), pp. 485–491. ISSN: 1755-3768. DOI: 10.1111/AOS.14359. URL: https://pubmed.ncbi.nlm.nih.gov/32017403/.

[189] Miranda T. Schram, Simone J.S. Sep, Carla J. Van Der Kallen, et al. "The Maastricht Study: An extensive phenotyping study on determinants of type 2 diabetes, its complications and its comorbidities". In: *European Journal of Epidemiology* 29 (6 Apr. 2014), pp. 439–451. ISSN: 15737284. DOI: 10.1007/S10654-014-9889-0/TABLES/3. URL: https://link.springer.com/article/10.1007/s10654-014-9889-0.

[190] Lewis Kass-Iliyya, Saad Javed, David Gosal, et al. "Small fiber neuropathy in Parkinson's disease: A clinical, pathological and corneal confocal microscopy study". In: *Parkinsonism & Related Disorders* 21 (12 Dec. 2015), p. 1454. ISSN: 18735126. DOI: 10.1016/J.PARKRELDIS.2015.10.019. URL: /pmc/articles/PMC4671992//pmc/articles/PMC4671992/?report=abstracthttps://www.ncbi.nlm.nih.gov/pmc/articles/PMC4671992/.

[191] Peter J. Podgorny, Oksana Suchowersky, Kenneth G. Romanchuk, and Thomas E. Feasby. "Evidence for small fiber neuropathy in early Parkinson's disease". In: *Parkinsonism & related disorders* 28 (July 2016), pp. 94–99. ISSN: 1873-5126. DOI: 10.1016/J.PARKRELDIS.2016.04.033. URL: https://pubmed.ncbi.nlm.nih.gov/27160569/.

[192] V. L. Feigin, R. V. Krishnamurthi, A. M. Theadom, et al. "Global, regional, and national burden of neurological disorders during 1990–2015: a systematic analysis for the Global Burden of Disease Study 2015". In: *The Lancet Neurology* 16 (11 Nov. 2017), pp. 877–897. ISSN: 14744465. DOI: 10.1016/S1474-4422(17)30299-5.

[193] Thiago A. Patente, Mariana P. Pinho, Aline A. Oliveira, Gabriela C.M. Evangelista, Patrícia C. Bergami-Santos, and José A.M. Barbuto. "Human Dendritic Cells: Their Heterogeneity and Clinical Application Potential in Cancer Immunotherapy". In: *Frontiers in immunology* 9 (JAN 2019). ISSN: 1664-3224. DOI:

10.3389/FIMMU.2018.03176. URL: https://pubmed.ncbi.nlm.nih.gov/30719026/.